Modeling Creep-Fatigue-Environment Interactions in Steam Turbine Rotor Materials for Advanced Ultra-supercritical Coal Power Plants

Final Report

DOE/NETL Cooperative Agreement
DE-FE0005859

Chen Shen
Principal Investigator
518-387-4247 (Telephone)
518-387-6232 (Fax)
E-mail: chens@ge.com

Submitted to
United States Department of Energy
National Energy Technology Laboratory
Pittsburgh, PA 15236

April 2014

GE Global Research
Niskayuna, NY 12309-1027

ACKNOWLEDGMENT

This Technical Report is based upon work supported by the Department of Energy National Energy Technology Laboratory under Award No. DE-FE0005859.

DISCLAIMER

ABSTRACT

The goal of this project is to model creep-fatigue-environment interactions in steam turbine rotor materials for advanced ultra-supercritical (A-USC) coal power Alloy 282 plants, to develop and demonstrate computational algorithms for alloy property predictions, and to determine and model key mechanisms that contribute to the damages caused by creep-fatigue-environment interactions.

The nickel based Alloy 282 is selected for this project because it is one of the leading candidate materials for the high temperature/pressure section of an A-USC steam turbine. The methods developed in the project are expected to be applicable to other metal alloys in similar steam/oxidation environments. The major developments are:

- failure mechanism and microstructural characterization
- atomistic and first principles modeling of crack tip oxygen embrittlement
- modeling of gamma prime microstructures and mesoscale microstructure-defect interactions
- microstructure and damage-based creep prediction
- multi-scale crack growth modeling considering oxidation, viscoplasticity and fatigue

The technology developed in this project is expected to enable more accurate prediction of long service life of advanced alloys for A-USC power plants, and provide faster and more effective materials design, development, and implementation than current state-of-the-art computational and experimental methods.

This document is a final technical report for the project, covering efforts conducted from January 2011 to January 2014.

TABLE OF CONTENTS

ABSTRACT 3

EXECUTIVE SUMMARY 6

RESULTS AND DISCUSSIONS 8

- Task 2: Failure mechanism and microstructural characterization 8
  - 2.1. Experimental results 8
- Task 3: Atomistic and first principles modeling of crack tip oxygen embrittlement 19
  - 3.1. Stress accelerated grain boundary oxidation (SAGBO) versus dynamic embrittlement (DE) 19
  - 3.2. Models and computational methods: 23
  - 3.3. Thermodynamic stabilities 25
  - 3.4. Mechanical embrittlement on the strength of metal grain boundaries 26
  - 3.5. Diffusion kinetics of oxygen in Ni 30
    - 3.5.1. Oxygen diffusivity in crystalline Ni 30
    - 3.5.2. Oxygen and Nickel diffusivity in amorphous Ni 32
  - 3.6. Hydrolytic weakening of Chromia 35
  - 3.7. Summary 37
- Task 4: Modeling of gamma prime microstructures and mesoscale microstructure-defect interactions 38
  - 4.1. Gamma prime microstructure modeling for Alloy 282 38
    - 4.1.1. Gamma prime microstructure models 39
    - 4.1.2. Calibration of precipitation model 40
    - 4.1.3. Model validation 41
    - 4.1.4. Predictions of long-term microstructure change 46
  - 4.2. Link microstructure to creep model 47
    - 4.2.1. Average inter-particle spacing in realistic γ' microstructures 48
    - 4.2.2. Effective inter-particle spacing in realistic γ' microstructures 51
  - 4.3. Thermodynamic calculation of oxides in Alloy 282 54
  - 4.4. Mesoscale modeling of crack-microstructure-oxidation interactions 56
    - 4.4.1. Basic crack model 56
    - 4.4.2. Basic model verifications 58
    - 4.4.3. Incorporate grain microstructure 64
    - 4.4.3. Incorporate plasticity 66

    4.4.4. Incorporate oxygen diffusion and oxidation 68
    4.4.5. Modeling crack-microstructure-oxidation interactions 72
  4.5. Summary 77
Task 5: Microstructure and damage-based creep prediction...........................79
  5.1. Historical creep study on Alloy 282 79
  5.2. Observations of creep deformation mechanisms in Alloy 282 80
  5.3. Creep model formulation..82
    5.3.1. Dislocation component 82
    5.3.2. Diffusion component...84
    5.3.3. Damage variable evolution and effective stress 86
  5.4. Model predictions and sensitivity to microstructure..............................88
    5.4.1. Alloy 282 creep predictions and evaluation 88
    5.4.2. Dependence of creep on precipitate microstructure 98
  5.5. Summary 99
Task 6: Multi scale crack growth modeling considering oxidation, visco-plasticity and fatigue 100
  6.1. Overall approach 100
  6.2. Development of constitutive material models.....................................101
    6.2.1. Rate independent constitutive modeling.......................................102
    6.2.2. Rate dependent constitutive modeling 104
  6.3. CCTP model calibration...110
    6.3.1. Crack tip blunting 110
    6.3.2. Evolution equations...111
    6.3.3. Overload and crack closure effects 113
    6.3.4. Model calibration 115
    6.3.5. Results and discussion...116
  6.4. Incorporate oxidation effects..120
  6.5. 3D Crack propagation simulation: FE model setup.............................123
  6.6. Crack growth rate predictions using cyclic plasticity, creep and oxidation 128
  6.7. Summary 130
Acknowledgements..132
REFERENCES 133

EXECUTIVE SUMMARY

The crack growth response of Alloy 282 has been experimentally investigated at 1200˚F, 1400˚F, and 1600˚F as a function of cyclic period, environment, and applied stress intensity factor range level. At 1600°F, creep-fatigue and environmental-fatigue interactions are operative. At 1400°F and below however, an environmental-fatigue interaction is dominant at extended cyclic periods. Detailed microstructure characterization indicates a correlation between fatigue behaviors and *crack-tip* oxidation characteristics in Alloy 282. In particular, formation of NiO and Ni-Cr spinel oxides appears to lead to the observed porous and thus more compliant crack-tip oxide structure in the specimen tested in 1400˚F air, as opposed to the compact Cr_2O_3 and Al_2O_3 oxides in the 1400˚F steam specimen that exhibits higher crack growth rate. Thermodynamic modeling of oxides in Alloy 282 is applied to explain the suppression of NiO and spinel phases at lower pO_2 in steam as well as at the higher 1600˚F temperature.

Mechanisms of oxygen-grain boundary interactions have been studied. Oxygen embrittlement effect due to formation of oxygen monolayers in metal grain boundaries is proposed. With first principles and atomistic modeling, energetic studies confirm oxygen absorption at grain boundaries, and quantify the reduction in grain boundary cohesion strength as a function of oxygen concentration. Diffusivities of oxygen and metal element are simulated for both crystalline and amorphous (grain boundary) Ni phases. The ab initio calculation results are used in phase field crack modeling, in which grain structure, oxygen diffusion, and oxidation are explicitly treated. It is found that crack growth rate and pathway (trans-granular vs. inter-granular) can be sensitively dependent on oxygen diffusion and grain boundary strength reduction due to oxygen concentration.

Creep behaviors of Alloy 282 have been modeled with a continuum-damage based model over a series of A-USC relevant conditions of 1375-1450˚F and 15-45Ksi. The model accounts for the predominant deformation mode of dislocation climb-bypassing gamma prime precipitates observed in Alloy 282. Diffusion creep and particle shearing mechanisms are also introduced for the low-stress and high-stress regimes, respectively. Damage evolution is introduced to improve modeling of tertiary creep regime and rupture predictions. Gamma prime precipitate microstructure and its coarsening evolution are incorporated for reliable long-term creep predictions. The gamma prime microstructures are simulated by precipitation model and phase field model, which have been validated against lab heat treatment data between 1300-1650˚F up to 8000 hours aging condition.

Confined crack-tip plasticity based fatigue crack growth model has been developed for Alloy 282. Crack-tip plasticity is evaluated by 2D finite element (FE) modeling. The models are calibrated to test data at 1200˚F and 1400˚F. Crack growth behaviors under different R load ratios are predicted and validated

against test data. A 3D extension of the FE model has been demonstrated on compact-tension specimen geometry. To address the accelerated fatigue crack growth phenomena under various hold-time loading conditions, creep and oxidation are integrated in the constitutive crack growth model. Crack growth predictions are then made for three (3) loading profiles with different hold times.

RESULTS AND DISCUSSIONS

A detailed review of this project is organized in the following order:

Task 2	Failure mechanism and microstructural characterization
Task 3	Atomistic and first principles modeling of crack tip oxygen embrittlement
Task 4	Modeling of gamma-prime microstructures and mesoscale microstructure-defect interactions
Task 5	Microstructure and damage-based creep prediction
Task 6	Multi scale crack growth modeling considering oxidation, viscoplasticity and fatigue

Task 2: Failure mechanism and microstructural characterization

The objective of this task is to develop a fundamental understanding of the fatigue failure mechanisms in Alloy 282 under service conditions relevant to A-USC rotor materials. The crack growth response of Alloy 282 as a function of test temperature, cyclic period, environment, and applied stress intensity factor range (ΔK) level has been investigated. At 1600°F, creep-fatigue and environmental-fatigue interactions are operative. At 1400°F and below however, an environmental-fatigue interaction is dominant at extended cyclic periods. The experimental results below summarize the findings related to the key failure mechanisms for Alloy 282.

2.1. Experimental results

A series of compact tension specimens were fabricated from Alloy 282. Effects of temperature and environment on hold-time fatigue crack growth behavior were evaluated. Figure 1 illustrates the crack growth response of Alloy 282 at 1200°F, 1400°F, and 1600°F versus environment and total cyclic period, at a fixed stress intensity factor range.

The observed temperature effect on crack growth behavior in Alloy 282 is most pronounced between 1400°F and 1600°F, indicating a potential mechanism shift at the highest test temperature. Figure 1a and Figure 1b demonstrate the substantial increase in growth rates with increasingly aggressive environments. Under extended dwell conditions at 1200°F and 1400°F, the crack growth rates measured in steam are up to two orders of magnitude higher than those measured in vacuum. In addition, there is a relative insensitivity of growth rates to increasing cyclic periods under vacuum in Figure 1a and Figure 1b. As a result, the crack growth acceleration observed at longer cyclic periods in air and steam at 1200°F and 1400°F can be reasonably attributed to an environmental-fatigue interaction. In other words, removing the environment at these two temperatures restores the material behavior to a near-fully cycle-dependent fatigue response.

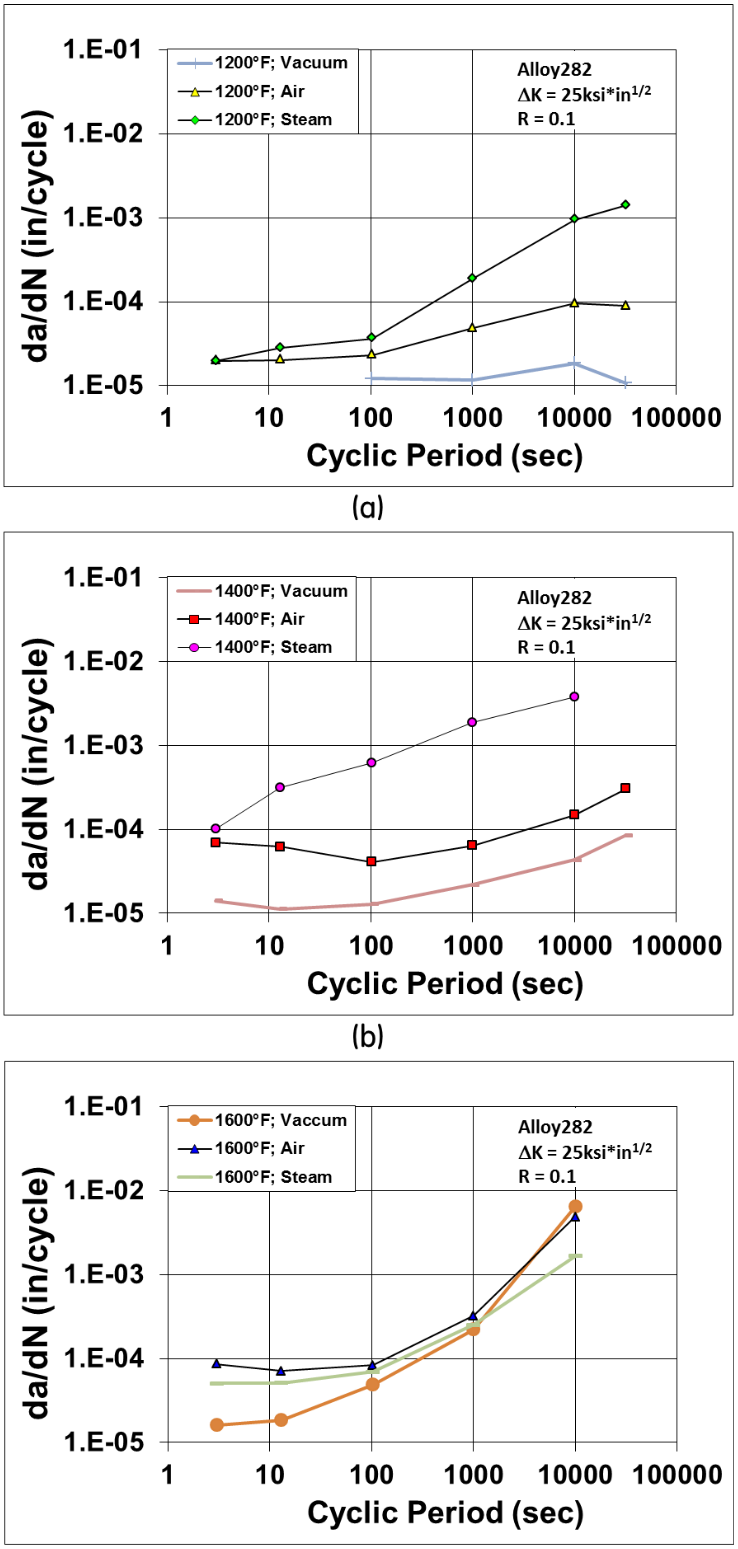

(a)

(b)

(c)

Figure 1: Alloy 282 hold-time sweep test results as a function of cyclic period, temperature, and environment (a) 1200°F (b) 1400°F, and (c) 1600°F.

At 1600°F, however, the crack growth rates in air, steam, and vacuum tend to converge (Figure 1c). While the growth rates initially indicate a slight improvement in crack growth resistance under vacuum at the shortest two incremental cyclic periods, the data for air, steam, and vacuum converge with increasing dwell-time at peak stress. Considering the growth rate is relatively unaffected by the removal of environment in this case, such convergence is indicative of a creep-fatigue interaction. Under vacuum conditions, an environmental-fatigue interaction can still play a role if the vacuum level is insufficient during testing. There was, however, no evidence of fracture surface oxidation on the specimen tested in vacuum.

Figure 2 recasts the same data at fixed environment, as a function of test temperature. Figure 2a shows the clear transition to a creep-fatigue interaction at 1600°F. Figure 2b indicates a progressively higher crack growth rate in air, with increasing test temperature and cyclic period. In steam, however, Figure 2c indicates an initially large increase in crack growth rate as the temperature is increased from 1200°F to 1400°F, followed by a significant reduction in crack growth rate as the temperature is further increased from 1400°F to 1600°F. The basis for the reduction in crack growth rate in 1600°F steam is related to the reduction in strength at that temperature. In general, the ultimate tensile strength correlates well with hold time crack growth behavior, as in Figure 3, where strength reduction typically leads to reduced hold time crack growth rates. This is commonly associated with the degree of crack-tip blunting, and associated redistribution of stress at the crack tip in plastically weaker materials. Figure 4 indicates the effect of temperature on ultimate tensile strength in Alloy 282. Between 1200°F and 1400°F, there is a ~26ksi drop in tensile strength. Between 1400°F and 1600°F there is an additional 40ksi reduction. Considering, however, that the reduction in crack growth rate between 1400°F and 1600°F occurred only in steam, the environmental-fatigue interaction in air vs. steam was explored in greater detail.

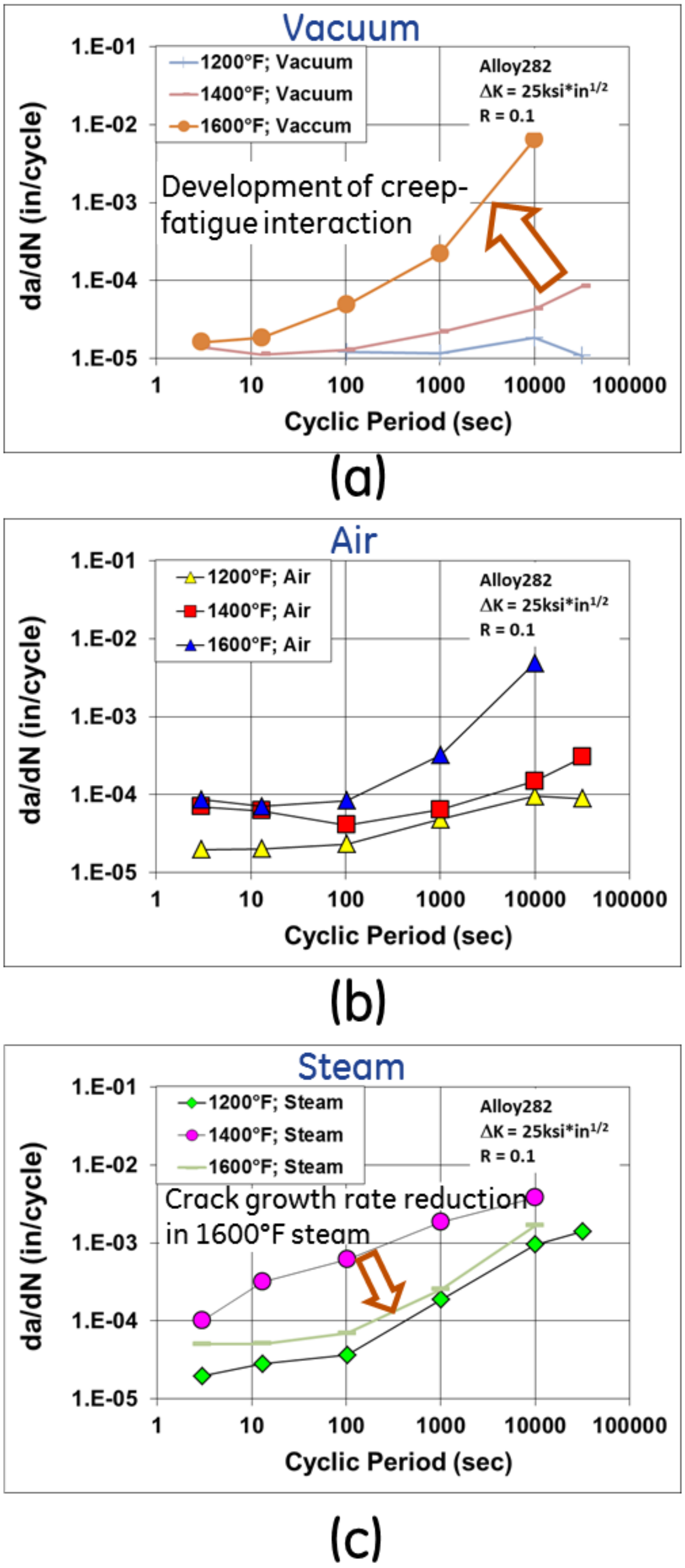

(a)

(b)

(c)

Figure 2: Alloy 282 hold-time sweep test results as a function of cyclic period, temperature, and environment (a) vacuum (b) air, and (c) steam.

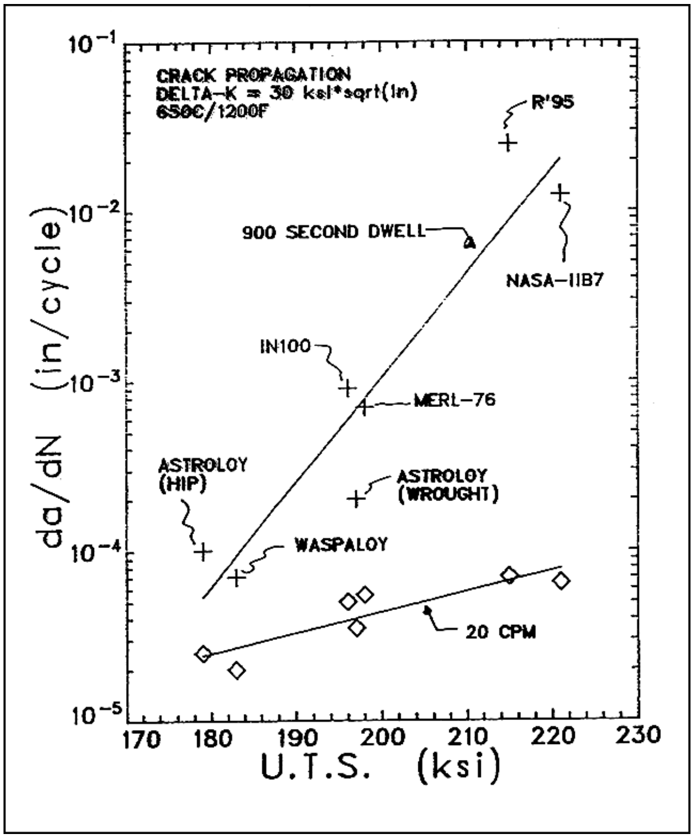

Figure 3: Correlation between strength and crack growth resistance over several Ni-base superalloys.

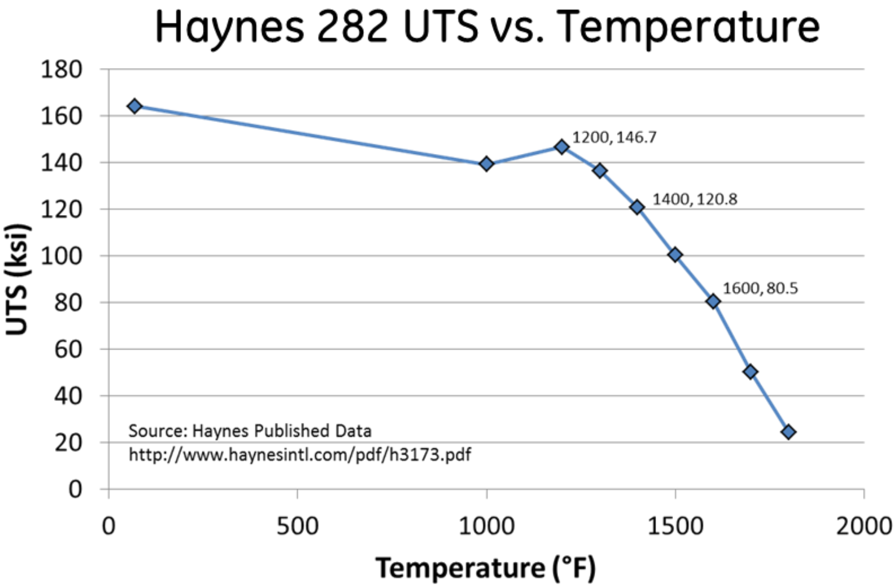

Source: Haynes Published Data
http://www.haynesintl.com/pdf/h3173.pdf

Figure 4: Effect of temperature on ultimate tensile strength of Alloy 282.

The objective of the study was to determine whether a correlation exists between oxidation and fatigue behavior in Alloy 282. The oxidation characteristics of the bulk material was compared to the crack-tip oxidation behavior. Given the lack of free surface and crack-tip oxidation in vacuum, similar analyses were not performed on specimens tested in the absence of environment.

The relative stability of metal oxides is related to their free energy of formation. Figure 5 represents an Ellingham diagram that illustrates the Gibbs free energy of formation of several relevant oxides, as a function of temperature. The lower the free energy of formation, the more stable is the oxide. For Alloy 282, the three oxides of most relevance are NiO, Cr_2O_3, and Al_2O_3. Based on the free energies of formation alone, one would expect Al_2O_3 to be the most prevalent oxide in the system. However, the kinetics of formation must also be considered. Under proper conditions of temperature and environment, NiO can form very rapidly in a relatively friable state, with a tendency toward void formation.

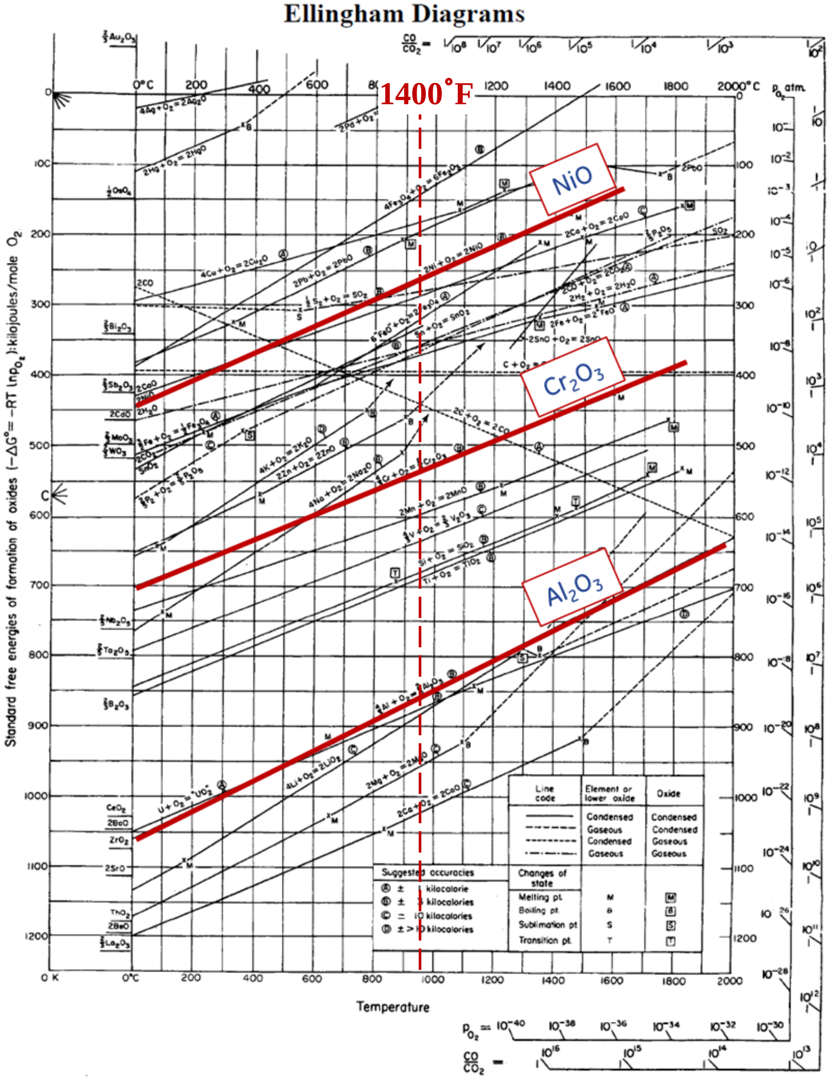

Figure 5: Ellingham diagram indicating equilibrium oxide free energies of formation. Source: http://web.mit.edu/2.813/www/readings/Ellingham_diagrams.pdf

With the exception of the presence of NiO in air, the free surface oxide constituents of specimens tested at 1400°F and 1600°F in air vs. steam appear comparable (Figure 6). In each case, there is considerable Al_2O_3 internal oxidation with a resultant sub-surface layer depleted in gamma prime. The majority of the free-surface oxides indexed to hexagonal Cr_2O_3 in air and steam at both temperatures. In all cases, discontinuous nodules of a Ti-oxide indexing to rutile were observed at the outer-most surface of the oxide layer (Figure 7).

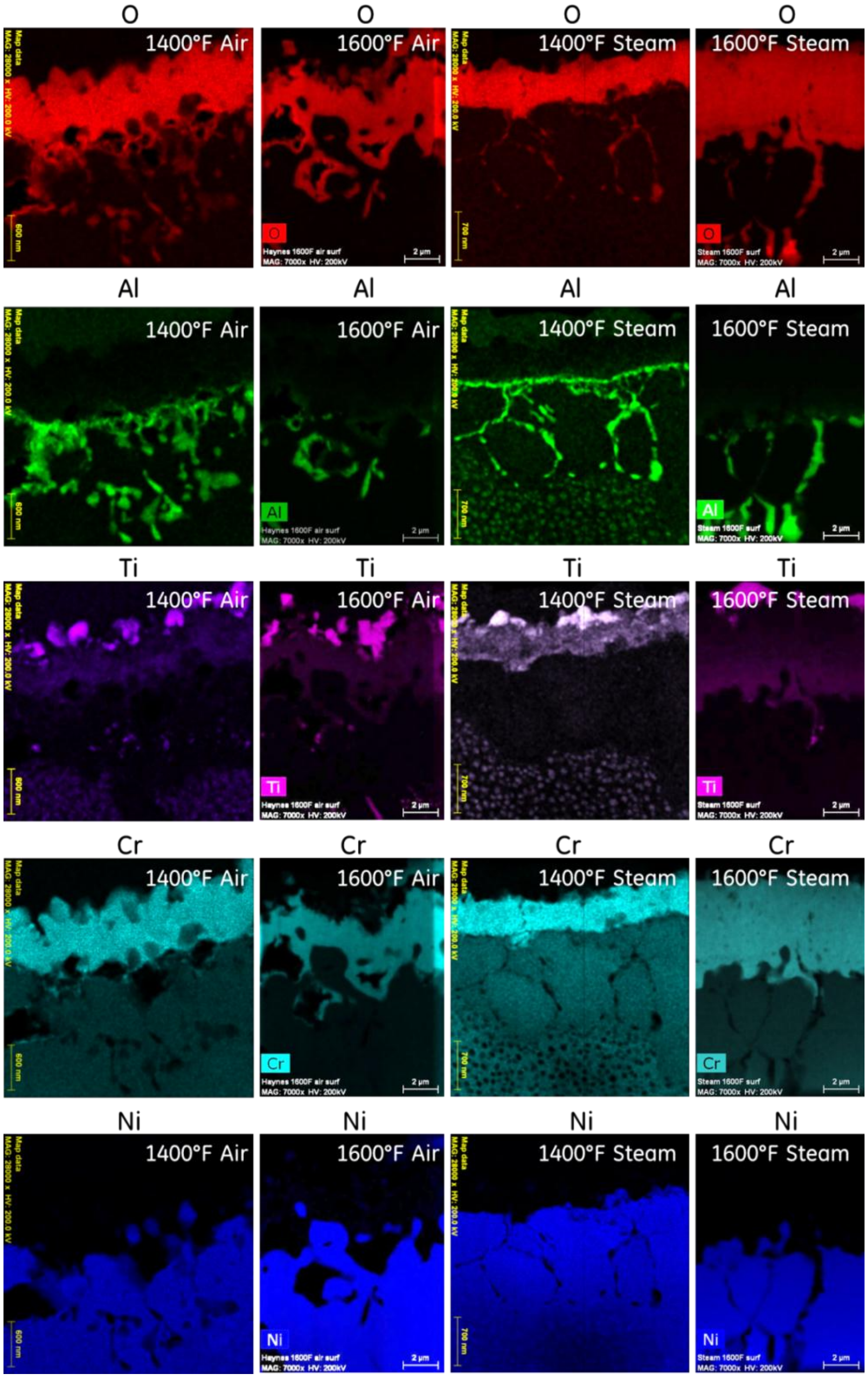

Figure 6: X-ray elemental maps indicating the chemical distribution of elements at the free surface of C(T) specimens tested at 1400°F and 1600°F in air and steam.

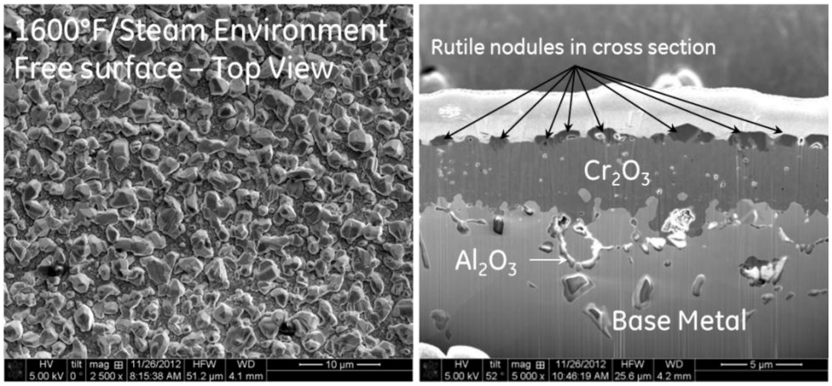

(a) (b)

Figure 7: Oxide character of a compact tension specimen tested in steam at 1600°F (a) at the free surface, away from the crack and (b) in cross-section, away from the crack.

One consistent difference between the oxide characteristics in air vs. steam is the apparent density of the oxide layer. In steam at 1400°F and 1600°F, the Cr_2O_3 layer appears dense, thick, and adherent. In contrast, in air at 1400°F and 1600°F, the Cr_2O_3 layer appears porous and friable at the outer-most surface, and near the base metal interface. This is most evident in the oxygen and chromium maps of Figure 6, and the FIB-liftout images of Figure 8, taken at the free surface. Similar observations are made near the crack tips of these specimens, as in Figure 9. The cause of the reduced oxide density in air is related to the early formation of NiO, which has a high vacancy concentration and a tendency toward forming microcracks and pores. The lower partial pressure of oxygen in steam suppresses the formation of NiO, and therefore results in a more dense oxide scale.

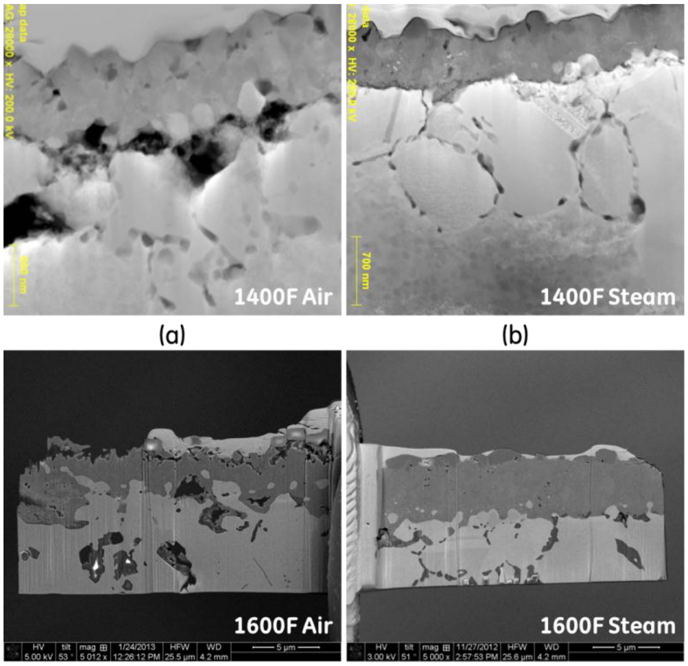

(a) (b)

(c) (d)

Figure 8: FIB-liftout specimens taken from the free-surface of compact tension specimens tested at 1400°F in (a) air and (b) steam, and at 1600°F in (c) air and (d) steam.

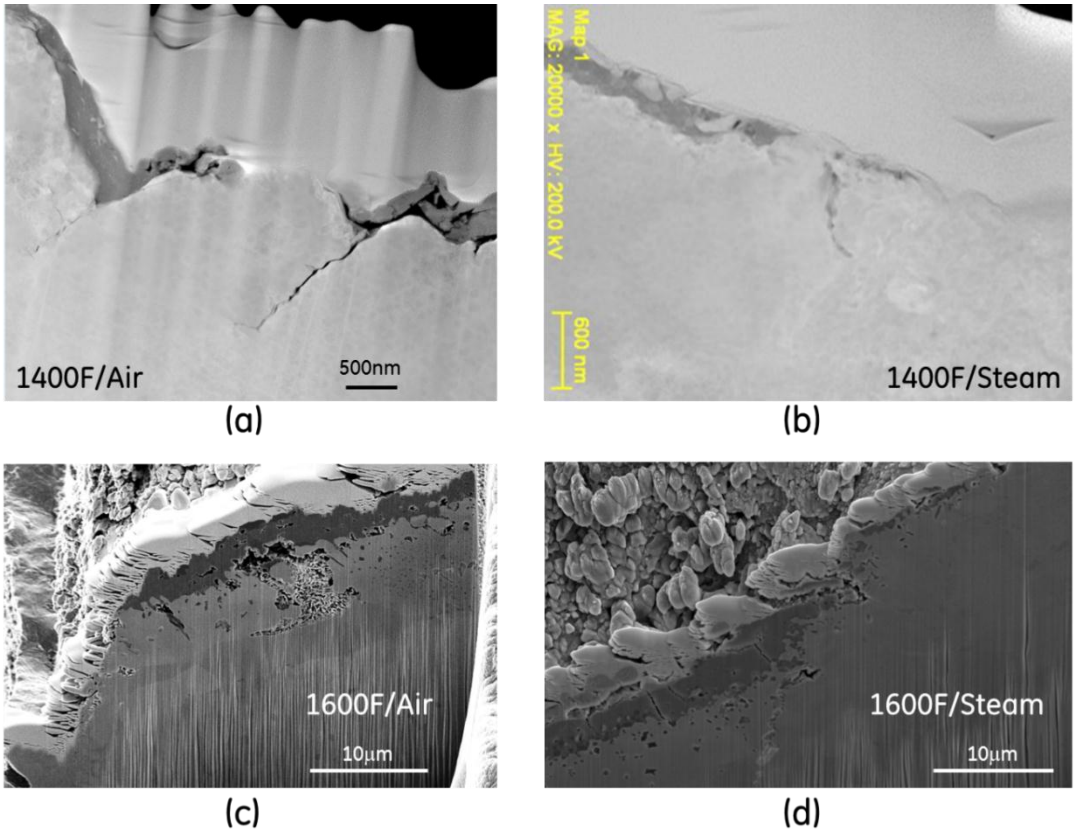

Figure 9: FIB cross-sections taken at the crack tips of compact tension specimens tested at 1400°F in (a) air and (b) steam, and at 1600°F in (c) air and (d) steam.

Two potential consequences arise from the observed differences in oxide density: 1) Crack path tortuosity is increased in specimens tested in air, which tends to promote crack closure and reduced crack growth rates. 2) The character of the oxides developed in air promotes a more compliant structure which may more effectively accommodate crack tip plasticity, and reduce growth rates. Additionally, for specimens tested at 1400°F in air, there is no evidence of Al_2O_3 or Cr_2O_3 formation at the tip of the crack (Figure 10). As a result, there is no gamma prime depletion at the crack tip. In 1400°F steam, the crack tip oxides characterized contain a larger fraction of aluminum and titanium, in addition to a Ni-Cr-Co rich oxide. This suggests that Al_2O_3 and Cr_2O_3 form earlier at the crack tip in steam than in air at 1400°F. The consequence of earlier alumina formation in steam (and the absence of a friable NiO layer) is a less compliant crack-tip oxide, with a reduced level of crack path tortuosity (Figure 9). Both account for the observed increase in crack growth rate in steam at 1400°F, relative to the 1400°F air behavior (Figure 1b).

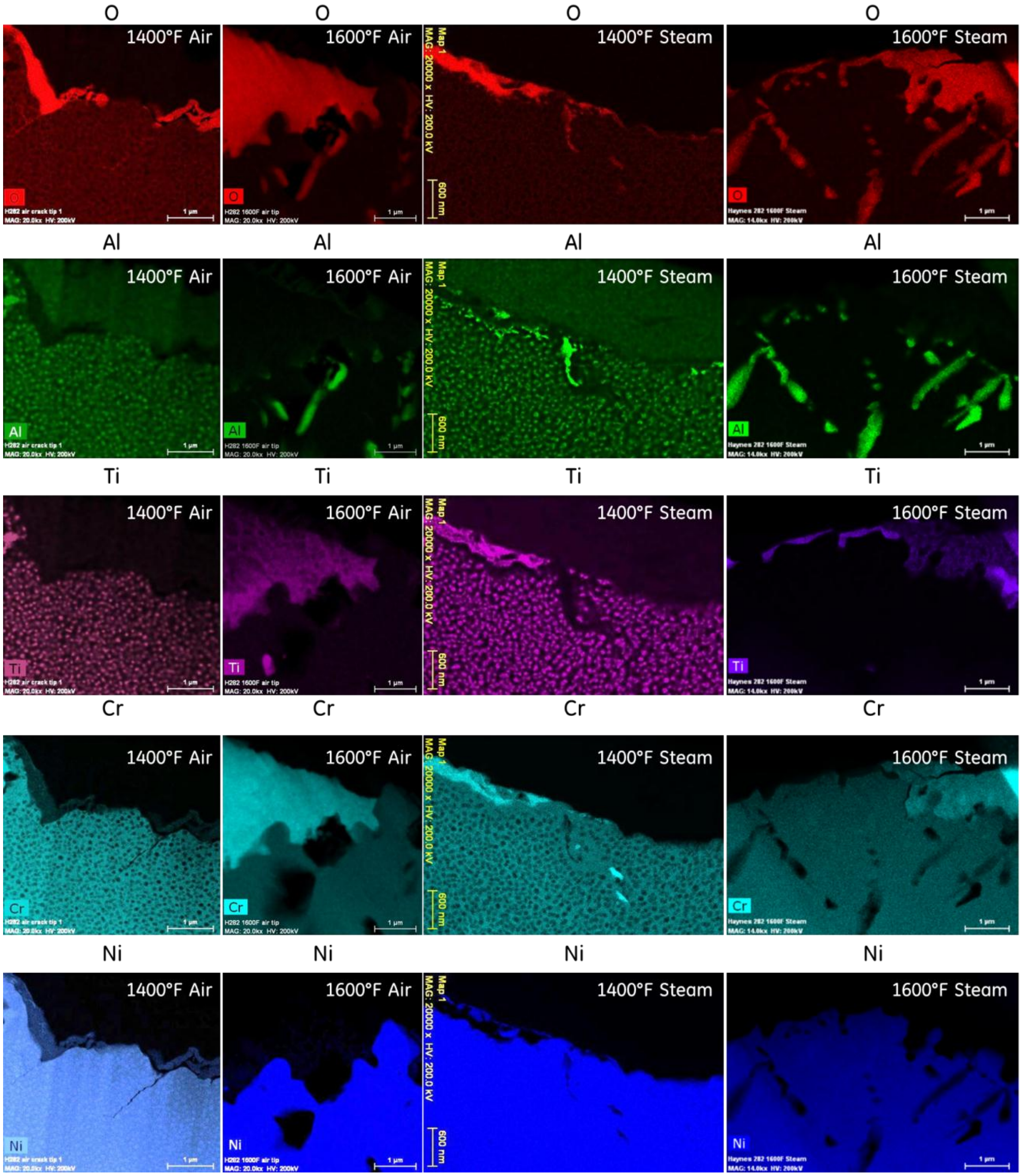

Figure 10: X-ray elemental maps indicating the chemical distribution of elements at the crack tips of C(T) specimens tested at 1400°F and 1600°F in air and steam.

At 1600°F, the rates of crack growth in air and steam converge. Figure 10 illustrates that under 1600°F/air conditions, the formation of *crack-tip* Al_2O_3 and Cr_2O_3 is no longer suppressed. Figure 9 and Figure 10 also indicate that the *crack-tip* oxide character in both air and steam appear similarly dense, inferring that the NiO formation in 1600°F air is delayed at the crack tip, but forms in the wake of the advancing crack. The convergence of growth rates in 1600°F air and 1600°F steam conditions (Figure 11c) can therefore be rationalized based on the fact that that the crack-tip oxide constituents and oxide density appear comparable in both environments at that temperature, in addition to a more dominant creep-fatigue interaction at that temperature.

Figure 11 depicts the crack growth behavior with an overlay of the predominant crack tip oxides present at each condition. It can be concluded that for scenarios with friable NiO formation at the crack tip, crack growth rates are generally reduced. For combinations of temperature and environment where Al_2O_3 and Cr_2O_3 are promoted at the crack tip, growth rates are accelerated due to the less compliant structure, and less tortuous crack path. Under conditions of equivalent crack tip oxide character (Figure 11f), the role of strength vs. temperature and the onset of a creep-fatigue interaction at 1600°F tend to dictate the overall fatigue performance. The relations developed between crack-tip oxidation characteristics and crack growth behavior have been delivered to Task 6 to facilitate improved crack growth predictive capability.

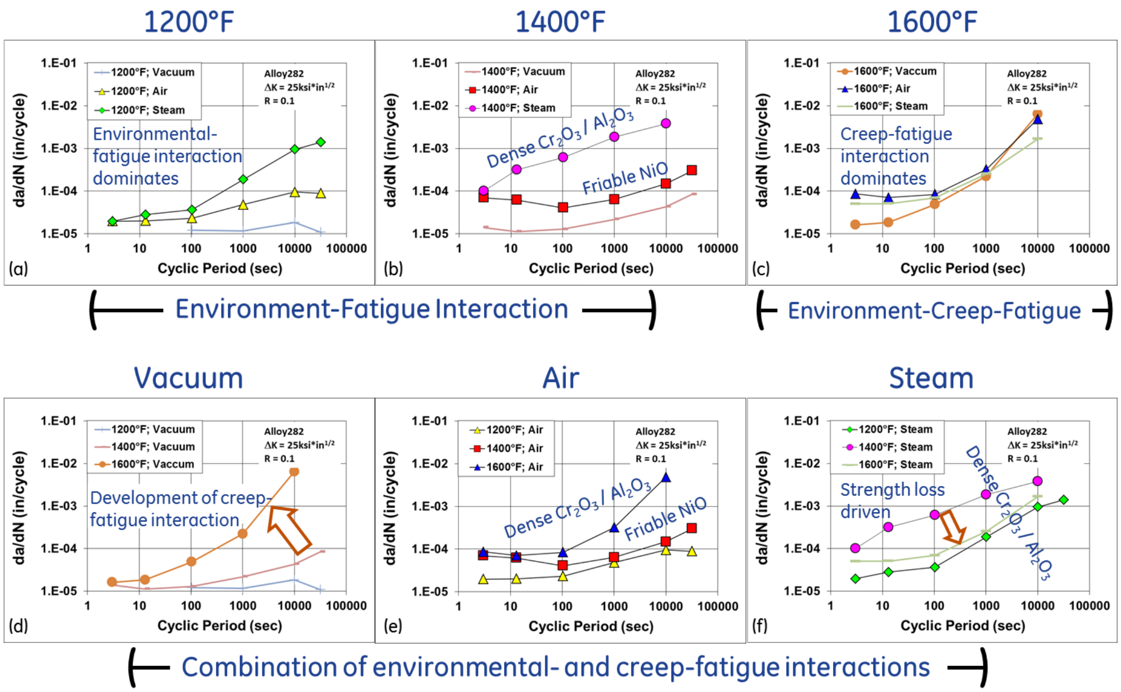

Figure 11: Alloy 282 hold-time sweep test results as a function of cyclic period, temperature, and environment.

Task 3: Atomistic and first principles modeling of crack tip oxygen embrittlement

The effect of oxygen on crack growth of a Ni-based superalloy has been proposed with two major mechanisms in literature: stress accelerated grain boundary oxidation and dynamic embrittlement[1-3]. We first review these two mechanisms. We propose that monolayer spreading of oxygen atoms in the metal-metal grain boundaries (GB) results in a significant reduction of mechanical cohesion that dominates the oxygen embrittlement effect. We then present computational data based on first-principles calculations to support this hypothesis. We find that oxygen transports more favorably through the grain boundaries than that in the metal bulk lattice, because of the lower formation energies and the “repairing” effect mediated by oxygen in the metal grain boundaries. Such absorption may initiate a metastable oxide monolayer phase that significantly decreases the mechanical strength of nickel alloys. We quantify such effects on the cohesion strength of metal grain boundaries. We further study the diffusion kinetics of oxygen in the nickel lattice, and perform first-principles modeling to calculate the oxygen diffusivity in both the crystalline and amorphous Ni phases. In addition, we calculate the ideal strength of hydrolyzed chromia, which is found to be significantly lower than that of chromia. The results indicate that the protective function of chromia to the nickel alloy may be highly weakened under the hydrolysis condition.

3.1. Stress accelerated grain boundary oxidation (SAGBO) versus dynamic embrittlement (DE)

SAGBO, shown in the upper portion of Figure 12, states that an oxide wedge is preferentially formed down the grain boundary: (a) This oxide cracks under mechanical stresses, (b) the oxides then further penetrate down the boundary, and (c) the process is repeated. This mechanism involves formation of bulk oxides in grain boundaries. Crack growth is accompanied with the fracture of an oxidized grain boundary ahead of a crack tip. The tensile stress normal to the plane of the oxide assists the oxide formation. The *dynamic embrittlement* mechanism, shown in the lower portion of Figure 12, suggests that the grain boundary is embrittled by oxygen penetration in the near surface region: (a) The embrittled boundary fails in tension, (b) and the free surfaces thus are oxidized, and (c) while oxygen diffuses down the boundary at the head of the crack the next segment is embrittled and this process repeated. In this picture, embrittlement occurs by grain boundary diffusion of oxygen ahead of a crack tip, causing decohesion and consequently cracking of the grain boundary under load[4]. Thus, cracking by oxygen embrittlement is correlated with percolation of a thin layer of oxygen atoms, which forms a damage zone ahead of a crack tip.

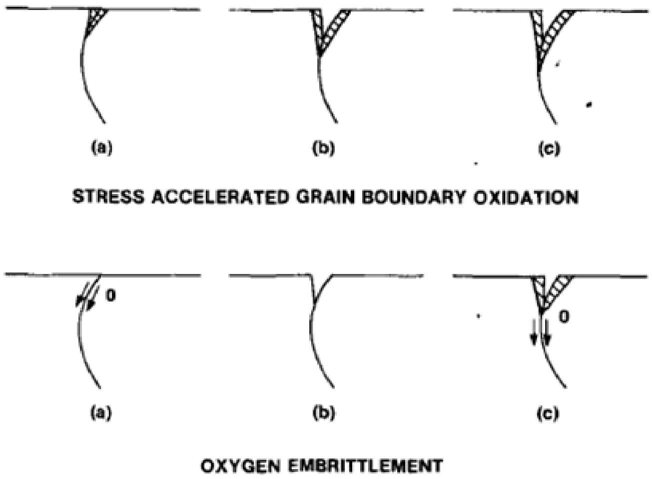

Figure 12: Stress accelerated grain boundary oxidation versus oxygen embrittlement [1].

The argument of these mechanisms comes down to the comparison of the thermodynamic stability, as well as the kinetics of the 2D monolayer oxides and the 3D bulk oxides – the diffusive time of oxygen monolayers through the grain boundaries versus the nucleation time of the bulk phase.

Here we use the language of solution thermodynamics and phase transformation to describe the distribution of oxygen in an originally metallically-bonded polycrystal. As illustrated in Figure 13, there are basically four types of "living conditions", or phases, that oxygen can find themselves in:

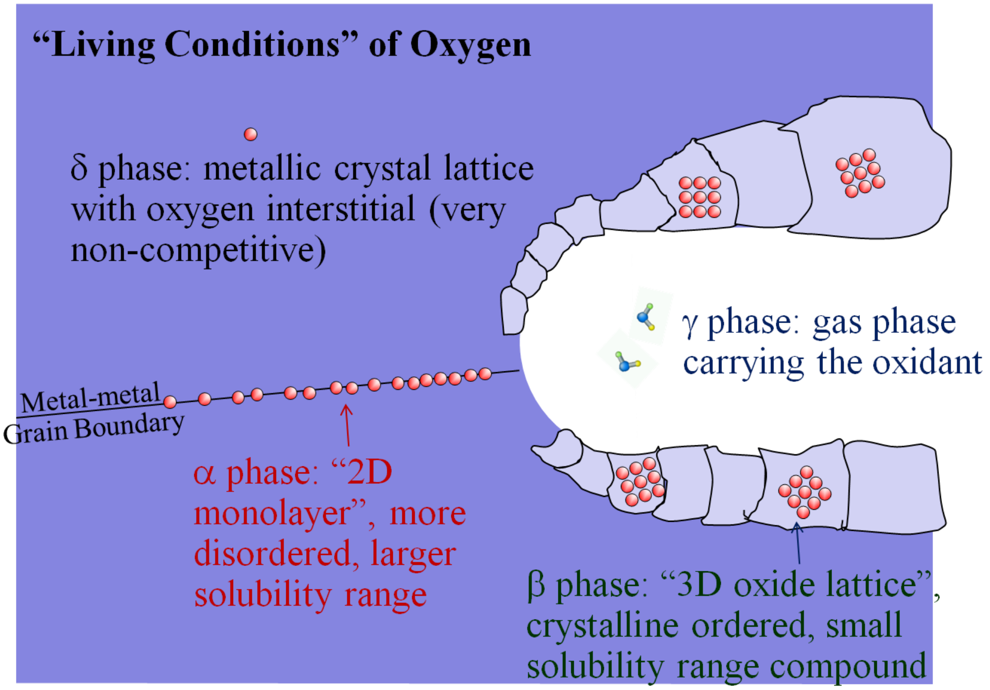

Figure 13: Living conditions of oxygen in an originally metallically-bonded polycrystal.

α phase: This is the hypothesized phase behind dynamic embrittlement. Oxygen atoms find suitable spots right inside the metal-metal grain boundary. As a grain-boundary-absorbed phase, similar to surface adsorption (Langmuir isotherm) of gaseous molecules, structurally the α phase should be more "2D" and monolayer (ML) like, and should be disordered at the application temperature, similar to the surface pre-melting layer. The thermodynamic description should follow that of Gibbs absorption isotherm and interfacial excess. Because of the disordered 2D structure at high temperature, the chemical miscibility or solubility range should be larger than that of compounds.

β phase: This is the oxide phase behind the proposed SAGBO mechanism. By oxide phase, we mean 3D chemically and structurally ordered crystalline compound lattice. For something to be called oxide, the thinnest dimension should extend more than ten monolayers, and the different layers should be packed in a highly ordered fashion. We can have multiple oxide phases, such as NiO and Ni_2O_3, in which case we will call them β and β' phases. These compounds should form sharp and deep lines in the Gibbs free energy versus composition plot (Figure 14), centered at rational values of stoichiometry such as 1:1 or 2:3.

γ phase: This is the environmental gas phase that carries the oxidant, where the external control (such as pO_2) comes in.

δ phase: This is essentially the original metallic lattice. Oxygen usually finds itself not very welcome in the original metallic lattice structure, so the concentration of oxygen dissolved in metallic lattices (with the exception of HCP Ti and Zr) is usually very low. δ phase is certainly non-competitive against the α phase, as Figure 13 shows.

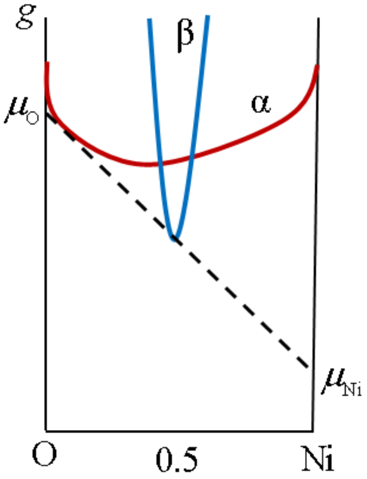

Figure 14: Schematic Gibbs free energy vs. composition.

The relative thermodynamic stability and oxidant mobility in α phase and β phase are the keys to the discussion of whether the embrittlement mechanism is SAGBO or DE. Put plainly, the two questions are:

Question A: Does oxygen ion (or oxygen-carrying species) diffuse faster in α, or in β phase?

Note the complication to this question is that α phase may have a wide range of chemistry, X^{α}, so the dependence of oxygen mobility M^{α} on X^{α} should be modeled. We generally expect that M^{α} should decrease with increasing X^{α}, that is, the more degree of prior oxygenation, the slower the newly injected oxygen can diffuse along the "dirty GB" α phase, as the previous oxygen would be "roadblock" to the new oxygen addition.

Question B: Is α phase just metastable or globally stable, against the formation of β phase?

Note rigorously speaking this a wrong question, since the $kT(X^{\alpha}\ln X^{\alpha} + (1-X^{\alpha})\ln(1-X^{\alpha}))$ entropic free energy term would allow α phase to always possess a finite amount of X^{α} in any two-phase equilibrium with β. But the practical question is whether the X^{α} would be so small that the mechanical effect of α phase becomes negligible.

Here we note that, from a mechanical viewpoint, as long as the α phase composition in the grain boundaries $X^{\alpha G} > 0.1$ or so (we use the grain boundary composition $X^{\alpha G}$ in order to differentiate from the bulk composition X^{α}), the α phase should be able to substantially embrittle the GB. One does not need tens or hundreds of layers of oxygen to change the GB decohesion behavior. 1 ML, or even a fraction of monolayer, should be able to sufficiently influence the local GB decohesion characteristics. Similarly, the dislocation-GB interaction characteristics should be changed with $X^{\alpha G} > 0.1$ or so. As the plastic work term dominates in the fracture energy of metals, the effect of $X^{\alpha G}$ on dislocation plasticity is probably even more important than the effect of $X^{\alpha G}$ on GB decohesion energy. A dislocation transmitting through the GB should be able to tell a purely metallic GB from a "dirty GB" with 10% oxygen in it. In particular, the ability of the GB to store dislocation content before eventual debonding should be severely impaired after 10% oxygen absorption. One does not need tens of layers of oxide for this to happen.

A reasonable scenario is described below, based on speculative answers to Question A ("oxygen does diffuse faster in α phase than in β phase, since there is larger free volume in α") and Question B ("α phase is quite metastable against β phase for most of the composition range; but β phase needs some time to nucleate"). In this scenario, whether we have α-controlled DE or β-controlled SAGBO depends on a quantitative comparison of two time scales: the diffusive time of oxygen monolayers through the grain boundaries versus the nucleation time of β phase. Certainly, when a sample is under cyclic load fatigue test, another two (2) time scales emerge: the time scale of crack growth, and the cyclic period. The size of the oxygen monolayers (α phase) are dependent on all the four (4) time scales. For simplicity, let us focus our discussion on the comparison of the diffusive time of oxygen monolayers versus the nucleation time of β phase.

The general scenario is following. The 2D α phase is not the globally optimal arrangement for oxygen: it is just a chaotic, temporary living arrangement, but in which oxygen find more comfortable than in the γ phase or δ phase. A significant amount of oxygen can percolate through the "dirty GBs", i.e. α phase, if nothing shuts the oxygen source off. But in their hearts, the oxygen atoms crave the ordered 3D β phase. Given enough time and concentration, the oxygen atoms in α will incite a revolution that involves significant rearrangements of the metal atoms. This would be the nucleation event of the β phase, and is also a 2D→3D transition. Once the 3D β phase is nucleated, because of the much reduced oxygen diffusivity in β, it will largely shut off the oxygen flux into the metal. In this sense, β phase protects the metal. Once β phase is nucleated at crack tip, the previously extended α phase (with supersaturation of X^{α}) into the metal would actually "shrink", and its mechanical effect (DE) becoming less and less with time.

According to the scenario above, if β phase takes long time to nucleate (which is possible, since significant metal rearrangements are needed along with oxygen rearrangements, and any 2D→3D transition is going to be complicated), then the α phase, with its thermodynamically supersaturated oxygen coverage, can wreak havoc mechanically inside the polycrystal by DE. $X^{\alpha G} > 0.1$ could extend tens or even hundreds of nanometers into the grain boundary network. In this case, the metal can crack first along the "dirty GB", far ahead of the oxide that forms later.

On the other hand, if the β phase nucleates easily, or there is fast growth and coalescence of prior βs, the α phase will not have sufficient time to achieve DE state (as the $X^{\alpha} > 0.1$ region extends no more than a few Angstroms? nanometers?). In this case, we will have SAGBO mechanism: the 3D oxide forms along GB first, and is cracked later when the β phase thickens and stores enough elastic energy to drive brittle cleavage cracking.

Here we provide the computational results to illustrate the thermodynamic stabilities of the α, β, and δ phases based on first-principle calculations.

3.2. Models and computational methods:

Crystalline Ni (c-Ni) structure was modeled as a $2 \times 2 \times 2$ supercell of the conventional cubic cell that contains 32 atoms. A lattice constant 3.52 Å was obtained after energy minimization. We calculated the cohesive energy of Ni as -5.58 eV. We further calculated the tetrahedron volume to characterize the structural feature. For c-Ni, the tetrahedron volume was found as 1.82 Å^3. The atomic structure of the Ni supercell is shown in Figure 15(a).

To model a Ni grain boundary, we built an atomic structure by tilting the crystallographic [100] axis with respect to the (100) plane. After energy minimization, Ni atoms rearranged and formed an amorphous structure (a-Ni). The lattice constants were a=3.55 Å, b=19.18 Å, c=9.52 Å, and it contains 56 atoms. The cohesive energy of the GB structure after energy minimization was -5.40 eV. The tetrahedron volumes were in the range [0.27, 3.46] Å^3. The initial and the final configuration are shown in Figure 15(b).

For the crystalline NiO (c-NiO), we modeled a $2 \times 2 \times 2$ supercell that contained 64 atoms. A lattice constant 8.34 Å was obtained. The cohesive energy was calculated as -5.75 eV, and the tetrahedron volume in this structure was 1.51 Å^3. The atomic configuration is shown in Figure 15(c).

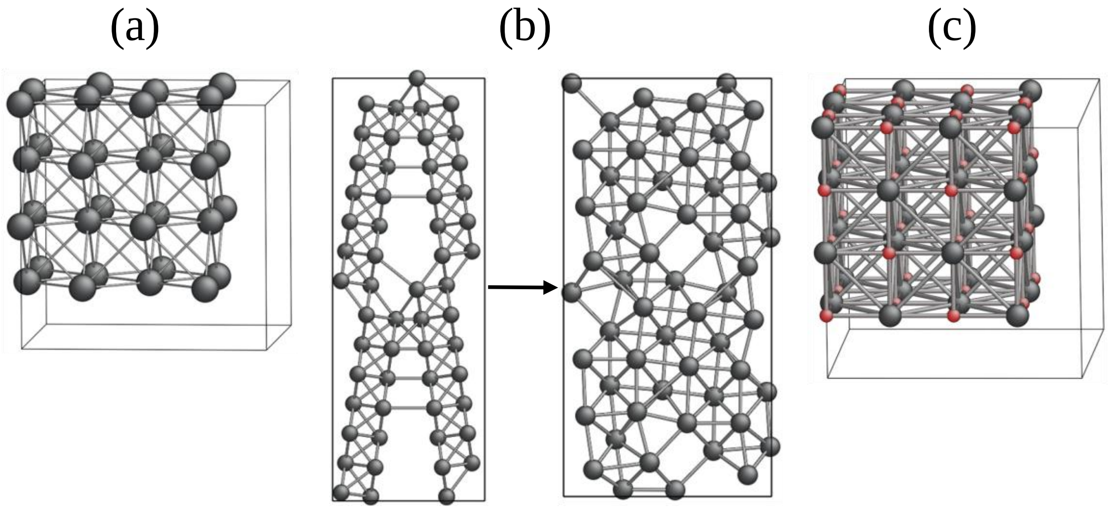

Figure 15: The configurations of (a) the supercell of c-Ni, (b) the initial structure of a Ni GB and the final structure after energy minimization, and (c) the supercell of c-NiO. The grey spheres are Ni atoms, and the red spheres are oxygen atoms.

Density functional theory (DFT) calculations were performed using Vienna Ab-initio Simulation Package (VASP). The plan-wave cut off energy was set as 400 eV for all calculations. $5 \times 5 \times 5$, $9 \times 2 \times 4$, and $4 \times 4 \times 4$ Monkhost-Pack meshes were used to model the Brillouin zone in the reciprocal space for c-Ni, a-Ni, and c-NiO, respectively.

For an FCC structure, the tetragonal and octagonal sites are the interstitial sites for oxygen insertion. To calculate the formation energies and the free energies at different oxygen concentrations, we systematically varied oxygen concentration by placing oxygen at the interstitial sites. For the crystalline phases (α phase and δ phase), the insertion sites can easily be identified. For the GB structure (β phase) with an amorphous nature, we performed Delaunay triangulation to find the largest void size to accommodate the insertion of oxygen.

3.3. Thermodynamic stabilities

We calculated the formation energies of oxygen in c-Ni (α phase) and a-Ni (β phase). In the calculation of the formation energy, we took the energy of an atom in c-Ni (a-Ni) (E_{Ni}) and the energy of an isolated O atom (E_{O}) as the reference energies, with $E_{n\mathrm{O\text{-}Ni}}$ being the total energy of the system containing n O atoms in the cell. The formation energy per O atom $E_f(n)$ was calculated as $E_f(n) = (E_{nO-Ni} - E_{Ni} - nE_O)/n$. Figure 16 shows the formation energies of oxygen in c-Ni and a-Ni. It is evident that oxygen is more favorably absorbed in the grain boundary compared to that in the bulk crystalline lattice at low oxygen concentration (X_{O}<0.4, where $X_O = N_O/(N_{Ni} + N_O)$). At relatively high oxygen concentrations, the formation energies show little difference because of the dramatic structural rearrangement caused by oxygen insertion, and that oxygen may not be able to differentiate its environment. We further calculated the specific free energies of different phases to compare the thermodynamic stability. The results are shown in Figure 17.

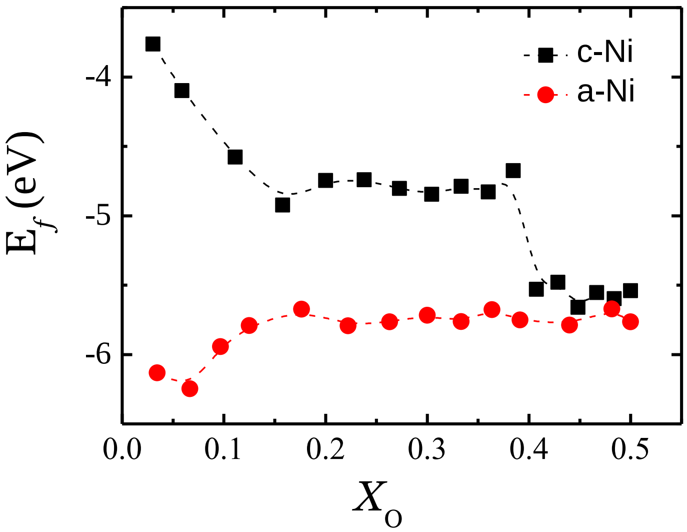

Figure 16: Formation energies of oxygen in c-Ni and a-Ni. The solid symbols represent the calculation data. The lines connecting the data are guide for the eyes.

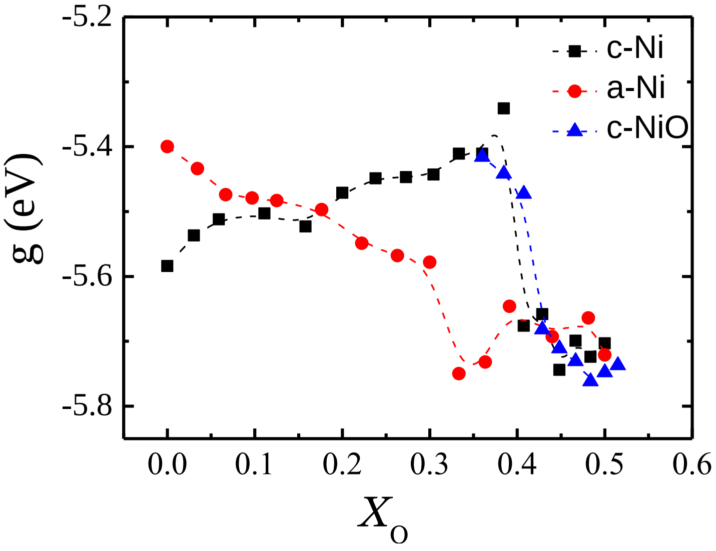

Figure 17: The specific free energies as a function of the oxygen concentration.

It is noteworthy that, the energy difference at zero oxygen concentration between c-Ni and a-Ni may represent the grain boundary formation energy. As oxygen concentration increases, the free energy of c-Ni increases since the oxygen atoms mostly feel uncomfortable in the crystalline lattice. However, the free energy of a-Ni decreases with oxygen insertion as the oxygen atoms may mediate the amorphous structure to find a lower energetic state. When the oxygen concentration is close to 0.5, the interactions of Ni and O atoms may invoke the local characteristics of the bulk oxide (valence state, coordination number, etc.), and the system free energies drop and are close to that of the crystalline NiO. At X_O=0.5, the crystalline NiO preserves the lowest energy state, and by varying the oxygen concentration, the free energy shows the needle-like behavior as we sketched in the *g*-*X* relation in Figure 14.

We have thus far confirmed that oxygen transports more favorably through the grain boundaries because of the lower formation energies and the “repairing” effect mediated by oxygen. Such absorption may initiate the oxide monolayer that dominates the mechanical behavior of nickel oxides.

3.4. Mechanical embrittlement on the strength of metal grain boundaries

To quantify the embrittlement effect on cohesion strength due to the presence of oxide monolayer in metal grain boundaries, we performed uniaxial simulations of various Ni structures containing different oxygen concentrations. In the simulation of uniaxial tension, we prescribed a given strain along the *z*-direction of the structure, and measured the nominal stress simultaneously. For a material under tension, it undergoes either plastic flow or fracture at elevated level of strain, depending on the relative strength of plastic yielding and fracture of the structure. According to linear elastic fracture mechanics, for a penny-shape crack embedded in a matrix of infinite size, under mode-I load the maximum tensile stress $\sigma_{max} = K_I/\sqrt{2\pi r}$, the maximum shear stress $\tau_{max} = \sqrt{2}K_I/\sqrt{27\pi r}$, and the ratio of these values is about 2.6. We may estimate that, for a material with such a ratio smaller than 2.6, it would undergo fracture under uniaxial tension, and when the ratio is larger than 2.6, it would reach plastic yielding before fracture occurs. To capture the fracture event in the oxidized Ni and obtain the ideal fracture strength, we froze the deformation in the *x*- and *y*-direction, and only allowed atoms to relax along the *z*-direction. In such simulations, we suppress the plastic yielding that is mediated by continuous bond switching and reforming, and force the atoms to overcome the barrier of fracture and break the atomic bonding. The stress-strain curves for example systems of c-Ni, a-Ni, and c-NiO are shown in Figure 18.

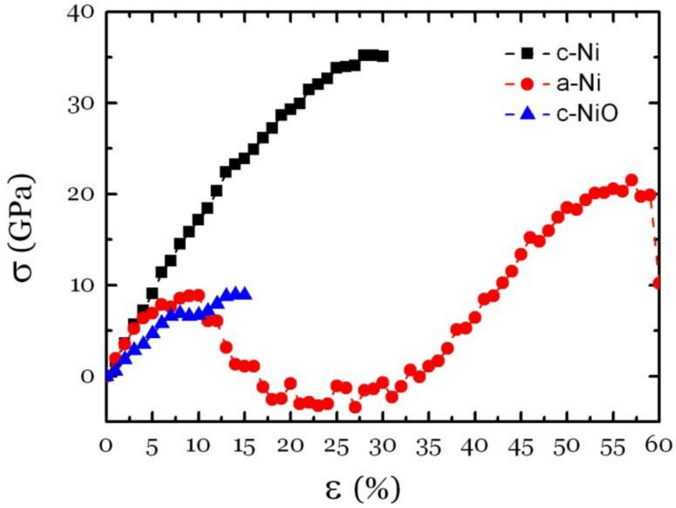

Figure 18: Stress-strain curves for the example systems of c-Ni, a-Ni and c-NiO. The solid symbols represent the calculation data. The lines connecting the data are guide for the eyes.

We see that for the crystalline structures of c-Ni and c-NiO, before the stress reaches the respective peak values, the materials experience elastic deformation and the crystalline configurations are preserved. At the critical stress (strain), the atomic bonding is broken and the corresponding peak stress represents the ideal strength of the structure. Notably the ideal strength of c-NiO is significantly lower than that of c-Ni, by a factor of four. This may be due to a weaker Ni-O bonding as compared to the pure metal bonding.

In comparison, for the a-Ni lattice, a significant structure reconstruction is observed during loading. In the initial stage of load ($\epsilon < 10\%$), the crystal structure experiences elastic deformation that mainly involves bond stretching. By increasing applied strain, the stress drops dramatically. Such a drop corresponds to the subsequent reconstruction of the atomistic structure – a change mainly mediated by atomic bond switching and stimulated by the applied mechanical load. With further increased applied strain, the stress increases linearly up to a critical value. We take the maximum stress at which the structure can sustain as the ideal strength. Here we show the atomic configurations in Figure 19, to illustrate the initial structure before applying strain and after fracture.

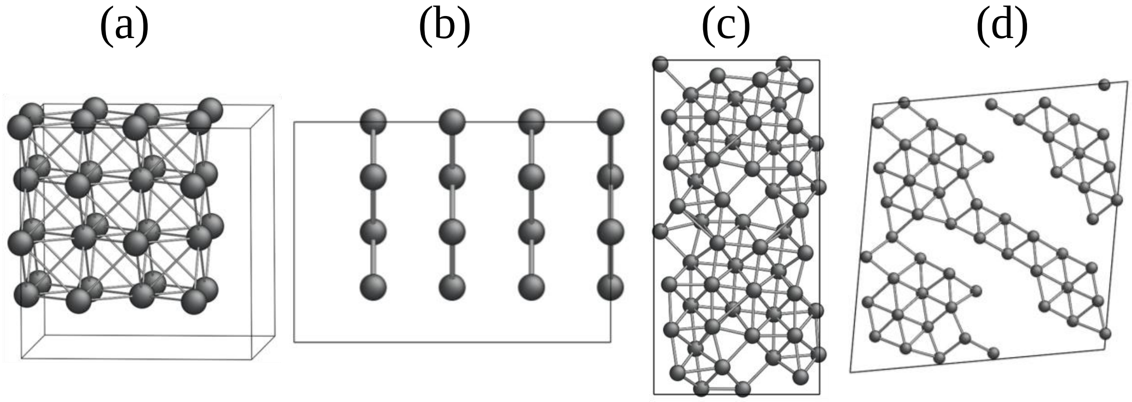

Figure 19: The atomic configurations of (a) the supercell of c-Ni, (b) c-Ni after fracture, (c) the initial structure of a-Ni, and (d) a-Ni after fracture.

As we have argued in the previous section, the composition of the monolayer oxide (α phase) at equilibrium might be a small number. However, even when the bulk composition is very low, the grain boundary composition can be sufficiently high. From a mechanical viewpoint, as long as the α phase composition in the grain boundaries $X^{\alpha G} > 0.1$ or so, the α phase could severely embrittle the GB. A fraction of monolayer could severely influence the local GB decohesion characteristics. One does not need tens or hundreds of layers of oxygen to change the GB decohesion behavior. Here we performed uniaxial tensile simulations until fracture occurred to the a-Ni grain boundaries with various oxygen concentrations, to obtain the dependence of the ideal strength on the oxygen concentration. The evolution of the ideal strength is shown in Figure 20.

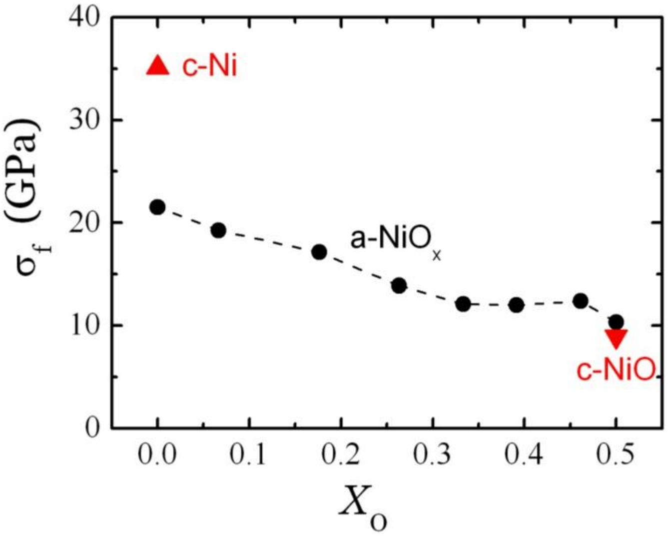

Figure 20: Ideal fracture strength of Ni with various oxygen concentrations. The a-NiO$_x$ represents the monolayer oxide (α phase) in the Ni grain boundaries. The solid symbols are the calculation data, and the dashed lines are guide for the eyes.

It is clearly seen that the ideal fracture strength of both crystalline and amorphous Ni decrease as more oxygen is present in the lattice. For the amorphous structure, the fracture strength decreases by a factor of two, when oxygen concentration increases from 0.07 to 0.5. We have examined the microscopic mechanism of such behavior. Compared with the pristine Ni network, the presence of oxygen breaks certain numbers of Ni-Ni bonds but a well-defined network still exists and spans the size of the supercell. The inhomogeneous distribution of oxygen leaves certain Ni bonds more disturbed than others, and causes locally less close-packed structures. Such topological feature may share the same characteristics in glassy materials – the amorphous network consists of tightly bonded clusters, which form the backbone of the structure, and loosely bonded free-volume regions, which act as flow defects and behave liquid-likely responding to the external mechanical load. The flow defects may be caged by the tightly bonded surroundings, which constitute the basic topological feature of the atomic structure. Under mechanical load, the deformation is mainly localized in the loosely packed regions (weak regions) while the backbone (strong regions) behaves elastically. Such deformation behavior is also evidenced in oxidized Ni, as shown in Figure 21. In the course of deformation, it is mainly accommodated by local weak Ni-O regions and eventually fracture occurs in those places.

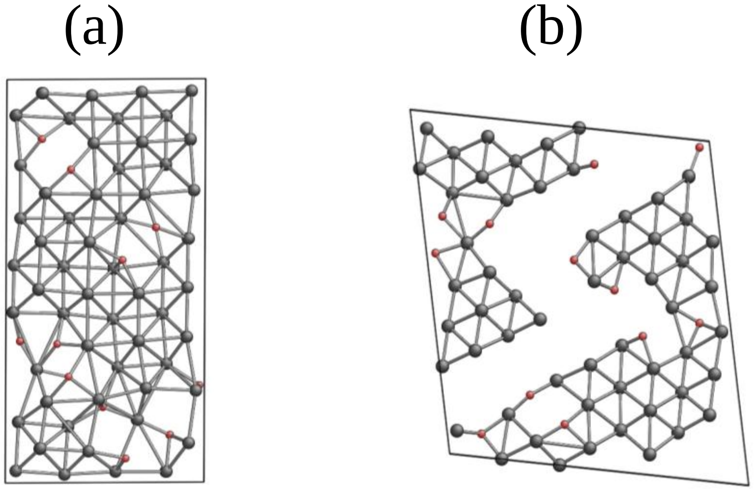

Figure 21: The configurations of (a) a-$NiO_{0.17}$ before applying strain, and (b) a-$NiO_{0.17}$ after fracture. The grey spheres are Ni atoms, and the red spheres are oxygen atoms.

In addition, we note that the ideal strength of c-Ni is much larger than that of the counterpart amorphous lattice, because the amorphous structure has a loosely packed atomic bonding. When the oxygen concentration approaches 0.5, the ideal strength of a-NiO_x is close to that of c-NiO. At relative high oxygen concentrations, the interactions of Ni and O atoms may develop the local characteristics of the bulk oxide such as the valence state and local coordination, such that the system behavior of the amorphous network is similar to that of the crystalline NiO.

In summary, here we have quantified the embrittlement of Ni grain boundaries due to the presence of oxygen monolayer by performing uniaxial tensile simulations. As oxygen concentration increases, the ideal fracture strength of a-NiO_x decreases dramatically. The results confirmed our previous hypothesis that a fraction of oxygen monolayer in the metal grain boundaries could severely influence the GB decohesion characteristics.

3.5. Diffusion kinetics of oxygen in Ni

The difference of DE and SAGBO mechanisms depends on the kinetic factors – primarily diffusion of oxygen along grain boundaries (GB) to form the monolayer α phase versus the nucleation of bulk oxide β phase. If β phase takes long time to nucleate relative to the fast diffusion of oxygen along grain boundaries, then the α phase**,** with its thermodynamically supersaturated oxygen coverage, can cause severe mechanical embrittlement inside the polycrystal by DE. Oxygen segregation may extend tens or even hundreds of nanometers into the grain boundary network. In this case, the metal can crack first along the “dirty GB” and the oxide will form later. On the other hand, if the β phase nucleates easily, or if fast growth and coalescence of prior βs occurs, the α phase will not have time to achieve a steady state of DE. In this case, we will have SAGBO, as the 3D oxide forms along GB first, and is cracked later when the β phase thickens and stores enough elastic energy to drive brittle cleavage cracking. Here we focused on the diffusion process of oxygen in the nickel lattice, and performed first-principles modeling to calculate the oxygen diffusivity in both the crystalline and amorphous Ni phases. We used the nudged elastic band method to calculate the energy barrier of elementary hops for a single oxygen atom in crystalline Ni, and we used the non-equilibrium ab-initio molecular dynamics to calculate the dependence of oxygen diffusivity on its concentration in the amorphous Ni lattice.

3.5.1. Oxygen diffusivity in crystalline Ni

In order to determine the diffusivity of oxygen in crystalline Ni, we calculated the activation energy along its diffusion trajectory. The minimum energy path with the saddle point of oxygen migration was determined by using the nudged elastic band (NEB) method. NEB is a method for finding saddle points and minimum energy paths between known reactants and products. The method works by optimizing a number of intermediate images along the reaction path. Each image finds the lowest energy states while maintaining equal spacing to neighboring images. This constrained optimization is done by adding spring forces along the band between images and by projecting out the component of the force due to the potential perpendicular to the band. We also implemented the climbing image in which the highest energy image is driven up to the saddle point. In this modification, the image does not feel the spring forces along the band. Instead, the true force at this image along the tangent is inverted. The image tries to maximize its energy along the band, and minimize in all other directions. When this image converges, it will be at the exact saddle point. We sampled the diffusion pathway with an NEB path consisting of seven intermediate configurations. The NEB path was first constructed by linear interpolation of the atomic coordinates. Then, the path was relaxed until the force on each atom was smaller than 0.01 eV/ Å. The shape and volume of the cell were fixed during the NEB calculation.

Before the NEB calculation, we first relaxed the crystal lattice using a conjugate-gradient algorithm that all ions were allowed to relax while both the supercell volume and shape could be changed. Here we modeled the c-Ni structure as a $2 \times 2 \times 2$ supercell of the conventional cubic cell that contains 32 atoms. Oxygen diffuses interstitially in the Ni lattice. For the interstitial diffusion in an FCC structure, the octahedral site is the most stable state, while the tetrahedral site is a metastable position for oxygen insertion. Diffusing interstitial oxygen atom can be equilibrated at the metastable tetrahedral sites temporarily and jumps forward and backward to a neighboring octahedral site. Therefore, the major diffusion of oxygen passes through adjacent tetrahedral sites via a tetrahedral site in c-Ni, as represented by the red arrows in Figure 22(a).

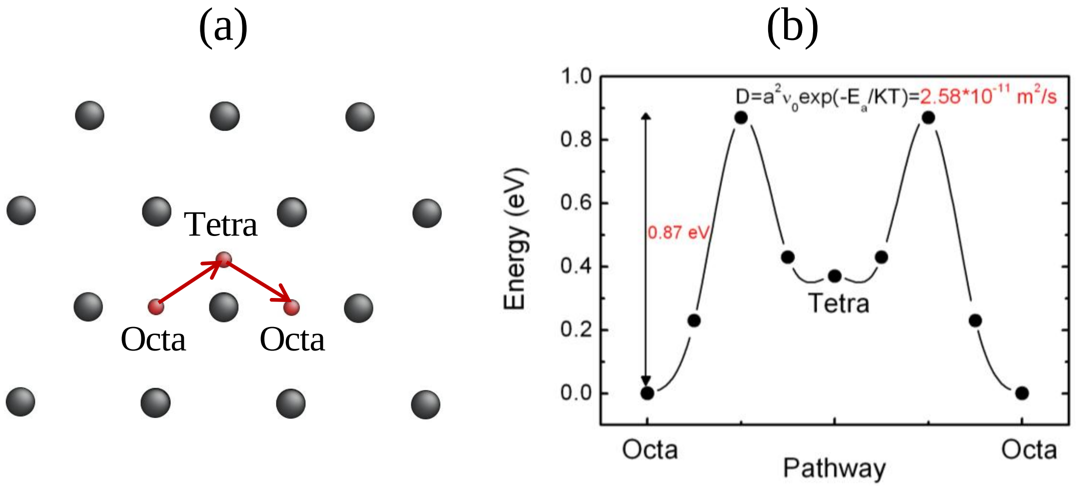

Figure 22: (a) The diffusion trajectory of a single oxygen atom in a c-Ni supercell. The grey solid circles represent the Ni atoms. The arrows represent the diffusion of an oxygen atom along the octahedron-tetrahedron-octahedron pathway. (b) The energy barrier for an oxygen atom in the c-Ni lattice. The activation energy is calculated as 0.87 eV, and the diffusivity of oxygen is estimated as $\mathbf{2.58 \times 10^{-11} m^2/s}$ using the Arrhenius equation.

Figure 22(b) shows the energy profile for oxygen diffusion calculated by the NEB method. The activation energy is 0.87 eV along the octahedron-tetrahedron-octahedron pathway. The diffusion constant can be estimated by the Arrhenius equation $D = a^2 \nu_0 \exp(-E_a/kT)$, where a is the elementary hopping distance, ν_0 is the hoping frequency, E_a is the activation energy barrier, k is the Boltzmann constant, and T is the absolute temperature. Using the lattice constant 3.52 Å, activation energy E_a=0.87 eV, T = 1000 K, and a typical value of $\nu_0 = 10^{13} s^{-1}$, we found the diffusivity of oxygen in c-Ni to be $D = 2.58 \times 10^{-11} m^2/s$.

3.5.2. Oxygen and Nickel diffusivity in amorphous Ni

To compute the diffusivity of oxygen and nickel at the temperature of interest, we performed non-equilibrium finite temperature molecular dynamics simulations within the framework of density functional theory (DFT) as implemented in VASP. Projector-augmented-wave (PAW) potentials were used to mimic the ionic cores, while the generalized gradient approximation (GGA) in the Perdew-Burke-Ernzerh of (PBE) flavor was employed for the exchange and correlation functional. We used the plane-wave cutoff of 400 eV and a *k*-point mesh of $4 \times 1 \times 2$ for all calculations. To quantify the diffusivity of both oxygen and nickel at different oxygen concentrations, we systematically varied the oxygen concentration by placing oxygen at the interstitial sites. For the GB structure with an amorphous nature, we performed Delaunay triangulation to find the interstitial sites with the largest void size to accommodate the insertion of oxygen. This method provided us a fast way to identify the favorable positions of oxygen insertion with low formation energy in the amorphous lattice.

We performed the MD calculations at temperatures 1500, 2000, 1200, 3000, and 4000˚K. Starting from the relaxed initial configurations, we first ran 500 MD time steps to incite sufficient local vibration of atoms at these temperatures, where each MD step was set as 2 fs. Then the cells were allowed to dynamically equilibrate at fixed temperatures for roughly 5000 MD time steps. The total simulation time corresponded to more than 10 ps, which induced substantial mixing of oxygen and nickel atoms with each other. The random walking of both oxygen and nickel were closely examined. It clearly showed that the atomic motions were far beyond the local elementary hopping. We then calculated the mean square displacements (MSD) for oxygen and nickel atoms as a function of time in order to compute diffusivities at different temperatures.

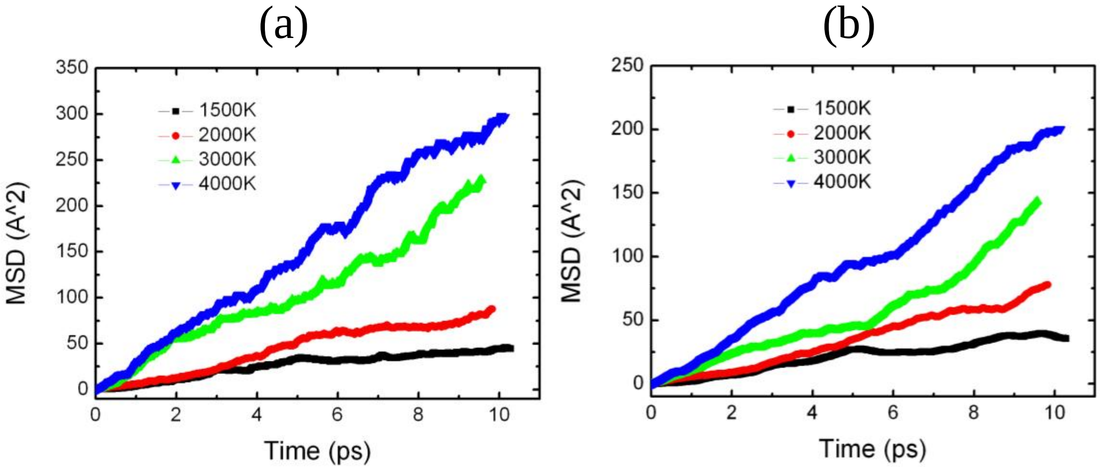

Figure 23: The mean square displacement of (a) oxygen, and (b) nickel as a function of the MD simulation time at various temperatures in a representative amorphous structure $NiO_{0.5}$.

The calculated mean square displacement of both oxygen and nickel in a representative amorphous structure $NiO_{0.5}$ is shown in Figure 23. In statistical mechanics, the mean squared displacement is the most common measure of the spatial extent of random motion. It is defined by the relation:

$$MSD = \langle |r_i(t) - r_i(0)|^2 \rangle \tag{3.1}$$

where $r_i(t)$ is the position of the atom i at the time t, $r_i(0)$ is the position of the atom i in the initial configuration, and <…> represents an average over the ensemble of atoms. We have considered the jumps of particles and refold them into the box when using periodic boundary conditions as contributing to diffusion. The atomic diffusivity can be derived from the MSD. If the system is solid, MSD saturates to a finite value, while if the system is liquid at elevated temperature, MSD grows linearly with time. In this case it is useful to characterize the system behavior in terms of the slope, which is the diffusion coefficient *D*

$$D = \lim_{t\to\infty} \frac{1}{6t} \langle |r_i(t) - r_i(0)|^2 \rangle \tag{3.2}$$

Using the above relation, we calculate diffusivities of oxygen as well as nickel for different temperatures and extrapolate the data to obtain the diffusivities at T=1000 ˚K. The extrapolation is carried out by following the standard expression for diffusivity, $D = D_0 \exp(-E_a/kT)$, where E_a is the energy barrier, k is the Boltzmann constant, and *T* is the absolute temperature. Plots of diffusivity versus 1000/T on a log scale for both oxygen and nickel in the amorphous structure $NiO_{0.5}$ are shown in Figure 24.

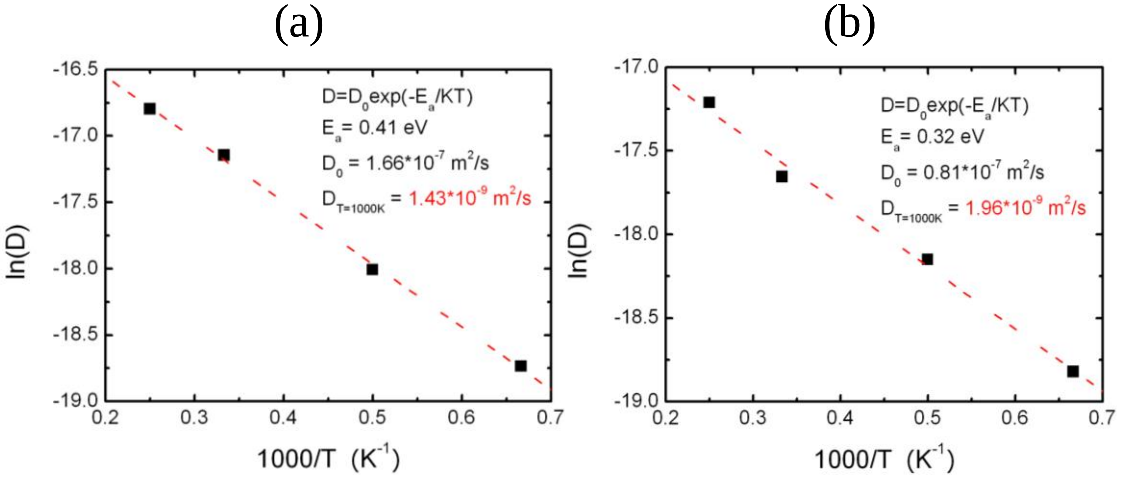

Figure 24: Diffusivity of (a) oxygen, and (b) nickel with respect to the inverse of temperature in the amorphous structure $NiO_{0.5}$. The inset shows the fitting parameters using the standard exponential fitting $D = D_0 \exp(-E_a/kT)$. The value of diffusivity at low temperature T=1000˚K is extrapolated from the high temperature data.

Following the same procedure, we varied the oxygen concentration to quantify the dependence of atomic diffusivity on the composition. The MD simulations have been fairly time-consuming. Depending on the size of the configurations, the computation times were slightly different, but the average time for each composition took around one week. We have completed the calculations for $Ni_{56}O_4$, $Ni_{56}O_{12}$, $Ni_{56}O_{20}$, and $Ni_{56}O_{28}$.

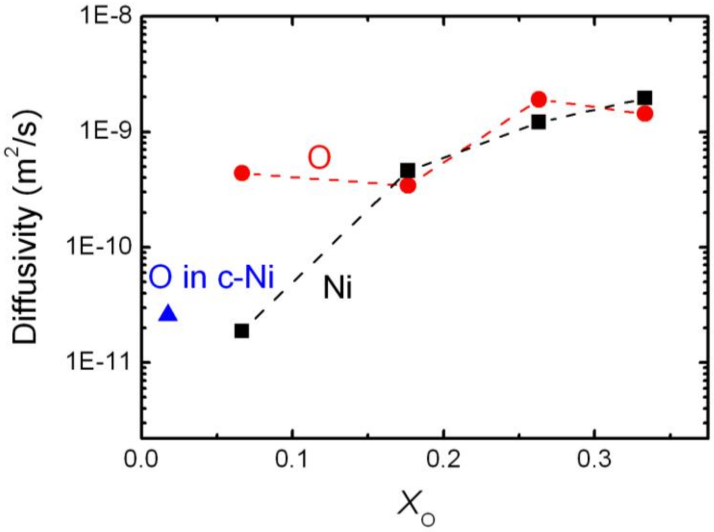

Figure 25: Diffusivity of oxygen (red circles) and nickel (black squares) as a function of the oxygen composition X_O in the amorphous structure, where X_O is defined as $N_O/(N_{Ni}+N_O)$. The dashed lines are guide for the eyes. The diffusivity of oxygen in c-Ni calculated by nudged elastic band method is represented by the blue triangle.

The compositional dependence of diffusivity of oxygen and nickel are summarized in Figure 25. The diffusivity of a single oxygen atom in c-Ni structure calculated by the NEB method is also included for comparison. We can see that the oxygen diffuse faster in the amorphous lattice than that in the crystalline phase by roughly one (1) order of magnitude. Note that we did not perform random walking MD simulations for a single oxygen atom in the amorphous structure because the statistics of a single atom may not be meaningful. In addition, for both oxygen and Nickel, we see that the diffusivity increases along with the oxygen concentration. This may be attributed to the factor that oxygen insertion weakens the structure strength of Ni lattice, which allows for a faster motion of atomic species.

To summarize, we use the nudged elasticity band method to calculate the activation energy of diffusion for a single oxygen atom in c-Ni. The diffusion trajectory is identified as the octahedron-tetrahedron-octahedron pathway. The value of activation energy barrier is 0.87 eV, and diffusivity is estimated to be $D = 2.58 \times 10^{-11}\ \mathrm{m^2/s}$. We further perform the non-equilibrium ab initio molecular dynamics to mimic the random walking of oxygen and nickel at elevated temperatures. We calculate the mean square displacement to plot the statistics of atomic motion, and derive the diffusivity at these temperatures. The diffusivity at low temperature of interest is extrapolated via an exponential fitting. We vary the oxygen concentration in the amorphous model to quantify the diffusivity dependence on the composition. These data can be useful inputs for finite element modeling and phase field simulations.

3.6. Hydrolytic weakening of Chromia

It is known that the effect of surface hydrolytic weakening of oxide is mostly local, which renders first-principles a suitable method to characterize such effects. Here we reproduce the phase diagram of Cr-H-O (Figure 26), to call for attention on the formation of $CrHO_2$ under hydrolysis conditions. The hydrolysis follows the reaction $Cr_2O_3+H_2O \rightarrow 2CrHO_2$. We calculated the driving force of the reaction as -0.45 eV. Such a high driving force can promote formation of the hydrolyzed chromia. In particular at the crack tip where a high magnitude of tensile stress concentrates, the mechanical stress can further bias the reaction barrier, and accelerates the hydrolysis reaction. We also found volume increase $\Delta V = 13.33\text{Å}^3$ from Cr_2O_3 to $CrHO_2$. The volume expansion causes lattice mismatch and may contribute to the fracture of the oxide. The atomic configurations of Cr_2O_3 and $CrHO_2$ are represented in Figure 27. Cr_2O_3 has a space group of R3c, and lattice parameters of a=b=4.96, c=13.59, α=β= 90°, γ=120°. $CrHO_2$ has a space group of P21nm, and lattice parameters of a=4.89, b=4.29, c=2.95, α=β= γ=90°.

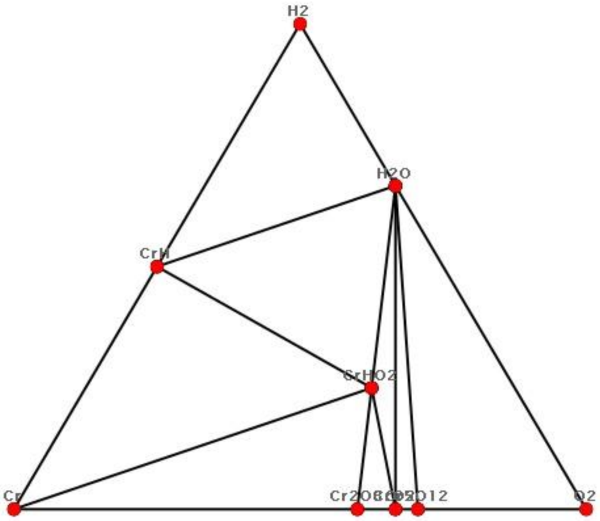

Figure 26: Cr-H-O phase diagram [5].

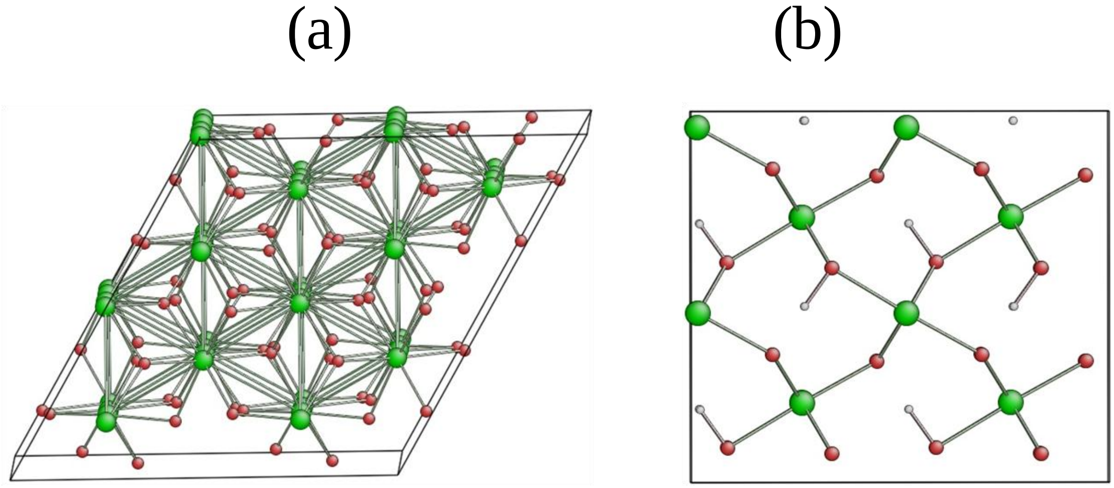

Figure 27: The atomic configurations of (a) Cr_2O_3, and (b) $CrHO_2$. The green spheres are Cr atoms, and the red spheres are oxygen atoms.

As seen from the atomic configurations, the presence of H atoms decreases the coordination number of Cr-O from 6 in Cr_2O_3 to 4 in $CrHO_2$. Such difference can cause dramatic decrease of the fracture strength of the oxide. To quantify such weakening effect, we also performed uniaxial tension simulations, as described in the above section, to compare the fracture strength of Cr_2O_3 and $CrHO_2$.

The stress-strain curves are reproduced in Figure 28(a). The strain is incrementally applied, and the peak stresses represent the respective ideal strength. Indeed, $CrHO_2$ is mechanically weaker than Cr_2O_3 and its fracture strength is about a half of Cr_2O_3. It indicates that upon formation of the hydrolyzed phase, the protective function of oxide can be significantly weakened. The atomic configuration of $CrHO_2$ is shown in Figure 28(b), it is evident that the hydrolyzed Ni-O is weaker than the pristine Ni-O bonds, and fracture occurs around the local hydrolyzed Ni-O bonding.

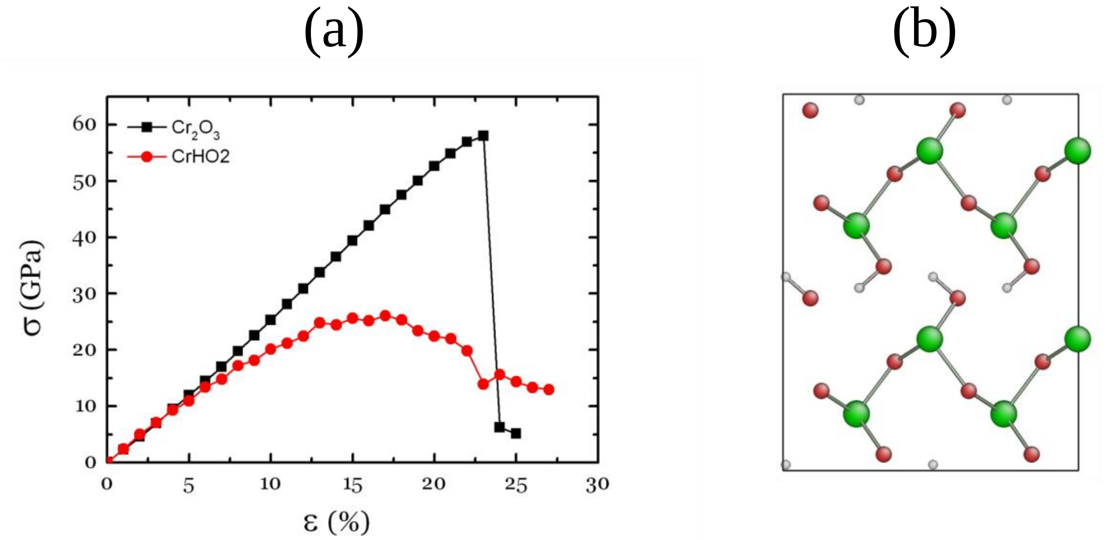

Figure 28: (a) Stress-strain response of Cr_2O_3 and $CrHO_2$. The peak stresses represent the respective ideal strength. (b) Atomic configuration of $CrHO_2$ after fracture.

3.7. Summary

We proposed a scenario that the leading effect of oxygen embrittlement was due to the presence of oxygen monolayers in the grain boundaries of a Ni-based superalloy. Through energetic studies, we confirmed that oxygen transported more favorably along the metal grain. Such absorption may initiate the oxide monolayer within the grain boundaries and embrittle its cohesion strength. We quantified the embrittlement effect by performing uniaxial tensile simulations. As oxygen concentration increases, the ideal fracture strength of a-NiO_x decreases dramatically, such that a fraction of oxygen monolayer in the metal grain boundaries could severely influence the GB cohesion characteristics. We also studied the diffusion of oxygen in the nickel lattice, and performed first-principles modeling to calculate the oxygen diffusivity in both the crystalline and amorphous Ni phases. In addition, we proposed the hydrolytic weakening effect of chromia. We found a high driving force for the hydrolysis reaction to occur, especially at the crack tip. Upon formation of hydrolyzed phase $CrHO_2$, the protective layer of oxide was mechanically severely weakened.

Task 4: Modeling of gamma prime microstructures and mesoscale microstructure-defect interactions

This task is to apply thermodynamic and kinetic modeling to microstructure evolution and microstructure-level defects interaction in Alloy 282. In particular, by emphasizing microstructure-property relationship, quantitative modeling of gamma prime (γ’) microstructures in Alloy 282 enables reliable predictions for long-term creep performance (see Task 5) in A-USC steam turbine operation. Modeling of cracks in polycrystal microstructures and under oxygen effect allows us to gain mechanism understandings of the complex interactions between crack growth behaviors and microstructural and environmental effects, and provides a potential linkage between the experimental (Task 2) and atomistic modeling (Task 3) studies and the constitutive fatigue crack growth modeling (Task 6).

4.1. Gamma prime microstructure modeling for Alloy 282

Alloy 282 is a γ’-strengthened Ni-base alloy[6], with about 20% volume fraction of coherent γ' phase precipitates (ordered $L1_2$ structure) dispersed in disordered face-centered cubic γ phase matrix at 1400˚F. Thermodynamic calculations predict the γ’ solvus temperature at about 1840˚F (Figure 29). Typical two-step aging heat treatment[6] produces fine γ’ precipitates via homogeneous nucleation and growth. Depending on aging conditions, γ’ size ranges typically in several tens of nanometers (Figure 30). The γ’ precipitates continue to coarsen during long-time high temperature exposure.

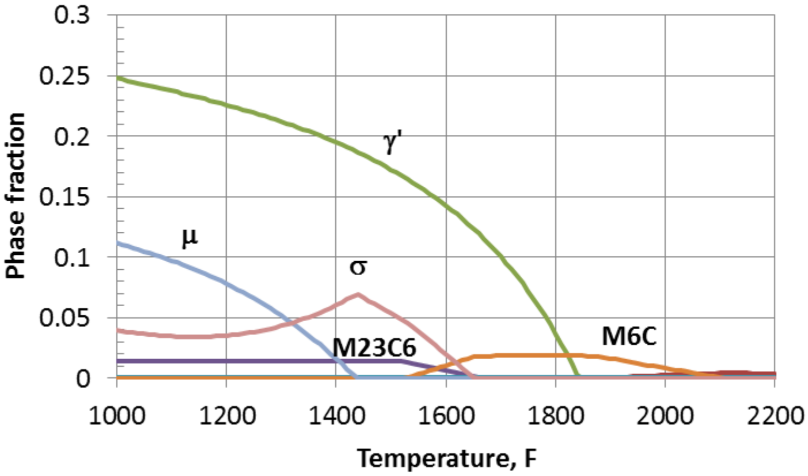

Figure 29: ThermoCalc prediction of phases in Alloy 282, with TTNI7 database[7].

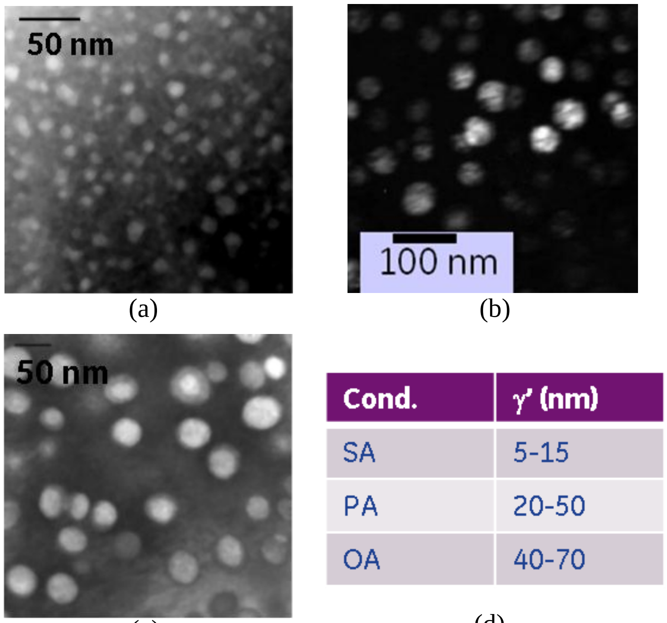

(a) (b)

Cond.	γ' (nm)
SA	5-15
PA	20-50
OA	40-70

(c) (d)

Figure 30: Alloy 282 γ' size after different heat treatment: (a) solution annealed (SA), (b) peak-aging (PA), and (c) over-aging (OA). Courtesy of Jeffrey Hawk

4.1.1. Gamma prime microstructure models

To quantitatively model γ' microstructures in sufficient details (precipitate size, volume fraction, spatial distribution) and under long-duration conditions (20 years), two GE internally developed γ' microstructure models were jointly applied to Alloy 282. The precipitation (PPT) model, based on the Langer-Schwartz type models[8-11], treats concurrent nucleation, growth, and coarsening of γ' in a continuous particle-size-distribution space. The precipitates' morphological details are not taken into account. The effects from γ' spatial distributions are simplified with a mean-field approximation, in which the precipitates are considered to share a common γ phase matrix that is spatially uniform. The γ matrix possesses the averaged composition of γ phase, which varies during different stages of precipitation and is subject to mass conservation constraint. The second model, based on the phase field (PF) method, provides the 3D spatial details of γ' microstructure, as well as the spatial distribution of chemical composition. The in-house phase field microstructure model was developed in a parallel code for multi-core systems, which allows a sufficient length and time scale for simulating the actual cooling and aging heat treatment conditions. In the present work, we have applied the PF model to predict microstructures under lab heat treatment conditions, over several thousand hours, and the PPT model to the longer-term creep conditions, over tens of years.

The PPT and PF models share the same physical laws of nucleation, growth, and coarsening of γ', but at different levels of details. In general, construction of the PF model is more sophisticated since it involves solving spatial evolution of solute diffusion and interface movement and, as a result, is computationally more costly. Nucleation in the phase field model is handled by the explicit nucleation algorithm[12], and the framework of Kim et al[13] is adopted to treat the thermodynamics of γ/γ' interface. An immediate benefit from sharing a common physical framework between the two models, however, is that a same set of physical parameters can be applied and that the outputs from the two models are mutually comparable. To provide alloy specific input to the PPT and PF models, thermodynamic and diffusivity data (for γ, γ' phases) were derived from CALPHAD database [7,14]. These parameters were reduced to a pseudo-binary composition description from the actual multi-element composition of Alloy 282 (see Table 1). γ/γ' interface energy was calibrated to a separate set of experimental data. Both models were designed to handle complex heat treatment conditions, including isothermal aging at different temperatures as well as non-isothermal conditions. Therefore, time-temperature data were used directly as model input.

Table 1: Alloy 282 chemical composition, weight percent [6]

Ni	Cr	Co	Mo	Ti	Al	Fe	Mn	Si	C	B
57**	20	10	8.5	2.1	1.5	1.5*	0.3*	0.15*	0.06	0.005

* Maximum, ** Nickel as balance

4.1.2. Calibration of precipitation model

Only a few parameters in the PPT model require calibration. These are a set of proportionality factors for correcting the default values for the γ/γ' interface energy, diffusion coefficient, and nuclei size. These parameters are difficult to measure directly by experiment, therefore are left to calibration.

In the calibration, the PPT model was applied to simulate a set of linear cooling conditions in a range of cooling rate between 0.15˚F/min to 5000˚F/min. All the simulations were started from above the γ' solvus temperature. During cooling, γ' precipitates formed at various temperatures depending on the cooling rate. The temperatures at which 2% of γ' volume fraction was reached were designated as the starting temperatures of γ' transformation, T_s. These values were compared with the experimental measurement of γ' precipitation temperatures using single-sensor differential thermal analysis (SS DTA). We used the SS DTA data on Alloy 282 developed in a prior internal program at GE-GRC. The aforementioned calibration parameters were iterated until T_s from PPT model matched the SS DTA data. The iterations were performed with a GE internal optimization tool, PEZ. Global minimization based on genetic algorithm was used to improve search of the true optimal parameters instead of locally entrapped solutions in the multi-dimensional parameter space. Figure 31 shows the results after the calibration.

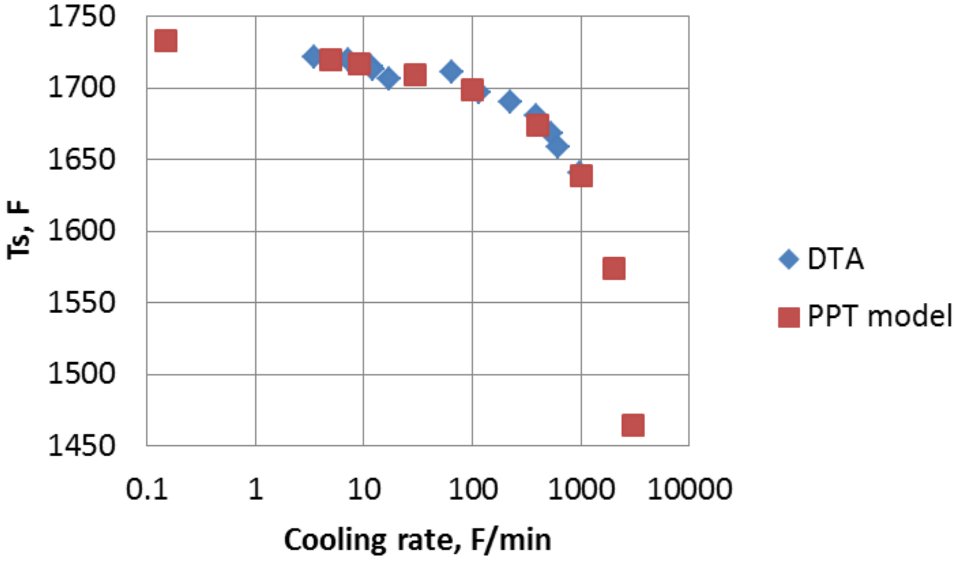

Figure 31: Calibration of PPT model to γ’ transformation temperatures at various cooling rates from SS DTA data.

4.1.3. Model validation

A set of twelve heat treated Alloy 282 specimens from a prior program were selected for validating the calibrated PPT model. These specimens, listed in Table 2, were fully γ’ solutionized at 1900˚F, cooled at 9˚F/min to four different temperatures between 1650˚F and 1300˚F, and isothermally aged. Figure 32 shows a typical uni-modal γ’ microstructure in the specimens. γ’ sizes were characterized for each specimen and were used for model validation.

Table 2: Heat treated specimens selected for γ' size characterization for validating PPT model. All specimens were solution heat treated, cooled at 9˚F/min to designated temperatures, and followed by isothermal aging given in the table.

Temperature (˚F)	Aging time (hours)			
1650	0	166	1007	3006
1500	0	985	3026	5015
1400		985	3000	5133
1300				8186

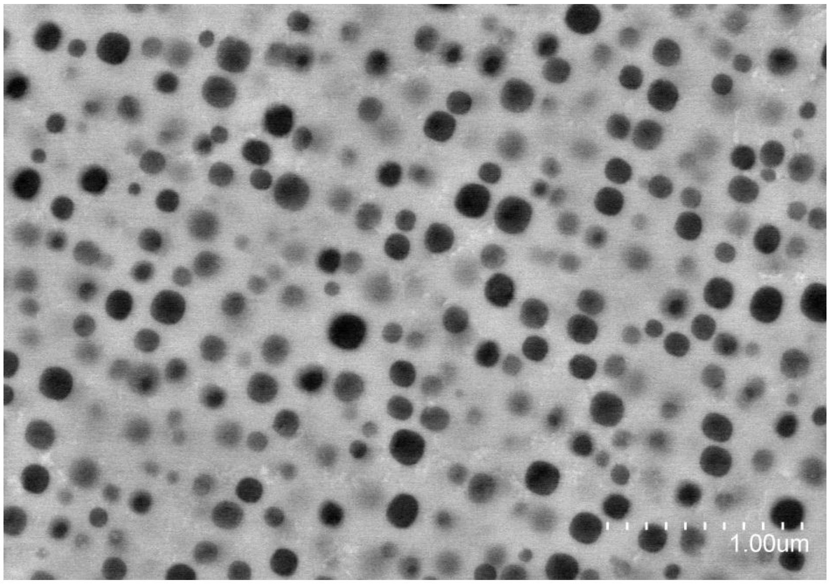

Figure 32: SEM image of γ' microstructure in Alloy 282 after 5133 hours aging at 1400˚F

The PPT model simulated continuous evolution of γ' size under these heat treatment experiment conditions. An additional temperature at 1600˚F was also included. As compared in Figure 33, the predicted γ' sizes are in very good agreement with the experimental data, especially if one considers that the PPT model was calibrated only to the very beginning of γ' precipitation (i.e., nucleation) and that it was able to predict correctly the microstructure changes almost ten thousand hours later.

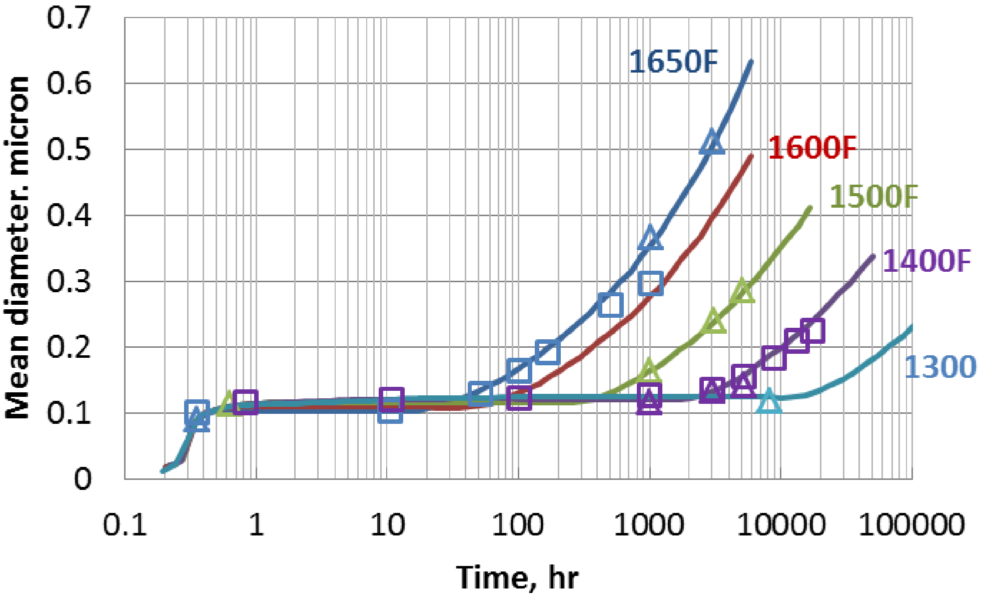

Figure 33: Predicted γ' sizes by the PPT model (curves) and by the PF model (squares) vs. experimental data (triangles) measured from specimens in Table 2. Some additional short-term historical data (<2hrs) are also plotted for comparison.

The experimental and predicted γ' size evolution in Figure 33 shows clearly that the conventional cubic coarsening law does not follow immediately the nucleation and growth stage of γ'. This transitional 'gap', appeared in Figure 33 as a plateau of nearly constant γ' mean size, extends as temperature decreases. A more detailed examination at 1400˚F indicates that the γ' size distribution in fact continuously broadens (Figure 34), even though the average γ' size only slightly changed. Obviously, as one attempts to use a cubic law to interpret γ' coarsening data in hands that happen to fall (or partially fall) in this plateau regime, the γ' size change will be eventually under-predicted. This under-prediction can become significantly greater if one attempts to extrapolate for long-term γ' coarsening behaviors.

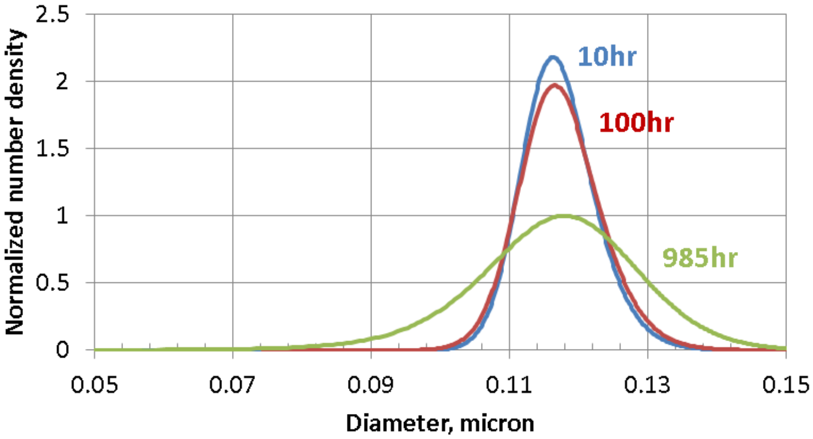

Figure 34: Broadening of γ' size distribution at 1400˚F for 10hrs, 100hrs, and 985hrs, predicted by the PPT model.

A series of phase field simulations were performed for the heat treatment conditions at 1400˚F and 1650˚F listed in Table 2. A snapshot of γ' microstructure after 100 hours of aging at 1400˚F is shown in Figure 35. The simulation volume is $2 \times 2 \times 2\mu m^3$. The simulated microstructures were found remarkably close to what was actually observed in Alloy 282 under the same heat treatment conditions. Figure 36 shows three scanning electron microscopy (SEM) images of specimens interrupted at 985, 3000, and 5133 hours during the 1400˚F aging. The inset in each of the images is a section view of the simulated 3D microstructure at the same interruption time. Both SEM and simulated images are displayed at the same length scale for comparison. The particle size, shape, inter-particle spacing in the simulated images are seen very close to the SEM images.

To validate the quantitative features of the simulated microstructures, we compared the mean γ' sizes predicted by the phase field model at two aging temperatures, 1400˚F and 1650˚F. Simulating the two temperatures required no change to the model or parameters except for the input time-temperature condition. Figure 33 shows the agreement between the phase field predictions and the γ' size measured from the specimens under the same heat treatment, together with the PPT model predictions. A more detailed comparison in terms of particle size distribution also indicates close agreement between phase field predictions and the actual microstructure (Figure 37). Note the precipitation model predicts typically a narrower particle size distribution at early stages due to lack of description of solute diffusion profiles (soft-impingement) in mean-field type models.

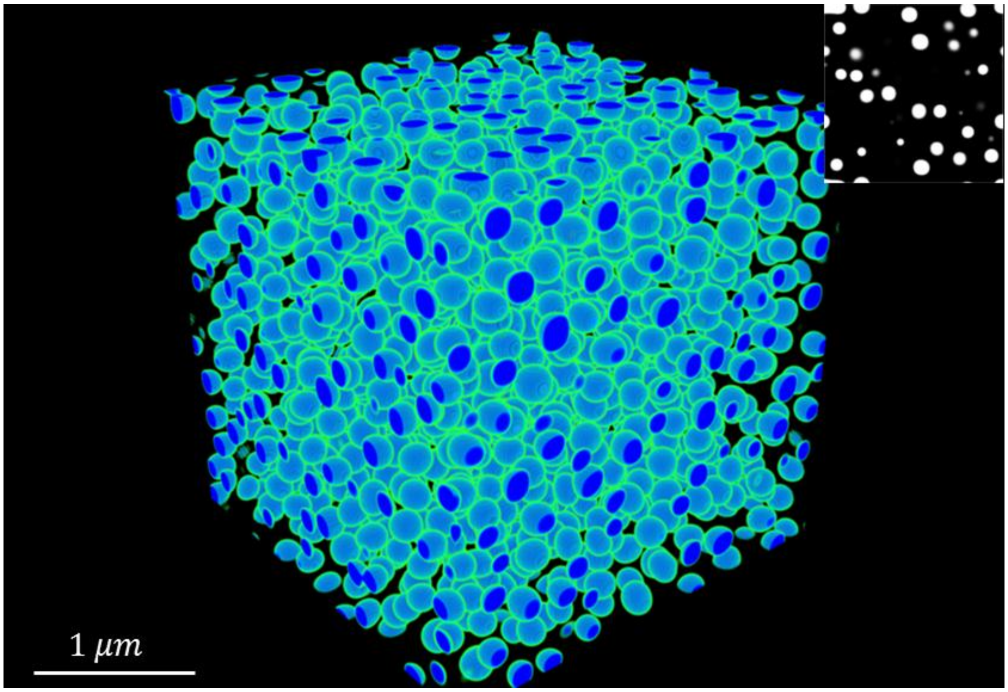

Figure 35: Simulated γ' microstructure after 100hr aging heat treatment at 1400˚F following a 9˚F/min cooling from solution temperature. Particles are γ' precipitates. The inset shows a cross section view.

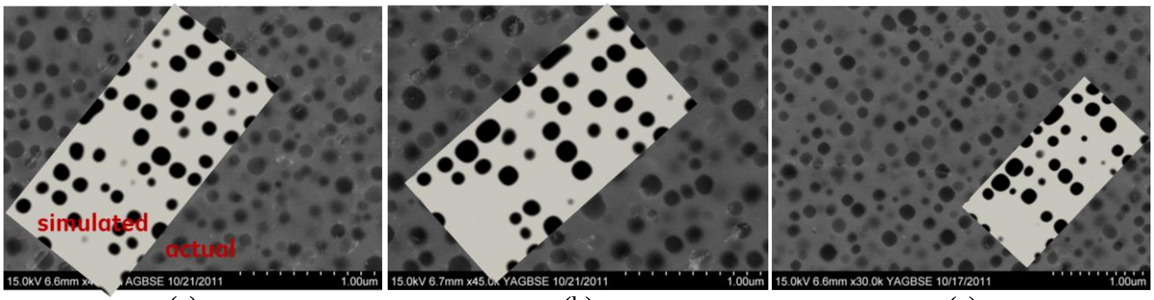

(a) (b) (c)

Figure 36: Comparison with actual microstructures after the 1400˚F heat treatment: (a) 985hrs, (b) 3000hrs, and (c) 5133hrs. Length scale of each image pair is kept identical for comparison.

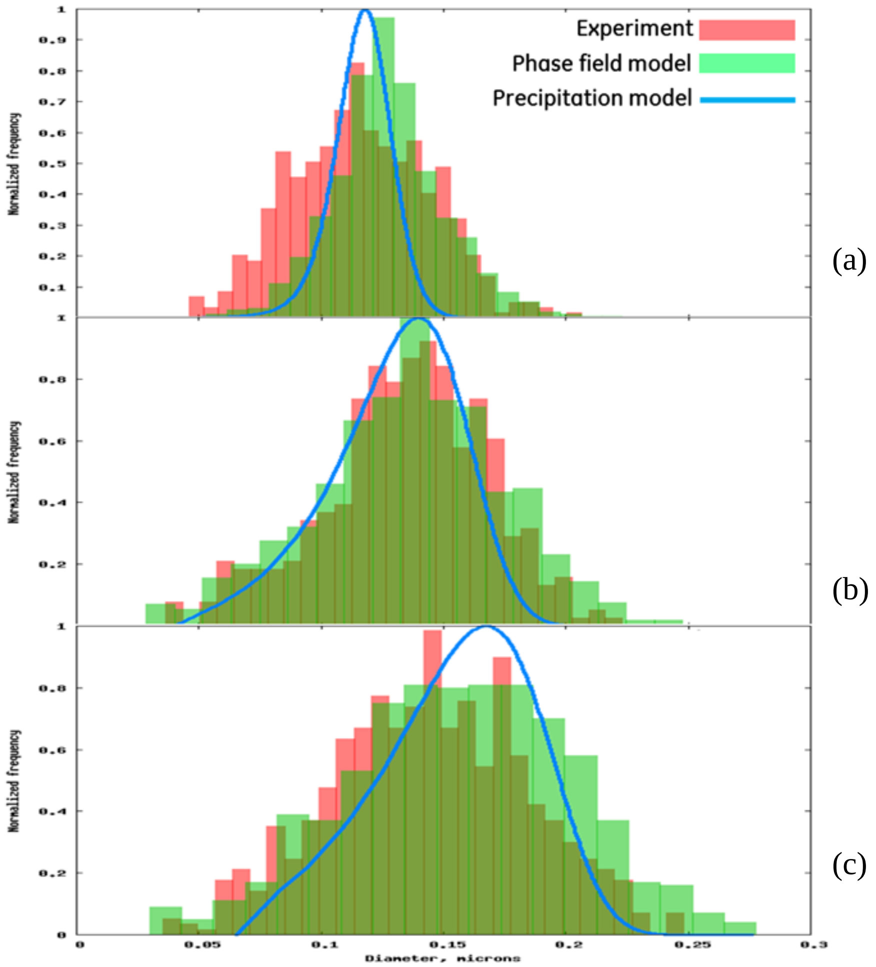

Figure 37: Comparison of γ' size distribution during 1400˚F aging, at (a) 985hrs, (b) 3000hrs, and (c) 5133hrs. Also shown is the prediction from precipitation model (curves).

To examine how well the phase field model can predict γ' morphology, we considered two heat treatment conditions with very different cooling rate, listed in Table 3. As is seen in Figure 38(b) and (d), at the much slower cooling rate 9˚F/hour, γ' precipitates grew considerably larger and into irregular dendritic shapes, while at 9˚F/min cooling rate they were formed mostly as fine spherical particles. These conditions can be taken as good test cases for the phase field model. The simulation results in Figure 38(a) and (c) demonstrate that the Alloy 282 phase field model can reproduce fairly well the morphological difference in γ' precipitates at the two vastly different cooling rates.

Table 3: Heat treatment condition of two Alloy 282 specimens

Heat treatment 1	Solution (1900˚F) + 9˚F/hour cooling + 1600˚F/100 hours aging
Heat treatment 2	Solution (1900˚F) + 9˚F/min cooling + 1600˚F/100 hours aging

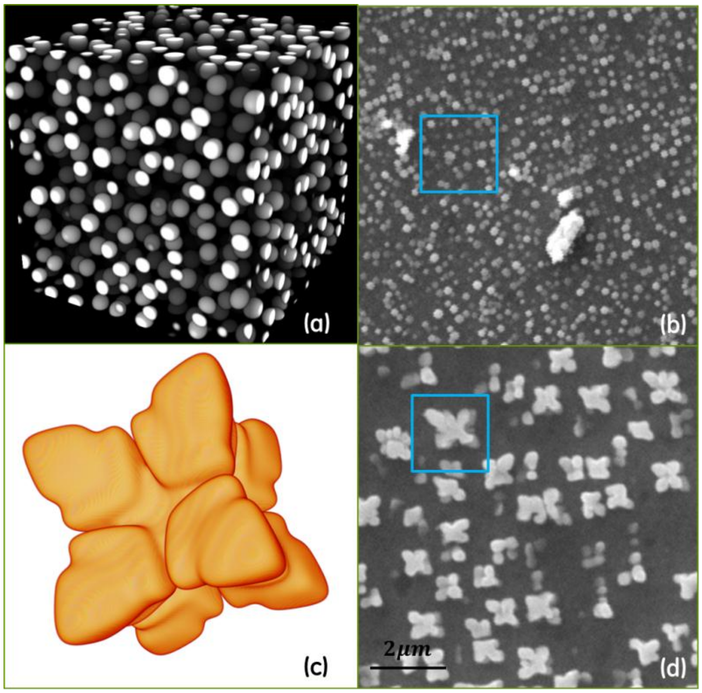

Figure 38: Phase field simulation of γ' microstructure in Alloy 282 under two different heat treatments: fast 9˚F/min cooling (a) simulation, (b) actual image; slow 9˚F/hr cooling (c) simulation, (d) actual image. The boxes on (b) and (d) represent the simulation cell ($2 \times 2 \times 2\boldsymbol{\mu m^3}$) on the left respectively.

4.1.4. Predictions of long-term microstructure change

Beyond the aforementioned transition regime on precipitate size evolution, longer-term γ' coarsening evolution can be well described by the cubic law,

$$D^3(t) - D_0^3(t_0) = K(T)(t - t_0) \tag{4.1}$$

where D and D_0 are respectively the γ' diameter at time t and t_0. The rate constant, K, is a function of absolute temperature, T. Using the predicted long-term γ' size data, we can fit coarsening rate constant, K, in the cubic regime for each temperature, illustrated in Figure 39.

The temperature-dependent rate constant can then be fitted to the Arrhenius form (Figure 40):

$$K = K_0 \exp(-Q/R_g T) \tag{4.2}$$

The activation energy and pre-exponential factor are found for Alloy 282 as: $Q = 287.2kJ/mol$, $K_0 = 7.15 \times 10^{-14} m^3/sec$.

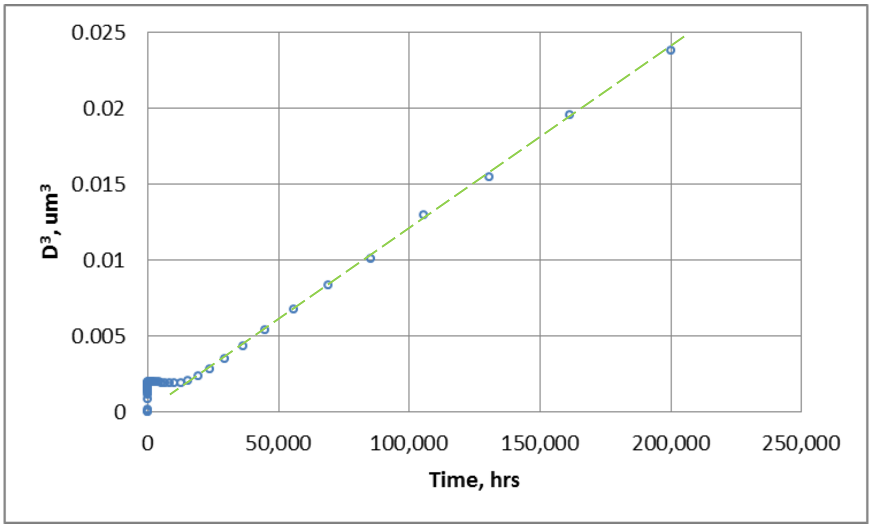

Figure 39: Simulated long-term γ' mean size at 1300˚F by the PPT model. The dashed line represents a cubic law regime of coarsening.

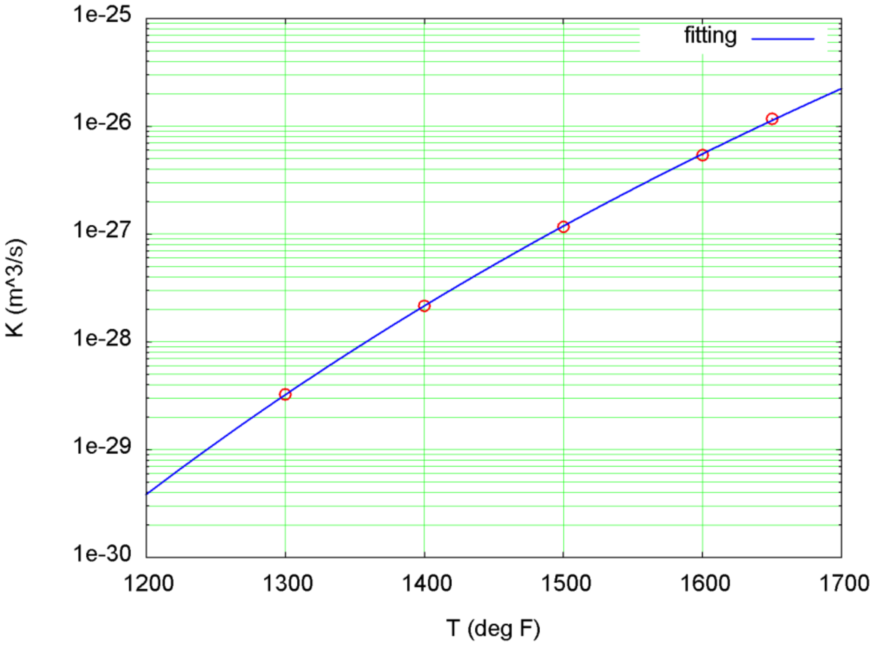

Figure 40: Predicted coarsening rate constant at each temperature (circles) and the fitted Arrhenius equation (curve).

4.2. Link microstructure to creep model

From an energetic point of view, the stress level for A-USC steam turbine rotor application, 15ksi (103MPa), is lower than the threshold stress for a dislocation to directly shear γ’ precipitates. Table 4 compares the estimated stresses for creating several common planar faults in γ’ by a single dislocation with appropriate Burgers vector associated with the fault. Although these values are only indicative, they identify correctly the stress regimes for γ’ shearing. The observations of predominant dislocation looping and climbing, instead of shearing, γ’ in Alloy 282 creep test samples in the 15-20ksi stress range (see Section Task 5) further confirm this estimation.

Table 4: Estimated stress level for creating different γ' faults (based on single dislocation shearing).

Deformation type	Typical fault energy (J/m^2)	Burgers vector (Å)	Threshold stress (ksi)
Anti-Phase Boundary (111)	0.16~0.22	2.54	91~126
Complex Stacking Fault	0.2~0.4	1.47	198~396
Superlattice Extrinsic Stacking Fault	0.01~0.02	2.93	5~10

When dislocation climb-bypass is the controlling deformation mode, the γ’ volume fraction and inter-particle spacing become the set of key microstructural parameters to creep. Although counting average γ’ size and volume fraction are usually straightforward, inter-particle spacing appears to be more complicated since it depends on both particle size distribution and spatial distribution. Historically, counting inter-particle spacing has been made with some simplistic assumptions in order to obtain an analytical functional form with respect to particle size. For example, in the square-lattice model[15], such a form is derived by assuming that all the particles have identical size r_p and are arranged regularly in a square array. With these assumptions the inter-particle spacing, λ_p, can be found linearly related to the particle size:

$$\lambda_p = 1.6 r_p (\sqrt{\pi/4\phi} - 1) \tag{4.3}$$

which has been used in the recent creep model by Dyson[16].

The actual γ’ microstructures in Alloy 282 typically have a range of particle size variation and somewhat random spatial arrangement. Secondly, the same average γ’ size or average inter-particle spacing can be associated with different distributions of each. With the now simulated 3D microstructures we can directly extract cross sections along dislocation slip plane, then test and derive more reliably the microstructural parameter relationship.

4.2.1. Average inter-particle spacing in realistic γ’ microstructures

To test the first point, we used Delaunay triangulation[17,18] to construct inter-particle spacing for given γ’ microstructures. Among different triangulation schemes, the Delaunay method tends to maximize the minimal angles of all the triangles in the mesh, so that gives a fair assessment of neighboring particle relations in the microstructure (Figure 41). The analysis can provide both center-to-center distance and inter-particle channel width after subtracting the portion of line segment inside particles, depending on the needs for studying either particle shearing or Orowan looping mechanism.

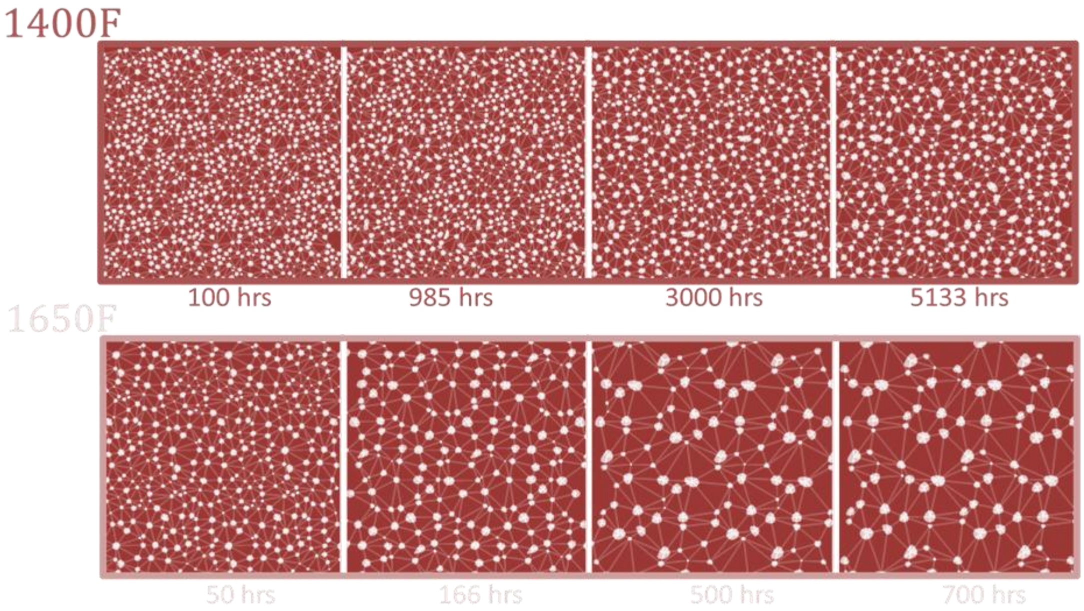

Figure 41: Lines identify inter-particle distance through Delaunay triangulation for two sets of microstructures from phase field simulation.

The Delaunay triangulation analysis performed on two sets of simulated microstructures at 1400˚F and 1650˚F (Figure 41) is converted to a frequency plot (i.e., a histogram) with respect to inter-particle spacing in Figure 42. It is found that a truncated Gaussian distribution function can be used to fit reasonably well the channel width distribution data. The peak of the distribution however is found generally smaller than the mean because of the truncation. Moreover, both the mean and width of the distributions are seen to increase with aging time.

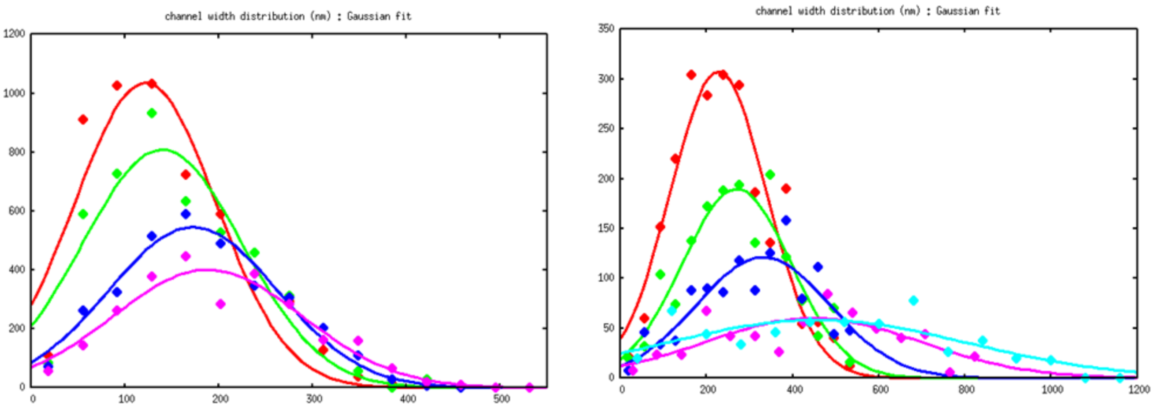

(a) (b)

Figure 42: Inter-particle channel width distribution evolution with aging time at (a) 1400˚F and (b) 1650˚F.

As the γ' microstructures being examined here are all selected from a coarsening stage where the precipitate volume fraction ϕ remains nearly constant, Equation (4.3) simply reduces to a linear relation between inter-particle spacing λ_p and mean particle size r_p. Figure 43(a) shows that such a relation is also followed in the more realistic γ' microstructures where the particles are not distributed in an idealized square array nor are their sizes kept identical. A close look (Figure 43(b)) however suggests that the slopes of the trend from the current analysis are higher than that from Equation (4.3), by a factor of 1.2~1.5. This is not surprising as the Delaunay triangulation constructs inter-particle spacing along not only the 'edges' but also the diagonal directions. This consequently imposes a factor somewhere between 1 and $\sqrt{2}$ in the case of a square lattice.

Additional analyses were performed using computer generated microstructures with:

1. Particles with non-uniform (in Gaussian distribution) size on a square lattice
2. Uniform particle size but in a random spatial distribution

All these test results confirmed the linear trend in Figure 43(a). Nevertheless this relation might not universally reflect the interaction between precipitates and dislocations. For example, depending on stress level, dislocation looping might not practically 'see' those wide inter-particle channels, and likewise dislocation climb/glide might not 'see' the very narrow channels. Such bias effects are likely to become more pronounced as wide channels are prevailing in a microstructure and when the stress is low. Further examination is given in the next section.

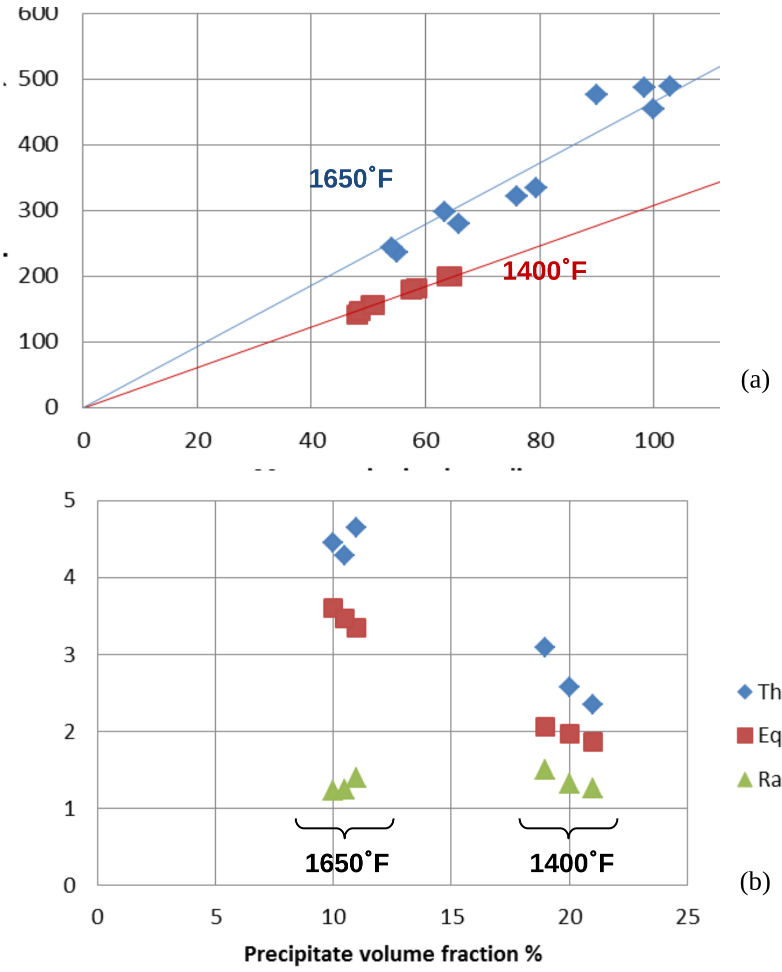

Figure 43: Relationship between mean particle size and mean inter-particle spacing in more realistic microstructures than square lattice, 8 cases at 1400˚F and 10 cases at 1650˚F: (a) a similar linear relation, (b) comparison of the slopes in (a) with Equation (1). Note a stereological multiplication factor $\sqrt{1.5}$ is applied to convert equivalent circular radius to spherical radius r_p in Equation (4.3).

4.2.2. Effective inter-particle spacing in realistic γ' microstructures

One issue with counting inter-particle spacing as an averaged quantity originates from the consideration of the physical role of the inter-particle spacing: it provides a threshold stress to dislocation motion. A dislocation is not required to overcome all inter-particle spacing as long as it can successfully find a series of wide spacing to pass through. In other words the dislocation does not need to sample the entire inter-particle spacing distribution. This difference can become more significant under low stresses, as dislocation movement through precipitates can become more percolative rather than homogeneous. In this context, the average of the entire inter-particle spacing distribution may not necessarily be the best measure of the actual contribution of microstructure to creep.

Moreover, a typical precipitate microstructure such as shown in Figure 44 has a non-symmetric distribution of inter-particle spacing, and the value at the highest frequency does not coincide with the average. Thus one may also ask: between the average and the most frequent inter-particle spacing, which is more sensible to mechanical (creep) properties?

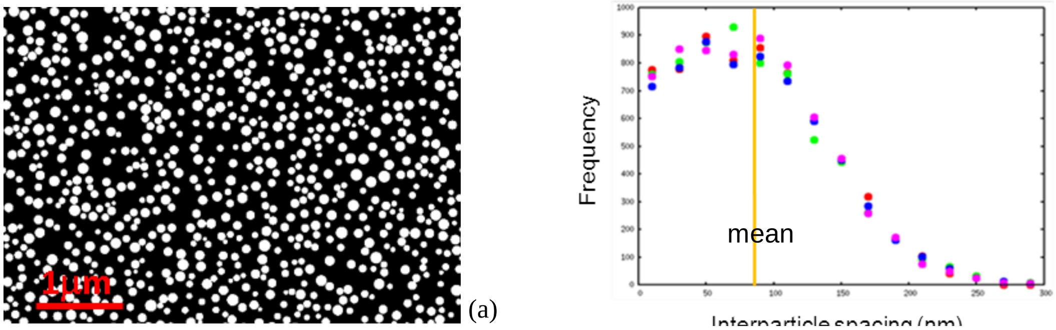

(a) (b)

Figure 44: (a) An artificial microstructure of circular particles with both random spatial distribution and random size distribution. (b) The corresponding inter-particle spacing and the mean (solid line).

We thus developed an approach to derive an effective inter-particle spacing of a realistic (non-uniform) microstructure in three steps:

1. Simulate percolation of a dislocation through the non-uniform microstructure and find an effective threshold stress
2. Simulate the same process but on a regular array of particles, and establish a reference curve of the threshold stress versus inter-particle spacing on the regular array
3. Correlate the non-uniform microstructure in step 1 to the inter-particle spacing in step 2 by equating the two threshold stresses

Figure 45 illustrates Step 1: a dislocation is initially placed at the right side and moves to the left under an applied stress. The area passed by the dislocation is highlighted in red (Figure 45(c-d)). Depending on the inter-particle spacing that the dislocation encounters, the applied stress is initially increased in order to keep the dislocation moving. A threshold stress is reached when the sheared area shows a rapid jump with a very small increase in the stress.

Figure 46 shows Step 2, in which a microstructure is formed by a regular (hexagonal or square) array of precipitates. The inter-particle spacing is readily known in both configurations. A same procedure is followed to find the threshold stress for the dislocation to percolate through the microstructure. Furthermore, inter-particle spacing is varied by keeping particle size constant while increasing the particle density (and thus volume fraction). A linear relation is found between the threshold stress and the reciprocal of inter-particle spacing (Figure 46(b)).

Figure 47 compares the inter-particle spacing of a given non-uniform microstructure such as Figure 44(a) by different counting methods, including

1. the averaged value from the actual distribution of inter-particle spacing (Figure 44(b))
2. the value at the maximum frequency of the same distribution
3. the value derived by Step 1-3
4. approximate the non-uniform microstructure by a hexagonal array of particle of same mean size and volume fraction
5. same as (4) but in a square array

Note the particle size and volume fraction are same in (4) and (5) but the inter-particle spacing is different because of the spatial arrangement. The comparison suggests that the effective inter-particle spacing (from (3)) can be best correlated to a hexagonal array (from (5)). Additionally, the square-array based counting yields a similar value to that at the maximum frequency on the actual distribution curve. Lastly, counting the average of the distribution would likely over-estimate the effective inter-particle spacing.

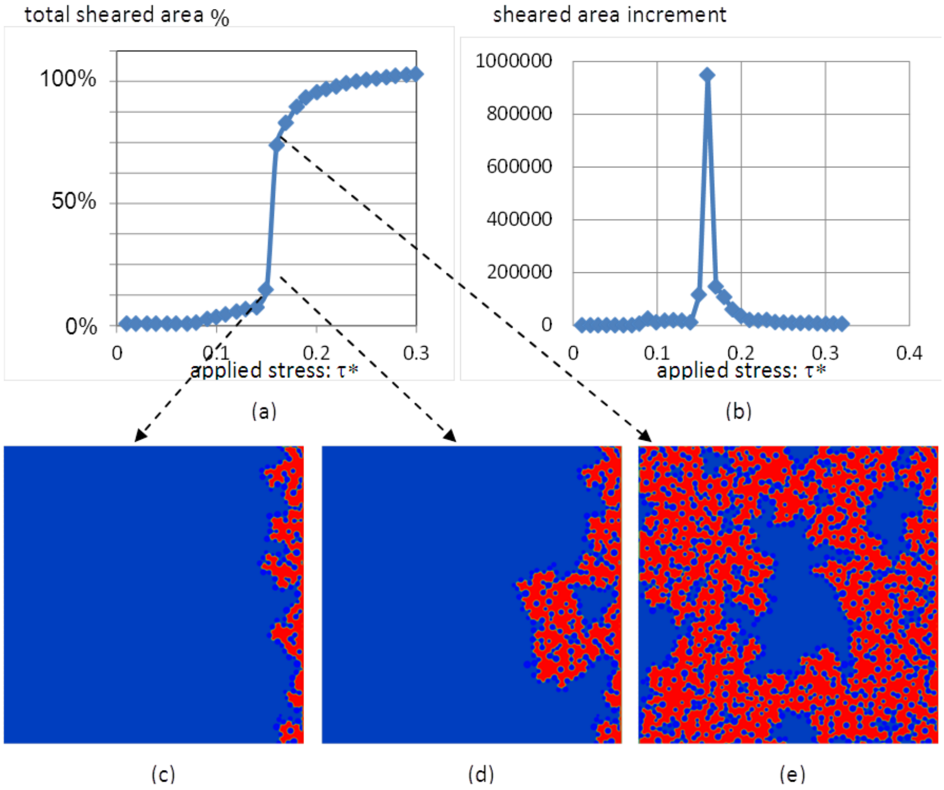

Figure 45: Simulation of dislocation percolation through a precipitate microstructure. (a) minimum stress required to drive dislocation forward (representated by the increase in total sheared area). A rapid jump indicates a threshold stress, shown also as a peak in (b) where differentiation is taken. (c-d) snapshots near the threshold stress (red area designates the area being passed by the dislocation).

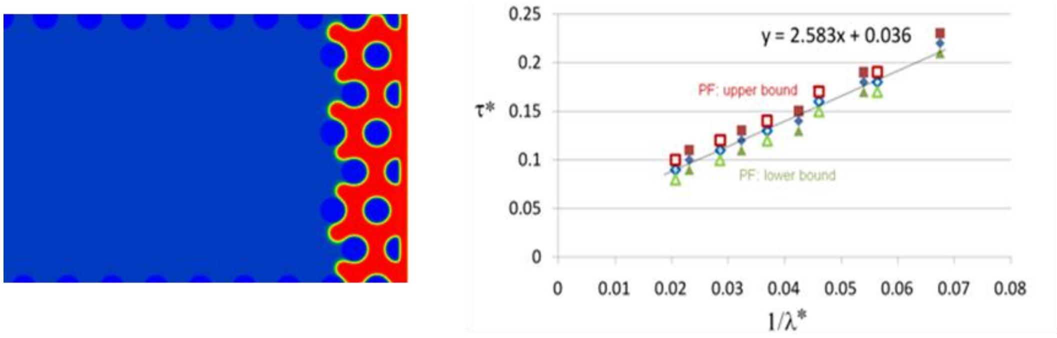

(a) (b)

Figure 46: Simulation of dislocation percolation through a regular array of precipitates. (a) An instance of hexagonal array of particles. (b) The critical stress versus reciprocal of inter-particle spacing λ^* for the hexagonal array (closed symbols) and the square array (open symbols).

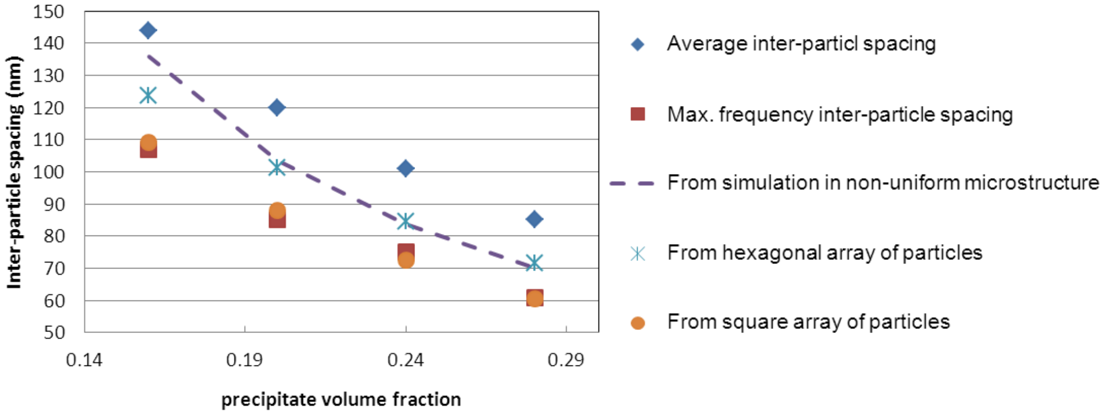

Figure 47: Comparison of inter-particle spacing from different counting methods on a given non-uniform microstructure.

4.3. Thermodynamic calculation of oxides in Alloy 282

Thermodynamic modeling was utilized to interpret the observed oxide formation behaviors at free surface and crack tip (see Section 2.1). ThermoCalc version S[19] was used for the calculations. The equilibrium phase formation at various oxygen level (pO_2) is compared in Figure 48. The variation of pO_2 may be correlated to either the change in the environment (in particular, air vs. steam) or the depth of the location, from the alloy surface or crack tip, to the interior (base) of the alloy.

Starting from the alloy interior (the lowest pO_2) where the phases are predicted mainly as γ and γ' with minor amount of σ phase, Al_2O_3 and TiO_2 oxides are the first to form at very low pO_2 in $10^{-40}\sim10^{-30}\mathrm{atm}$. This is accompanied by decrease in γ' phase as the loss of Al and Ti to oxides destabilizes γ'. As pO_2 increases, Cr_2O_3 becomes dominant at up to $10^{-16}\mathrm{atm}$, and then a mixture of Cr-rich spinel ($NiCr_2O_4$), Co-rich spinel (Co_3O_4), and NiO starts to be the major oxide up to the atmospheric pressure. The latter two regimes seem to correlate well to the specimens tested in steam and air respectively, since the lower pO_2 in steam suppresses NiO that forms in the air environment. It can be further verified that the predicted pO_2 levels for NiO, Cr_2O_3, and Al_2O_3 formation in Figure 48 are consistent with the Ellingham diagram (Figure 5).

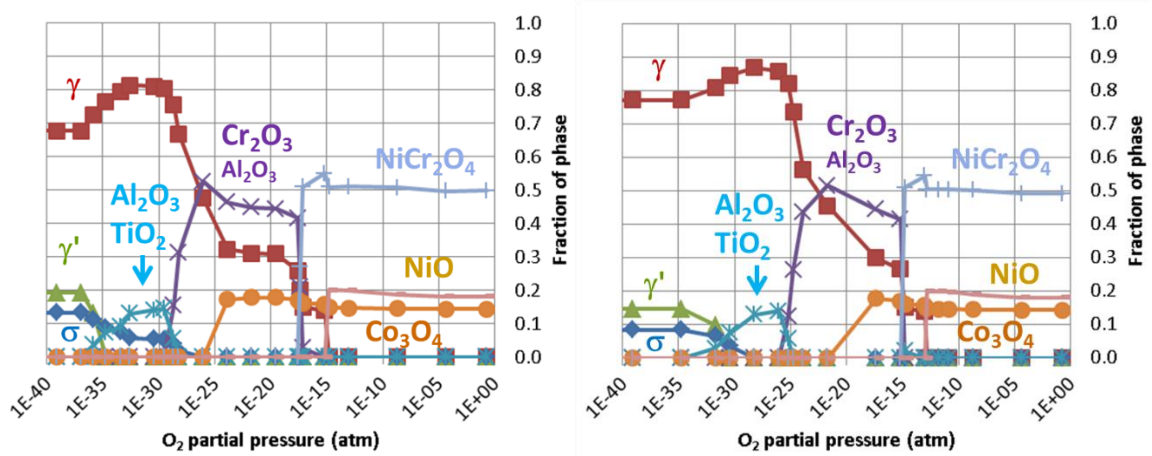

(a) (b)

Figure 48: Thermodynamic prediction of oxide phases in Alloy 282 at (a) 1400˚F, and (b) 1600˚F.

The calculation results are correlated well with the observed free-surface oxide characteristics in Section 2.1. The observed oxide phases NiO, TiO_2, Cr_2O_3 and Al_2O_3 corundum, and Co-rich, Ni-Cr spinel in Alloy 282 were predicted at both 1400˚F and 1600˚F, among which Cr_2O_3 was predicted as the dominant oxide phase because of high Cr in the alloy composition (Table 1). Consistent with the observation of discrete TiO_2 and internal oxidation Al_2O_3, both oxide phases were predicted in low amount, mainly toward the low pO_2 end. The Al_2O_3 formation in place of γ' phase explains the sub-surface depletion of γ' in both 1400˚F and 1600˚F specimens.

The decrease in pO_2 leads to suppression of NiO and $NiCrO_4$ spinel in favor of Cr_2O_3 and Al_2O_3 corundum phases at both temperatures in Figure 48. This qualitatively correlates the observed difference in crack-tip oxide between air and steam environment, in particular the formation of Ni-contained oxide at the crack tip in 1400˚F air condition. In addition, comparing the difference between (a) and (b) in Figure 48 also highlights the effect of temperature on oxidation behavior: the higher temperature acts in a comparable way as the lower pO_2 does. This seems to be consistent with the observation of Cr_2O_3 and Al_2O_3 in 1400˚F steam, comparable to 1600˚F air, but not the 1400˚F air specimen.

The predicted level of oxygen for the steam-behavior ($\sim 10^{-16}\mathrm{atm}$) appears to be much lower than the equilibrium level of oxygen ($\sim 10^{-7}\mathrm{atm}$, see Figure 49) in 1 atm steam. This may suggest that the atmosphere near the crack tip is much different from that at the free surface. Consider that the crack tip is a highly confined volume where oxygen content can be notably influenced by gas flow and local oxidation reaction, and that in steam, oxygen is mainly supplied by the reaction $H_2O = H_2 + 1/2O_2$, a small variation in O_2 or H_2 concentration due to either oxidation or hydrogen accumulation can suppress pO_2 orders of magnitude (Figure 49). For the latter, it was reported[20] that hydrogen released by oxidation on 2-9Cr steel could leave up to 70% in the steam with only 30% diffusing through the metal wall. Although further characterization may lead to a more concrete explanation for oxidation behaviors in steam, the present simulation shows a correct trend of oxidation formation in Alloy 282 with respect to the pO_2 variation in air versus steam.

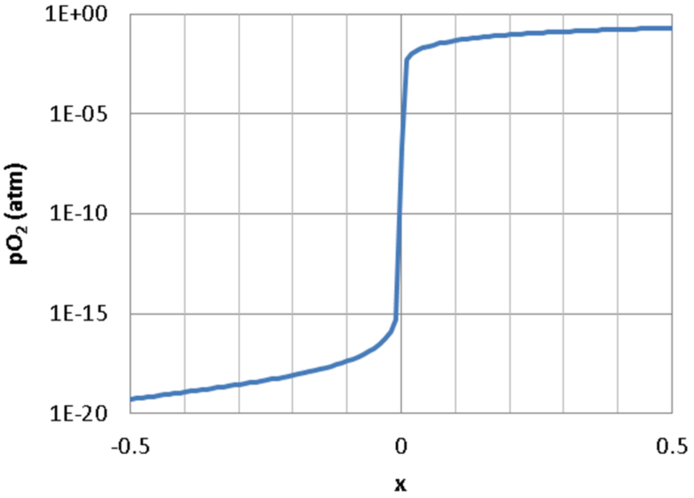

Figure 49: Calculated equilibrium O_2 partial pressure in 1 atm steam with variation of oxygen according to $H_2O_{1+x} \rightarrow H_2 + 1/2O_2$.

4.4. Mesoscale modeling of crack-microstructure-oxidation interactions

To facilitate a mechanistic understanding of crack behaviors under the combined effects of microstructure (grain boundaries) and environment (oxidation) in Alloy 282, we developed a mesoscale model that explicitly incorporated crack growth, oxygen diffusion, oxidation (phase transformation), and variations in local material properties. The cracks being addressed in this framework are at length scales comparable to grain structure, or “microstructurally short”. This approach also provides a potential means to bridge the outcomes of the experimental and atomistic studies and the continuum level modeling of crack behaviors.

4.4.1. Basic crack model

We adopt the phase field model of Jin, Wang et al [21,22] to treat mesoscale cracks. The size of the cracks is comparable with grain size. At this length scale, a crack is considered to reside on a crystallographic (cleavage) plane, and its growth direction can be a combination of different cleavage planes. The fundamental variable that describes a crack is the crack opening displacement vector, $\mathbf{h}$, as a function of spatial coordinate (see Figure 50). $\mathbf{h}$ is therefore a phase field defined in a 3D space and fully describes the geometry of a crack or a set of cracks. Furthermore, its mutual angle with the normal direction of the cleavage plane, **n**, gives rise to crack characteristic, for example a mode I crack or a mixed mode crack. Note this relation is not pre-defined, but a result of total energy driven phase field dynamic equation, which is in a form of [22]

$$\frac{\partial \mathbf{h}(\mathbf{x},t)}{\partial t} = -\mathbf{L}\frac{\delta[E^{coh}[\mathbf{h}(\mathbf{x},t)]+E^{el}[\mathbf{h}(\mathbf{x},t)]+E^{gr}[\mathbf{h}(\mathbf{x},t)]+W^{appl}[\mathbf{h}(\mathbf{x},t)]]}{\delta \mathbf{h}(\mathbf{x},t)} \qquad (4.4)$$

The right-hand side of Equation (4.4) is a variational derivative of the total free energy of the system with respect to the crack configuration (through **h**). It is essentially an analogous to a force term that drives proportionally the time evolution of a crack at the left-hand side of the equation. When a crack is at an equilibrium state, the right-hand side of Equation (4.4) becomes zero.

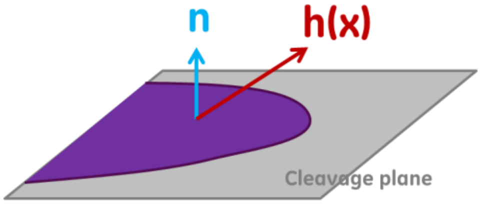

Figure 50: Phase field description of a crack.

For cracks, the total free energy was proposed [21] as a sum of four contributions, namely the cohesive energy E^{coh}, elastic energy E^{el}, gradient energy E^{gr}, and applied work W^{appl}. In the current approach the cohesive energy is linked to ab initio calculations (see Section 3.3). The elastic energy is formulated with the phase-field microelasticity theory of inhomogeneous body (i.e., elastic modulus varies in the space) [21], and can be extended to treat both crack and polycrystalline material in the same framework. Finally, the applied work term can treat different loading conditions, including strain or stress controlled, and can be extended to static or cyclic loading.

The phase field method adopts a cohesive zone type model [23,24] for crack. The crack behavior is controlled by not only the local stresses from elasticity, but also a counter-balancing cohesive force (or cohesive energy). The construction of the cohesive energy, E^{el}, reflects an atomistic nature of crystalline solids that acts against separation of atomic (crack) planes due to crack opening. In a simplistic way, as illustrated in Figure 51(a), the cohesive energy consists of a harmonic portion that represents a linear elastic behavior of the material at small displacement, and an inelastic portion at large separation displacement. Such a model gives rise to an (idealized) transition zone ahead of crack tip, in which a progressive decay of material strength is described.

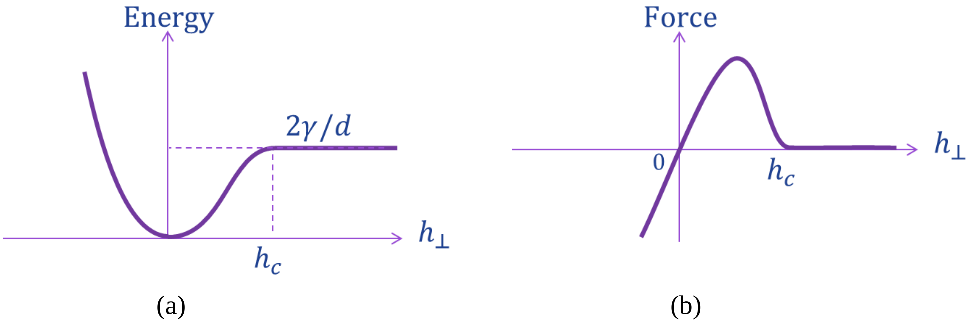

(a) (b)

Figure 51: Atomic resistance to separation of crack planes: (a) cohesive energy, (b) cohesive force.

Following the model of Wang et al [22], we chose the aforementioned simplistic form of the cohesive energy. The coefficients were determined from Young's modulus $E = 200GPa$, Poisson's ratio $\nu = 0.3$, lattice parameter 3.5Å, and surface energy $\gamma = 2J/m^2$, which are typical values for nickel. For a mode-I crack the corresponding critical separation distance is $h_c = \pi\sqrt{\gamma d/E} = 1.9$Å. Note these values can be tailored to better represent Alloy 282.

4.4.2. Basic model verifications

Equilibrium crack profiles

Figure 52 shows the opening profile of a mode-I crack in equilibrium with a tensile stress, σ^{appl}. The geometry corresponds to a plain strain condition. The crack opening profile exhibits a continuous transition at the crack tip, as shown in the enlarged inset on the right. In contrast, this transition zone at crack tip is absent in the traditional linear elasticity solution. For comparison, Figure 52 also includes the linear elasticity solution from a numerical calculation using the phase field inhomogeneous microelasticity theory [21] and an analytical solution based on dislocation pile-up model [25]. These calculations are similar to those in Ref [22] and were performed for verification purpose.

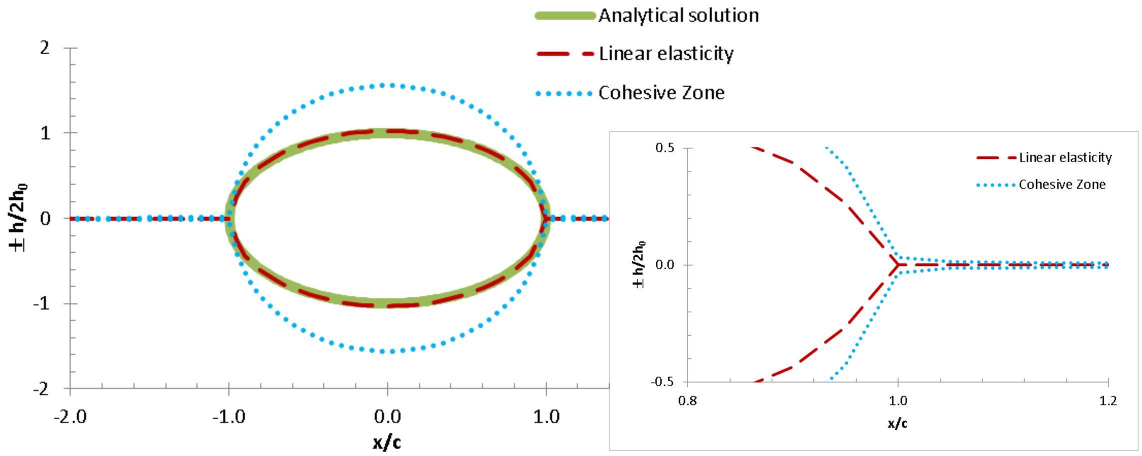

Figure 52: Crack opening profile of a mode I crack (length $2c$) under tension load. Comparison of cohesive zone (phase field), linear elasticity , and analytical solution of dislocation pile-up [25]. The comparison of the former two at crack tip is shown in the inset. The crack opening displacement is normalized by $h_0 = c(1-\nu)\sigma^{appl}/\mu$ (see also Ref [22]).

Validation of stress distributions at a crack

We have compared the stress fields of a stationary model-I crack between the numerical solutions from phase field simulation and the analytical solution (Figure 53). The size of the system was made relatively large (25*c,* where *c* is the half length of the crack) so that the stress distributions in the vicinity of the crack were not affected by the boundary condition used in the calculations. Two types of linear elasticity formulations in the phase field calculation were examined. The first is from the inhomogeneous microelasticity theory[22], where the volume occupied by a crack is treated with zero elastic modulus. The total strain energy was minimized via variation of an effective strain field, leading to a zero stress state inside the crack and appropriate stress distributions at the crack surface. The second formula is used in simulations of crack growth, where crack opening displacement fields are employed and the total energy consisting of strain energy and cohesive energy together determine the equilibrium stress distributions. Similar to other cohesive zone models, the second formula leads to a short continuous transition of crack-tip opening (a cohesive zone), instead of an infinitely sharp crack tip in the first formula. In Figure 54 the stress field components, σ_{xx}, σ_{yy}, τ_{xy} are displayed in the OXY quadrant (see Figure 53). Both numerical solutions are found to agree well with the analytical solution. Small wiggling of the contour lines at the crack plane ($y = 0$) corresponds to numerical fluctuations near zero stress. Note here the analytical solution actually represents a sharp crack tip. The inhomogeneous elasticity formula gives almost identical contour lines as the analytical solution, while the cohesive zone model solution shows a slight angular difference. It is considered primarily due to the difference of the crack opening profiles between the two approaches as shown in Figure 52. However the σ_{xx} and σ_{yy} profiles at the crack plane are seen to be very close among all the three solutions (Figure 55).

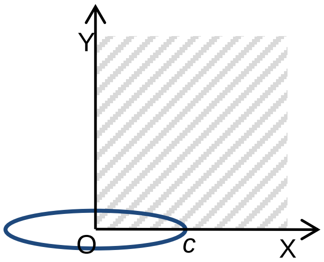

Figure 53: A schematic of a mode-I crack of length 2*c*.

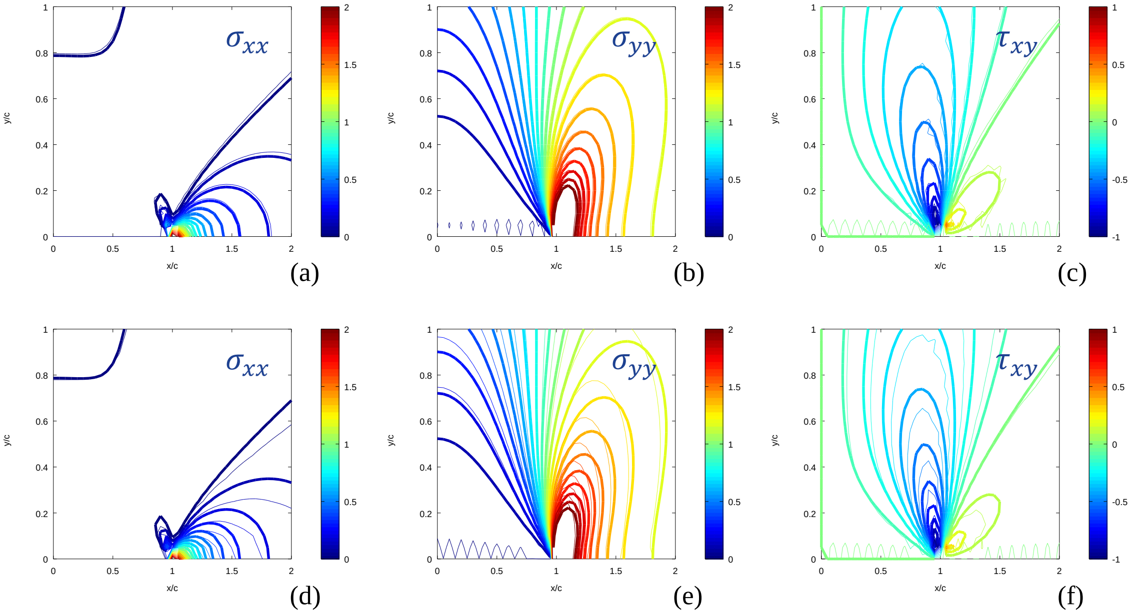

(a) (b) (c)

(d) (e) (f)

Figure 54: Comparison of stress distributions between analytical solution (thick contours) and numerical solutions (thin contours) from: (a-c) inhomogeneous elasticity and (d-f) phase field cohesive zone model. The area of the plot corresponds to the hatched region in Figure 53. The stresses are normalized by the applied stress.

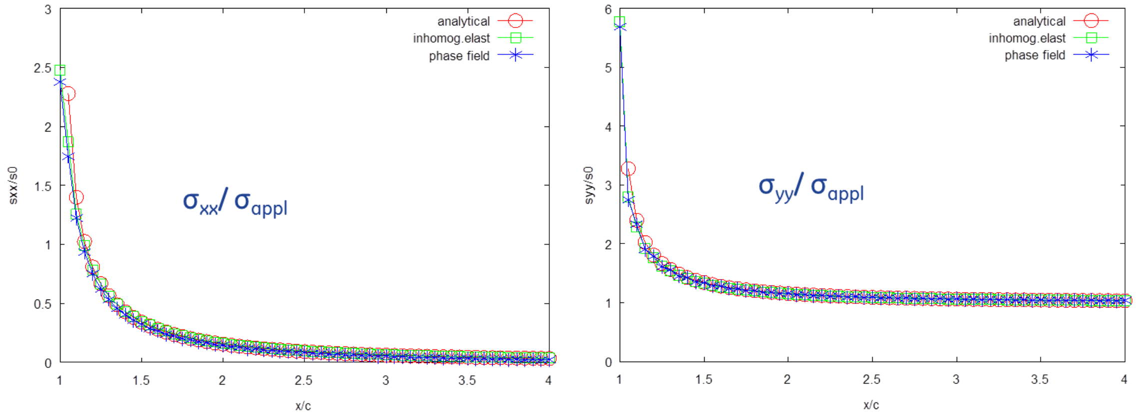

Figure 55: Comparison of stress profiles at the crack plane (along OX direction in Figure 53). The stresses are normalized by the applied stress. The shear stress τ_{xy} is zero and is not plotted here.

Figure 56 shows a mode-I surface crack under a static tensile load in “1” direction and the stress components σ_{11}, σ_{22}, and σ_{12} on the cross section plane. The color contours show the typical shape of stress distribution. Line profiles of σ_{11} and σ_{22} on the crack plane are plotted across the crack tip. It is noticed that the σ_{22} profile indicates a compressive component (in negative value) on the crack plane.

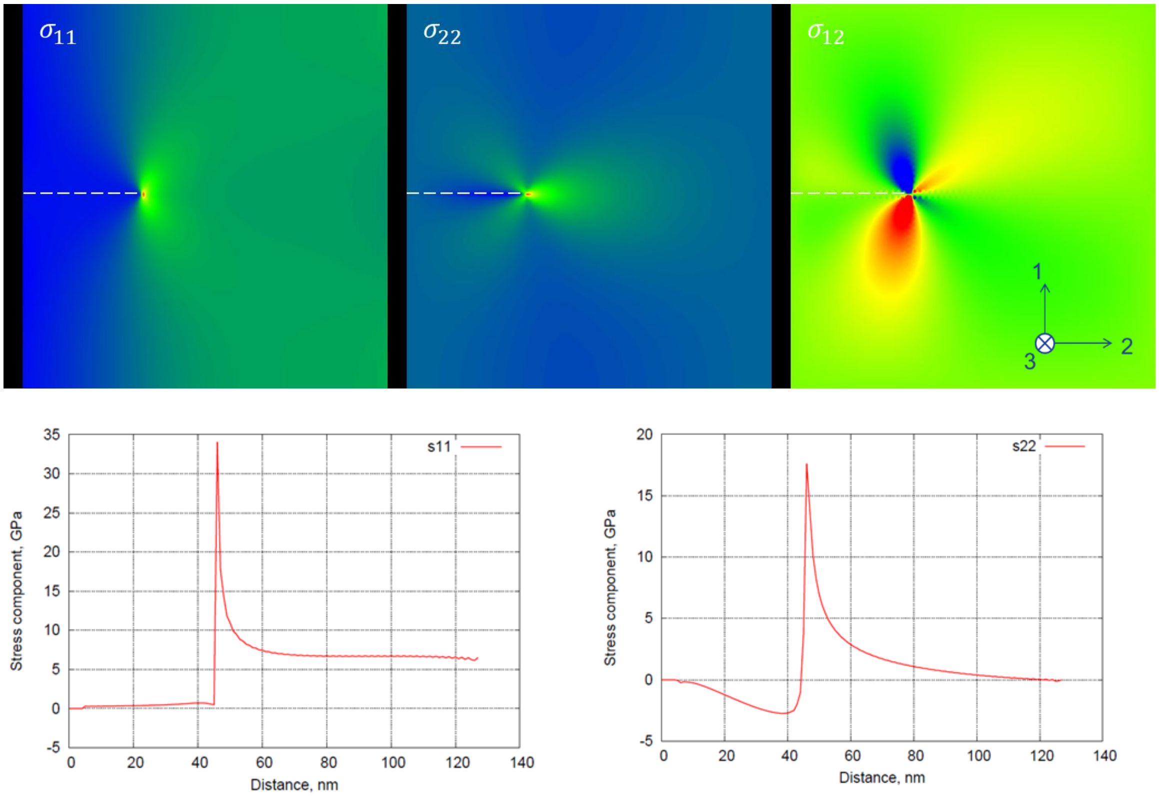

Figure 56: A mode-I crack (denoted by a dashed line) perpendicularly intersects a free surface, and the profiles of stress component, σ_{11} and σ_{22}, on crack plane. The applied stress is 7GPa, in “1” direction.

Validation of failure stress

The failure stress is associated with the maximum point (an unstable equilibrium) on the total energy curve of a crack at a given length. From a thermodynamic point of view, the crack should spontaneously grow once the applied stress exceeds the failure stress. The failure stress is thus a basic quantity that characterizes crack growth criteria under various stress state. The analytical model for the failure stress for a mode-I crack can be written as

$$\sigma_F = \sqrt{2E'\gamma/\pi c} \tag{4.5}$$

with γ the surface energy, $E' = E/(1-\nu^2)$ under plane strain condition, E the Young’s modulus, and ν the Poisson’s ratio.

Figure 57 shows a good agreement of the predicted failure stresses by the phase field crack model with the analytical solution (4.5). Each data point in Figure 57(b) was determined from multiple calculations, in which the applied stress was incrementally reduced until the equilibrium stress was found.

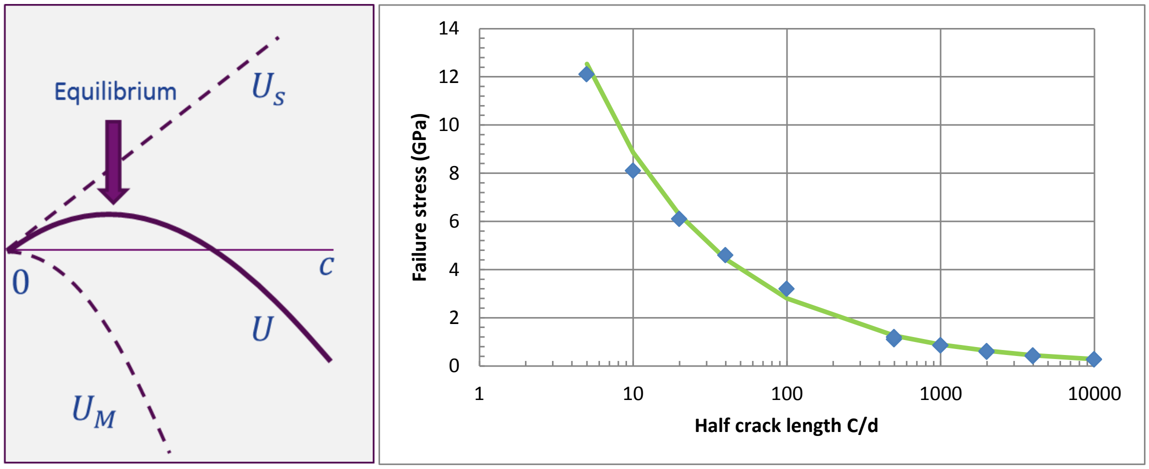

(a) (b)

Figure 57: Failure stress of mode-I crack with crack length 2c. The analytical solution is shown by the green curve in (b). The horizontal axis is normalized by interatomic spacing d. ($d = 3.52\text{Å}, E = 198\text{GPa}, \nu = 0.3$). U_S, U_M, U are respectively the surface energy, mechanical energy, and total energy of the crack.

Crack evolution

Just as in a cohesive zone model, in the phase field framework a crack will automatically grow when the applied stress exceeds the failure stress, which is dependent on crack size. The progress is driven by the variational derivative of the total energy of the system with respect to the crack configuration $\mathbf{h}(\mathbf{x}, t)$ (Equation (4.4)). The phase field total free energy allows incorporation of more complex microstructural features such as grain boundaries and oxides at a later stage. Figure 58 shows growth of a crack from an initial length of 20nm, under a constant tensile stress 4.5GPa. It is obviously seen that the growth is accelerated since the critical (failure) stress decreases with crack length as $\sigma_f \propto 1/\sqrt{c}$, i.e., a longer crack would require a smaller stress to drive it forward. A close look at the crack opening profiles at consecutive times (Figure 58(b)) indicates an initial stage (up to the reduced time 400 in Figure 58(a)) where the crack planes open up under the external load but the crack length does not increase with time. During this stage it can be shown by elasticity calculation that the local stress at the crack tip continuously increases. Once the stress exceeds a critical level, the cohesive force from atomic bonding can no longer withstand, and crack lengthening will begin. In this subsequent stage the crack opening profiles evolve in a self-similar manner, during which the shape of the profiles follows closely the contour of σ_{11} distribution.

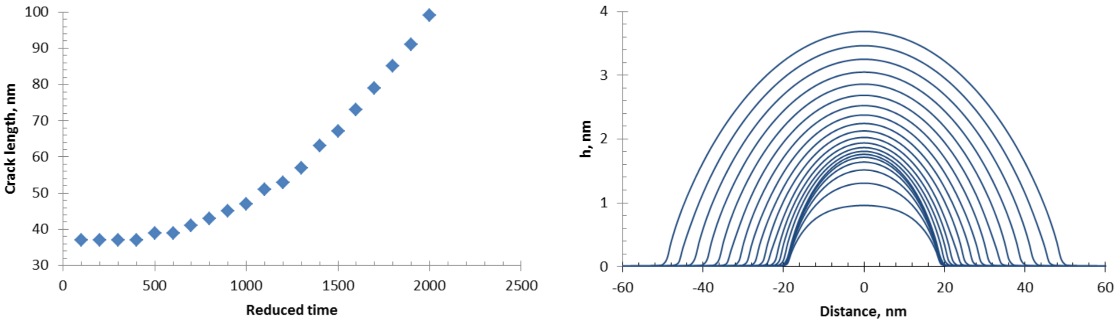

(a) (b)

Figure 58: Growth of a mode-I crack under a constant applied stress 4.5GPa: (a) crack length vs. time, (b) snapshots of the crack opening profile at a constant time interval.

At a given size, a crack in the phase field model can either grow or shrink, depending on the applied stress. Figure 59(a) compares the crack growth with the applied stress varied from 3 to 6GPa. The crack appears to remain stable at 4GPa, and grows increasingly fast at higher stresses. In each case the crack length versus time curve is shown in a parabolic shape. Under the lowest stress 3GPa, on the other hand, the crack continuously shrinks to zero length. This healing process is driven by the cohesive force. Such a situation can occur to brittle cracks when the fresh crack surface is not contaminated or damaged by plastic deformation [26,27], for example inside mineral crystals. Figure 59(b) compares the crack growth rate (d(2c)/dt) at different stresses. Since the crack growth rate varies with crack length, we compare its value at a fixed crack length (60nm) for all cases. The plot indicates a linear regime at relatively low stresses (below 5GPa) and then a nonlinear regime where the crack growth rate relatively slows down.

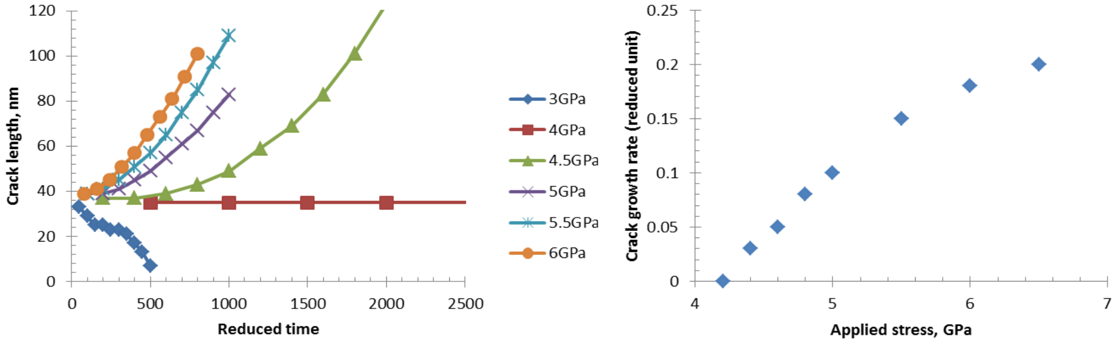

(a) (b)

Figure 59: Crack growth under different applied stress: (a) crack length, (b) crack growth rate measured at a fixed crack length 60nm.

4.4.3. Incorporate grain microstructure

The fatigue crack growth studies in Task 2 observed that failure in Alloy 282 switched from trans-granular to inter-granular cracking under an increased environmental effect, which was also found in other polycrystal Ni-base superalloys. This suggests a shift of the weak pathway for crack propagation between the bulk material and the grain boundaries. Generally speaking, grain boundaries are known to play an important role for environmental effects since they are usually the locations with enhanced oxygen diffusion and oxidation attacks, thus more significantly changing the local chemical and mechanical properties of the material. On the other hand, microstructurally short cracks are often seen to change propagation directions under the influence of local crystallographic orientation in the microstructure. Obviously, a model for addressing such environmental effects in polycrystalline alloys needs to take grain boundaries and orientations into appropriate account.

Extension of the phase field crack model to a polycrystalline system can be achieved by introducing a spatial-coordinate dependent rotation matrix[22], $Q_{ij}(\mathbf{r})$, which characterizes the rotation of the grains in a given microstructure. With the rotation matrix the description of cleavage plane can be generalized to

$$H_i(\alpha, \mathbf{r}) = Q_{ij}(\mathbf{r}) H_j^0(\alpha) \tag{4.6}$$

where the vector $\mathbf{H}^0(\alpha)$ designates the α^{th} cleavage plane defined in a local crystallographic coordinate attached to a grain at $\mathbf{r}$, while $Q_{ij}(\mathbf{r})$ transforms it to the global coordinate system (attached to the macroscopic body) and accounts for the rotation of the grain.

Although the rotation operation does not change the material's intrinsic (local) energies including the cohesive energy and the gradient energy, the rotation applied to the misfit strain (through $\mathbf{H}(\alpha, \mathbf{r})$)

$$\epsilon_{ij}^0(\mathbf{r}) = \sum_\alpha h_i(\alpha, \mathbf{r}) H_j(\alpha, \mathbf{r}) \tag{4.7}$$

in the elastic energy term does play a role in the long-range elastic interactions between crack and material and among cracks. Here the vector $\mathbf{h}(\alpha, \mathbf{r})$ is the crack opening displacement field that fully describes the crack geometry and spatial distribution in the polycrystal.

Figure 60 shows a simulation of crack propagation in a bi-crystal with the grain on the right side being rotated by 30˚ counter-clockwise. Since crack propagation in the phase field model always tends to follow crystallographic (cleavage) planes, the rotation of the grain results in a change of the crack direction, with the same 30° rotation, after the crack passes the grain boundary in the middle.

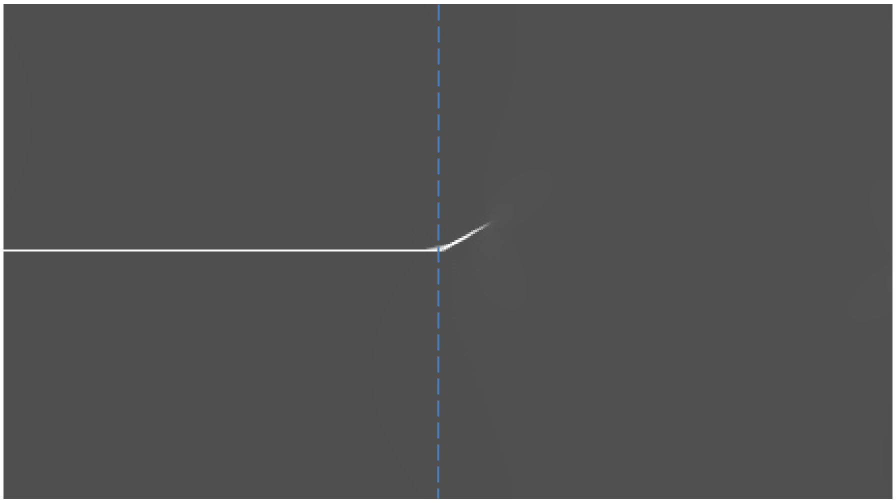

Figure 60: Crack deflection in a bi-crystal. The grain on the right is rotated by 30° counter-clockwise. The dashed line indicates the grain boundary.

To allow more realistic microstructures to be treated in the model, a two-dimensional grain structure was simulated with a phase field model. 40 grains (initial crystal seeds) with random orientations and initial locations were allowed to grow to occupy the entire area and further relaxed to develop grain boundaries with moderate curvatures (Figure 61).

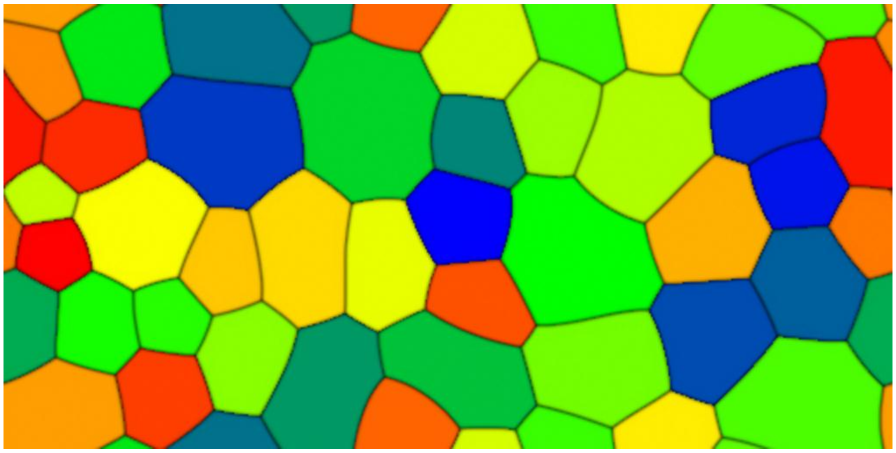

Figure 61: Simulated grain structure.

The simulated grain structure was then imported in crack simulations. In the particular simulation shown in Figure 62, a mode-I crack was initially placed in the center grain. A constant tensile force was applied in the vertical direction, which drove extension of the crack in both horizontal directions. After a momentary halt at the grain boundaries, the crack continued to propagate into neighboring grains, and simultaneously changed the direction due to the change in the grain orientation. Since in this case the applied force was fixed to a constant magnitude, during crack extension the effective load was shifted to the two sides of the material (as indicated by the color contrast in the figures) and the local stress continuously increased because of the reduced load bearing cross section. This as a result accelerated the crack propagation during the later stage.

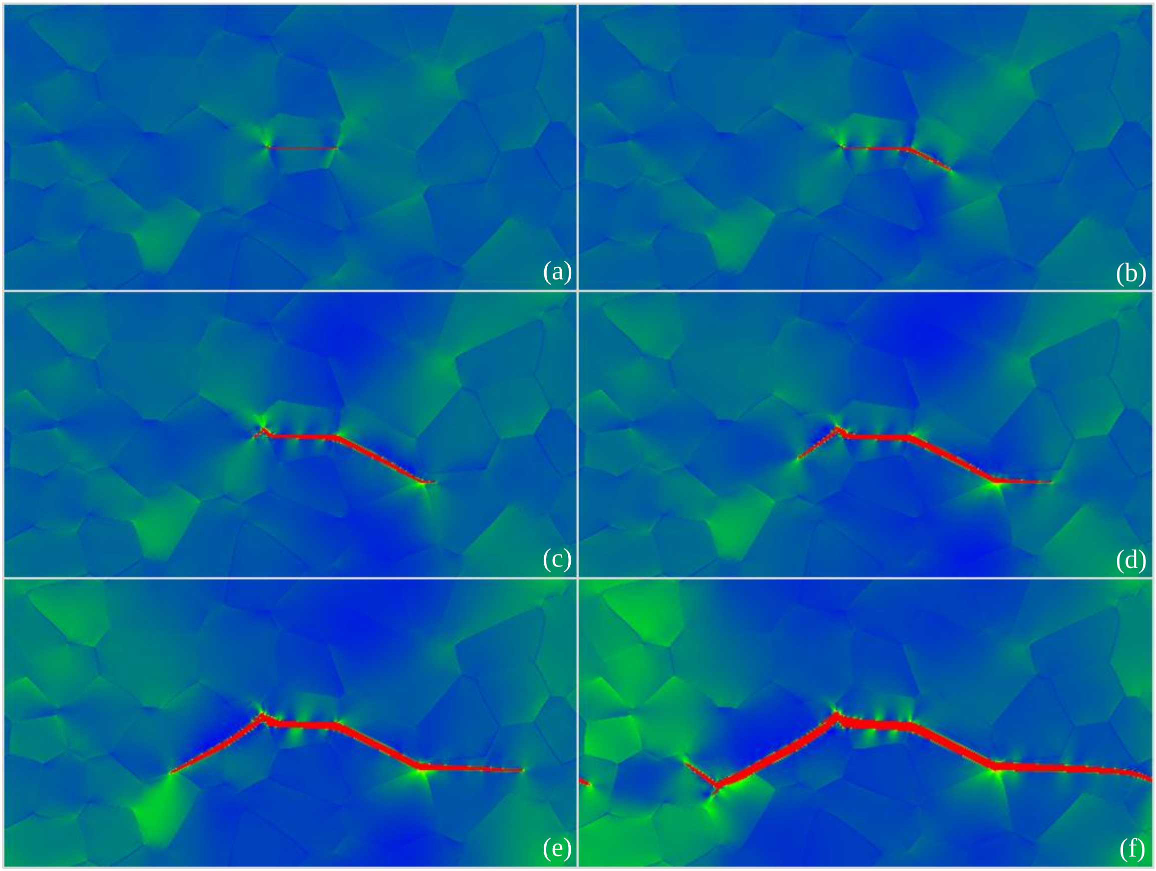

Figure 62: simulation of crack propagation in a polycrystal under a tensile load.

4.4.3. Incorporate plasticity

Plasticity is incorporated in the model to account for crack-tip yield in ductile materials. We adopt the von Mises yield criterion:

$$\sigma_e = \left[\frac{(\sigma_{11}-\sigma_{22})^2+(\sigma_{22}-\sigma_{33})^2+(\sigma_{33}-\sigma_{11})^2+6\left(\sigma_{12}^2+\sigma_{23}^2+\sigma_{31}^2\right)}{2}\right]^{\frac{1}{2}} \tag{4.8}$$

where σ_{ij} are the stress components. The yield occurs when the local von Mises effective stress σ_e exceeds the yield strength of the material. Subsequently a spatial distribution of plastic strain, ϵ_{ij}^{p}, is developed according to the local deviatoric component of the stress $s_{ij}(\mathbf{r})$: [28]

$$\frac{\partial \epsilon_{ij}^{p}(\mathbf{r})}{\partial t} = M s_{ij}(\mathbf{r}) = M\left[\sigma_{ij}(\mathbf{r}) - \frac{\mathrm{tr}\left(\sigma_{ij}(\mathbf{r})\right)}{3}\delta_{ij}\right] \tag{4.9}$$

Here for simplicity, the evolution of plastic strain is considered in proportion to the deviator stress with a constant factor M. The onset of the plastic strain results in a reduction in the local stress, and thus the driving force for further change in the former. Equation (4.9) ceases to act when either the deviatoric stress s_{ij} reduces to zero, or the von Mises effective stress σ_e falls below the yield strength. Note the plasticity evolution (4.9) applies to the entire space. It however has only captured a 'perfect plastic' behavior of the material. Work hardening behaviors could be further incorporated to the model in a straightforward way.

Figure 63 shows the calculated stress profiles across the crack tip (along OX in Figure 53) with and without plasticity. With an applied tensile stress 500MPa and yield strength 650MPa, the crack tip stress σ_{yy} is seen to reduce about 3 times due to plastic yielding. It is noticed that due to other stress components, σ_{xx} and σ_{zz}, the normal stress σ_{yy} at crack tip is still noticeable higher than the yield strength, while the von Mises effective stress does not exceed it.

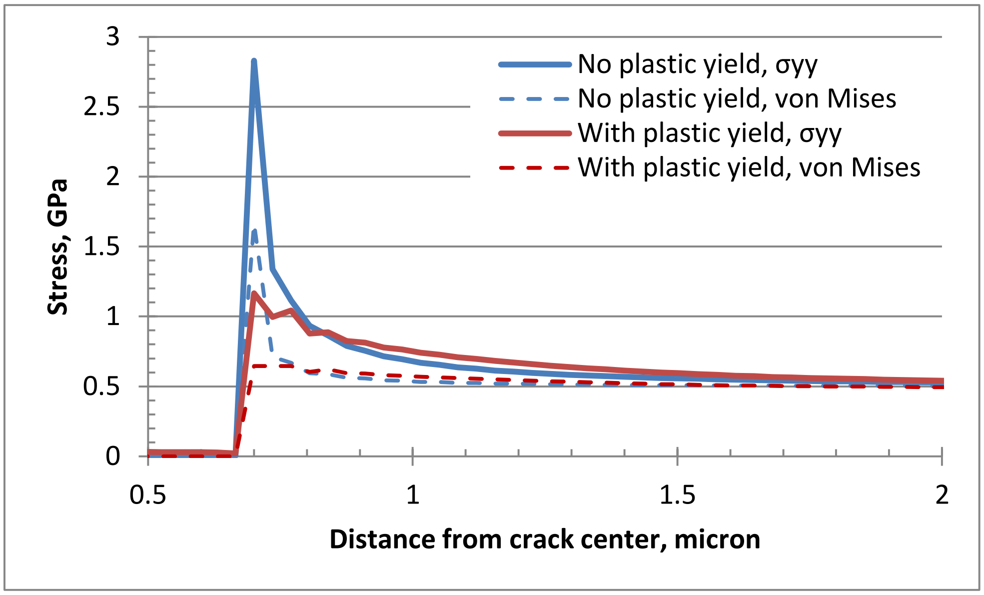

Figure 63: Calculated crack tip stress with and without plastic yielding.

A contour plot of the plastic strain ϵ_{ij}^{p} in Figure 64 outlines the plastic zone at the crack tip. The calculation corresponds to a plane strain condition since the depth along Z direction (normal to the display) is infinite due to periodic boundary condition. The shape of the plastic zone is seen to extend about 45˚ forward from the crack tip. It is seen that the plastic strain near the crack tip can be developed well over 30%.

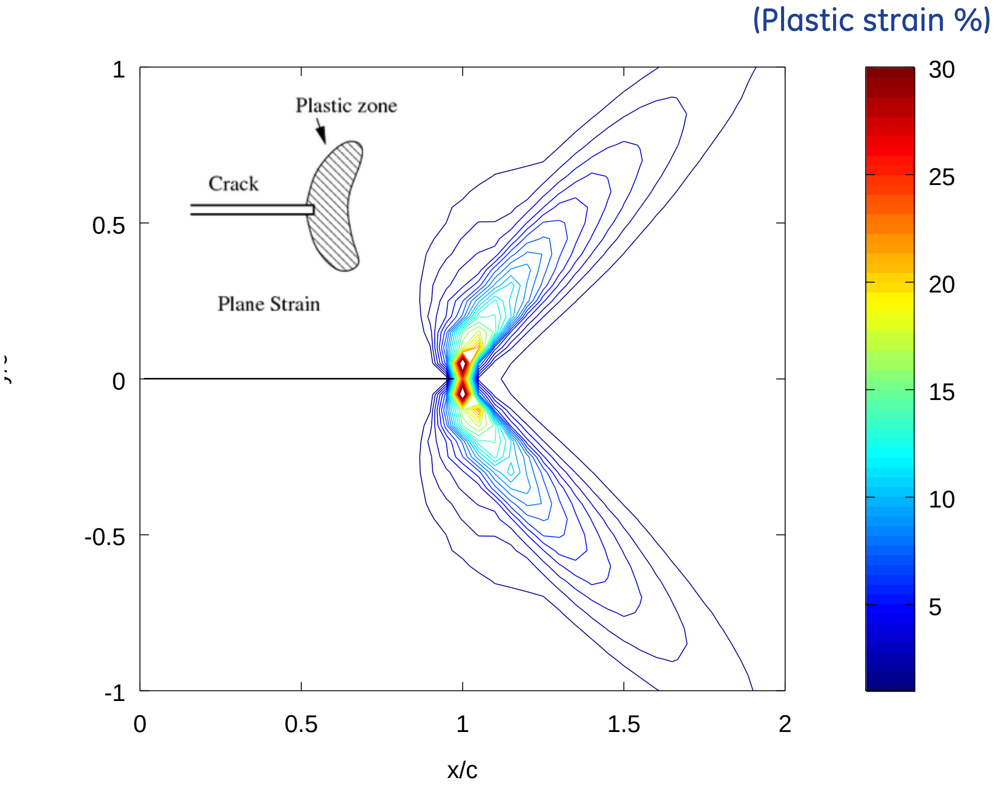

Figure 64: Spatial distribution of plastic strain near a mode-I crack under plane strain condition. The contour shows the shape and size of the plastic zone. The applied stress and yield strength are respectively 500MPa and 650MPa.

4.4.4. Incorporate oxygen diffusion and oxidation

Oxidation-crack interaction model

Figure 65 illustrates a minimal configuration of the model under consideration. More complex configurations with various grain structures can be treated in the phase field model. In this simple configuration, however, all the important ingredients are already illustrated. This includes co-existing alloy (metal) and oxide phase, diffusion, grain boundary, and crack. The oxygen source is applied at the surface of the oxide scale (the right end of Figure 65) where chemical potential (or equivalently, the partial pressure, or the activity) of oxygen is specified. The crack surface is assumed to maintain a similar oxygen environment as the external surface. Therefore the same oxygen condition is applied.

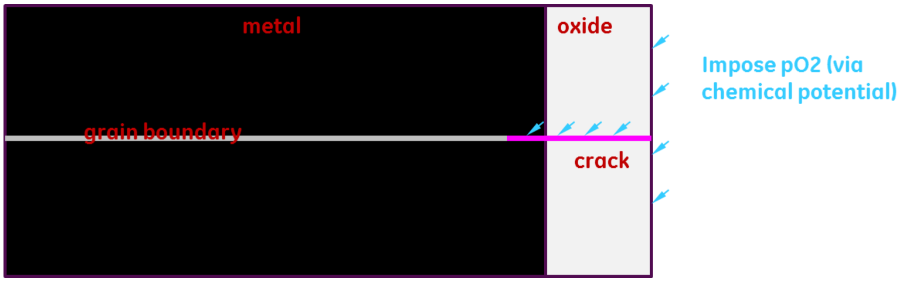

Figure 65: Basic configuration in the phase field model for oxygen-crack interactions.

In the model, oxygen transport in solid is governed by the generalized diffusion equation

$$\frac{1}{V_m}\frac{\partial X_O(\mathbf{r},t)}{\partial t} = -\nabla \cdot J(\mathbf{r},t) = -\nabla \cdot [-M(\mathbf{r},t)\nabla\tilde{\mu}(\mathbf{r},t)] \qquad (4.10)$$

where X_O is the concentration (atomic fraction) of oxygen, as a function of spatial coordinate $\mathbf{r}$ and time t. V_m is molar volume. J is diffusion flux. $M(\mathbf{r},t)$ designates chemical mobility of oxygen, which can be related to chemical diffusivity by thermodynamic factor. The generalized chemical potential, $\tilde{\mu}$, is given as [29]

$$\tilde{\mu}(\mathbf{r},t) = V_m\left[\frac{\partial f}{\partial X_O} - \kappa\nabla^2 X_O(\mathbf{r},t)\right] \qquad (4.11)$$

with κ the gradient coefficient. At a sufficiently high oxygen concentration, oxidation occurs via phase transformation. The formation of oxide phase and its equilibration with the metal phase is governed by the chemical free energy, f, in (4.11). Since we particularly consider grain boundary oxygen segregation in additional to the 'bulk' (intra-grain) property, the chemical free energy f includes both contributions, namely, f_{gb} for grain boundary and f_0 for the bulk. In particular we use the form

$$f = f_{gb}(X_O)\phi(\mathbf{r},t) + f_0(X_O)[1-\phi(\mathbf{r},t)] \qquad (4.12)$$

with $\phi(\mathbf{r},t)$ designating the grain boundary, which has a value continuously varied from 1 at grain boundary to 0 away from the grain boundary. Equation (4.12) essentially is a linear interpolation function that gives a smooth transition of the free energy from that at grain boundary to that in the bulk. For simplicity, in the subsequent simulation cases, ϕ is pre-determined by the given grain structure and does not evolve with time.

The basic interactions between oxygen and crack are treated in two aspects. The first is that crack provides shortcut passageway to oxygen transport, so that oxygen is delivered right to the crack surface including the neighborhood of crack tip. In the model this is done by coupling the oxygen 'boundary condition' and the crack opening displacement field: at any location $\mathbf{r}$ where the normal component of the crack opening displacement field, $h_n(\mathbf{r},t)$, exceeds the critical crack opening h_c (see Section 4.4.1), the chemical potential of oxygen is modified to a value identical to the external environment. As a result, a propagating crack would dynamically change the oxygen environment along its pathway.

The second aspect of the interactions is that the locally evolved oxygen concentration changes the local mechanical property of the solid, in particular the cohesive strength. In the current model we couple the effective surface energy term in the cohesive energy (Figure 51) to both oxygen concentration $X_O(\mathbf{r},t)$ and grain boundary field $\phi(\mathbf{r},t)$.

$$\gamma = \gamma_{gb}(X_O)\phi(\mathbf{r},t) + \gamma_0(X_O)[1 - \phi(\mathbf{r},t)] \tag{4.13}$$

where γ_{gb} and γ_0 are respectively the effective surface energy at grain boundary and in the grain interior. In general as the cohesive strength reduces, the resistance to crack propagation is reduced, and the crack growth is accelerated.

Model inputs from ab initio calculation

The ab initio calculations (Section Task 3.3) have established basic inputs to the model above. The chemical free energies for Ni-O solution phase and NiO oxide phase are re-plotted in Figure 66(a). We used cubic spline to fit a smooth free energy curve with the data. For simplicity, we chose to treat the two phases with a single double-well shape free energy curve. This is given as f_0 in Equation (4.12). The simplification of the single free energy curve can be relaxed when ordering kinetics of Ni-O to NiO becomes of interest. In such a case, an additional long-range order parameter field would be introduced. The free energy at grain boundary, f_{gb}, is given in Figure 66(b), similarly fitted with a smooth cubic spline curve for use in the phase field model. Note here the units of the ab initio data (Figure 17) have been converted from eV/atom to J/mol. Also, the data have been subtracted by a common tangent line, which is associated with the choice of the reference state of Ni and NiO. It can be shown that this subtraction does not affect the phase field equation (4.10).

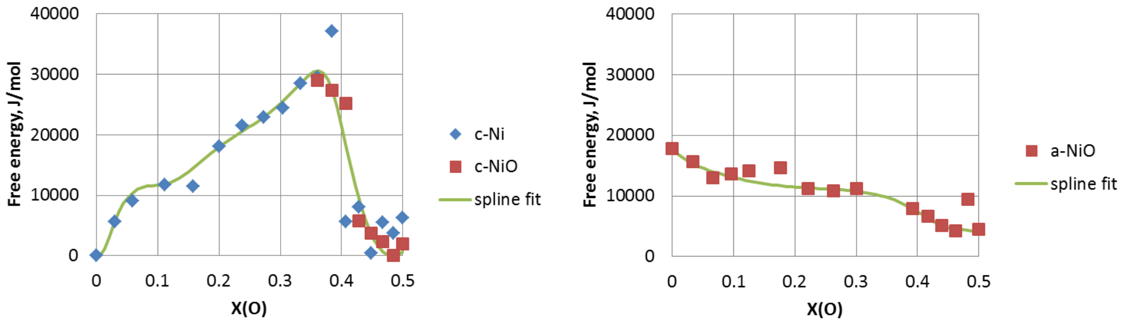

(a) (b)

Figure 66: Chemical free energies from ab initio calculation for (a) Ni-O (c-Ni) and ordered NiO (c-NiO), and (b) grain boundary Ni-O (a-NiO). The fitted cubic splines are used in the phase field model.

We approximated the weakening effect of oxygen on cohesive strength (or γ in Equation (4.13)) to be proportional to the oxygen effect on the ideal fracture strength of the base metal (Figure 67). In particular, the slope of grain boundary γ_{gb} versus oxygen concentration is taken the same as of the a-NiO$_x$ curve in Figure 67.

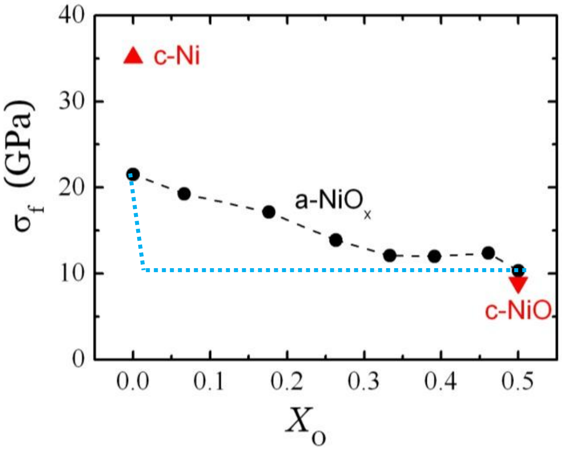

Figure 67: Ideal fracture strength of Ni with various oxygen concentration from ab initio calculation (same as Figure 20). The blue dotted line is a hypothetical modification with increased sensitivity to low oxygen concentration.

A material parameter left to determination is the chemical mobility of oxygen, M, in Equation (4.10). We chose to allow a spatial (microstructure) dependence of this parameter in order to treat different diffusion rate of oxygen in metal bulk, grain boundary, and through oxide. In the same fashion as for the chemical free energy and the effective surface energy, we write the chemical mobility

$$M = M_{gb}(X_O)\phi(\mathbf{r},t) + M_0(X_O)[1-\phi(\mathbf{r},t)] \quad (4.14)$$

with

$$M_{gb}(X_O) = M_{gb}^O \tilde{X}_O(\mathbf{r},t) + M_{gb}^M[1 - \tilde{X}_O(\mathbf{r},t)]$$
$$M_0(X_O) = M_0^O \tilde{X}_O(\mathbf{r},t) + M_0^M[1 - \tilde{X}_O(\mathbf{r},t)] \tag{4.15}$$

where M_{gb}^M, M_{gb}^O, M_0^M, M_0^O are respectively the mobility of oxygen in metal grain boundary, oxide grain boundary, metal lattice, and oxide lattice. The normalized oxygen concentration by the equilibrium oxide concentration $\tilde{X}_O = X_O(\mathbf{r},t)/X_O^{eq}$ is used as a weighting factor. Note, however, (4.15) is rather simplistic and can be replaced by the diffusivity calculation results in Task 3 (Section 3.5.2).

4.4.5. Modeling crack-microstructure-oxidation interactions

First, we considered oxygen transport in base metal and oxide. The values of the four mobility terms in Equation (4.15) were chosen in a parametric way, as shown in Table 5. In particular, Run 2 reduced the mobility in oxide lattice, and Run 3 further reduced the mobility in grain boundary oxide. The mobilities in metal were always kept same and the mobility at metal grain boundary was set somewhat (2X) higher than in the metal lattice.

Table 5: Three sets of oxygen mobility values used in the simulation.

	Run 1	Run 2	Run 3
Metal lattice M_0^M	1	1	1
Metal GB M_{GB}^M	2	2	2
Oxide lattice M_0^O	0.1	0.02	0.02
Oxide GB M_{GB}^O	0.5	0.5	0.04

Figure 68 shows growth of external oxide scale in the configuration illustrated earlier in Figure 65. A constant oxygen chemical potential is applied at the right-hand side of the oxide scale. The scale thickness is measured some distance away from the location of grain boundary, as indicated by the red arrows in Figure 68b. It is apparent from the difference between Run 1 and Run 2 that the growth of oxide scale is directly influenced by the mobility in oxide lattice, M_0^O, since oxygen has to diffuse through the bulk oxide scale in order to react with the metal element. Between Run 2 and Run 3 it is also seen that the difference in mobility in oxide grain boundary, M_{GB}^O, does not greatly affect the oxide scale growth. This is a reasonable behavior as one can notice in this particular configuration the grain boundary diffusion contributes only a small portion to the overall oxide growth. Finally, the initial growth of oxide scale is seen rather rapid, and only at a later stage the curves become more parabolic as in a diffusion-controlled kinetics.

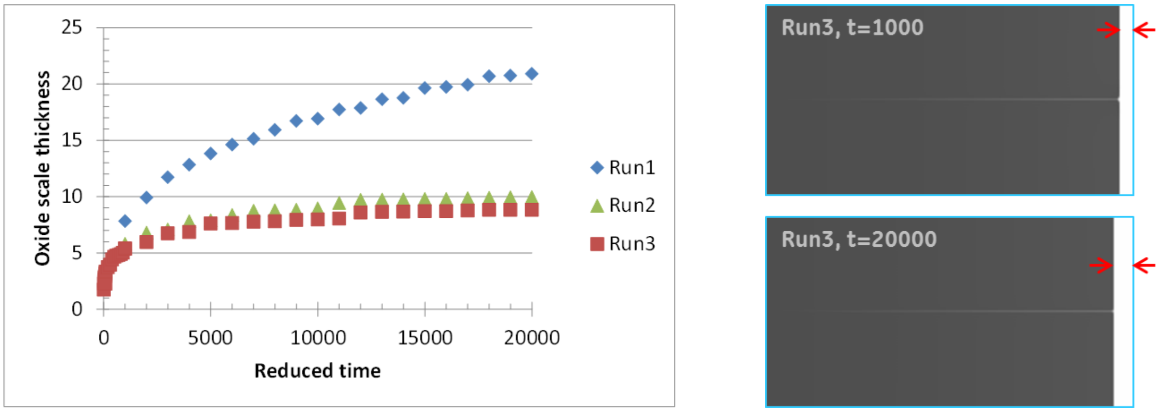

(a) (b)

Figure 68: (a) Simulated oxide scale growth. (b) Snapshots at two different times in Run 3. The grayscale contrast corresponds to oxygen concentration. The time unit is 960s, and the length unit is $1\mu m$.

The lighter contrast on the middle grain boundary in Figure 68b indicates penetration of oxygen along the grain boundary ahead of the growing oxide scale. This can be seen more clearly at the earlier stages, shown in Figure 69. Note the time scale is several orders of magnitude shorter compared with that of the growth of external oxide scale (Figure 70). For comparison, in Figure 69(b) we also plot the oxygen concentration profiles (dotted lines) away from grain boundary. The narrower diffusion profiles are mainly due to the lower mobility M_0^M as compared with M_{GB}^M. Note these diffusion profiles span in the low oxygen concentration range. Therefore the mobility is mainly determined by the metal diffusion instead of oxide scale, according to Equation (4.15).

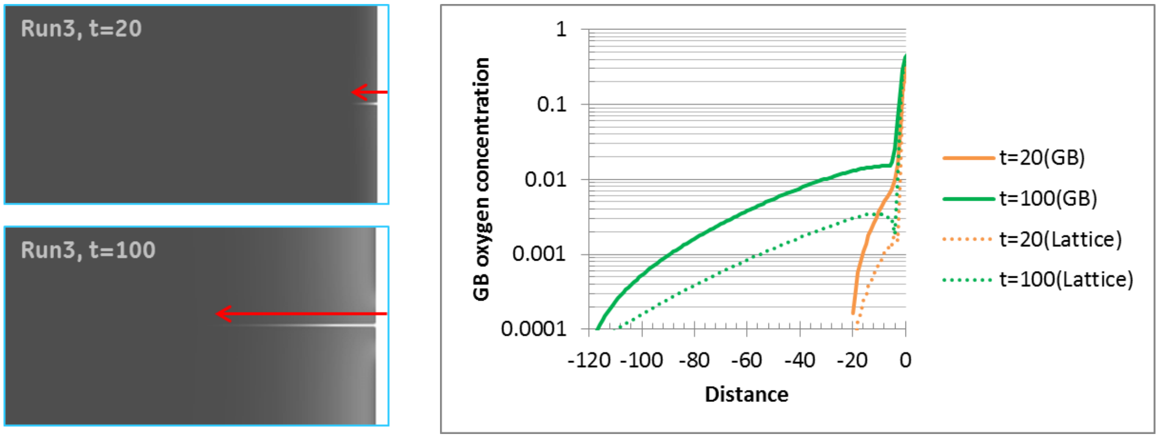

(a) (b)

Figure 69: Oxygen penetration along grain boundary. The bright vertical band at the right end of (a) is the external oxide scale. The corresponding oxygen concentration profiles are plotted in (b). For comparison the oxygen profiles in metal lattice (away from grain boundary) are also plotted. The time unit is 960s, and the distance (length) unit is $1\mu m$.

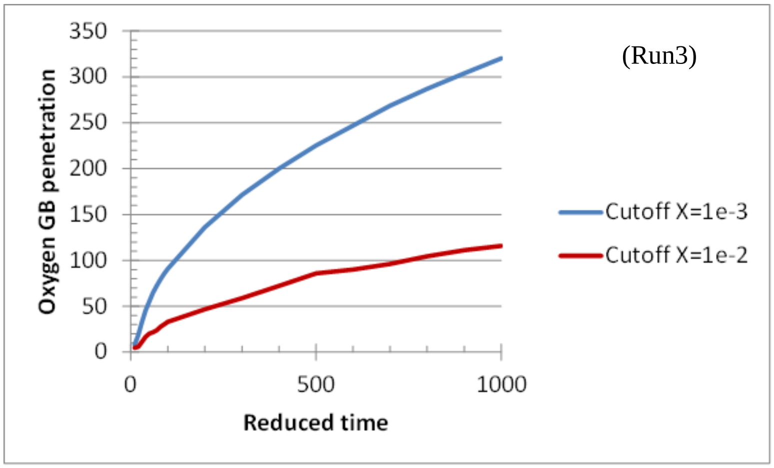

Figure 70: Oxygen grain boundary penetration depth with time. The two curves correspond to different cut off value of oxygen concentration in order to determine the extent of the penetration (see also Figure 69(b)). The time unit is 960s, and the length unit is $1\mu m$.

By incorporating oxygen diffusion and oxidation into the phase field crack model, we were able to simulate interactions between oxygen and crack propagation. Figure 71 summarizes the results from a series of simulations with different mobility values (Table 5) and interaction mechanisms. The case (a) in Figure 71 represents the same situations shown above, i.e., diffusion and oxide growth in an absence of crack. The main variation in oxide scale thickness and grain boundary oxygen penetration was determined by the different mobility values. In case (b), a crack was introduced and grew under a fixed applied tensile load. Oxygen was allowed to quickly distribute at crack surface by applying a constant oxygen chemical potential along the growing crack. The effect on the mechanical property however had not been introduced, so that the crack growth was not influenced by oxygen content. The weakening effects on cohesive strength due to oxygen, characterized by Figure 67 and Equation (4.12), were taken into account in case (c). In this case, with increased oxygen concentration the fracture strength was reduced, thus crack growth was promoted. In particular, as the fracture strength along grain boundary was reduced by a factor of 2 (Figure 67) when oxygen concentration varied from zero to 0.5 (the stoichiometric concentration of NiO), the growth rate of the crack was about twice in case (c) as compared with case (b) under the same applied load. Comparing the effect of oxygen mobilities among Run1-3 suggests that in these cases the oxide scale thickness is mainly determined by the mobility in oxide lattice, M_0^O. This is a reasonable result since in the current model we are not treating oxide with a polycrystalline structure so that grain boundary diffusion in oxide does not play an essential role in oxide scale growth.

On the other hand, we find in case (c) that crack growth under the influence of oxygen does not show great variation among different mobility values, even though they all show an increase in crack growth. This seems to indicate that the acceleration in crack growth does not depend on the oxygen penetration (or grain boundary segregation) ahead of the crack tip. In addition, it is neither sensitive to how fast the oxide scale grows. Rather the acceleration of crack growth seems to be the result of oxidation of just a thin layer of material at the crack tip, which is then fractured to allow fast delivery of oxygen to the moving crack tip.

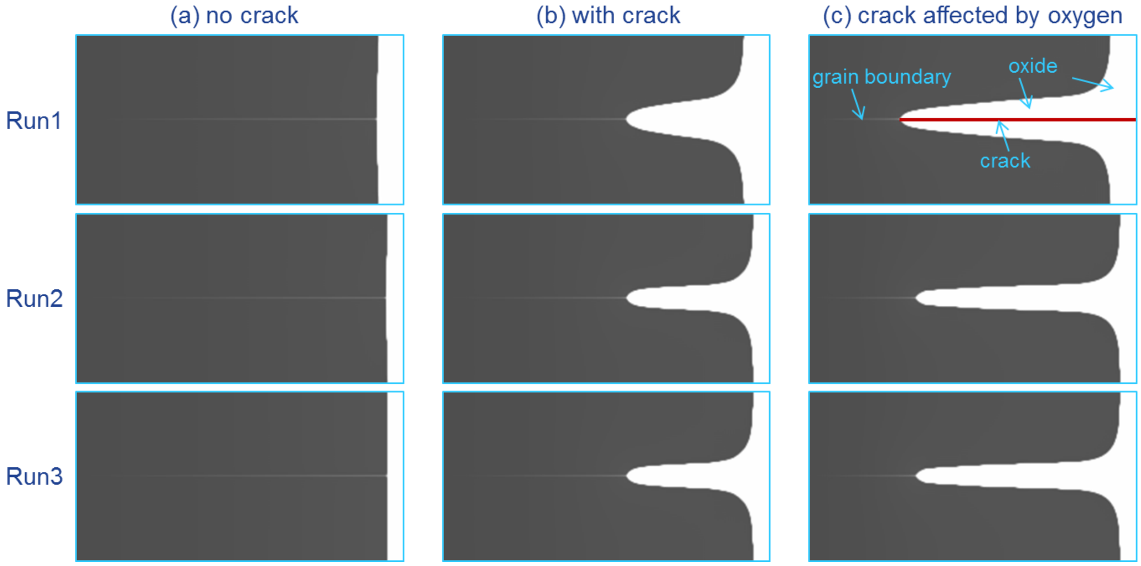

Figure 71: Snapshots of oxygen concentration distribution in different simulation cases. The upper right figure gives notation of each factor considered in the simulation. All the snapshots are taken at the same dimensionless time t=8000 (the time unit is 960s).

Such a damage mode appears to favor the SAGBO mechanism than dynamic embrittlement discussed in Section 3.1. By examining the ab initio calculation results of grain boundary strength in Figure 67, we find that the oxygen weakening effect is fairly moderate over the range of oxygen concentration. In addition, the free energy of the grain boundary phase (Figure 66(b)) suggests that the grain boundary oxygen concentration is typically less than 0.1 in atomic fraction. At this level of segregation, the grain boundary strength is only reduced about 10% (Figure 67). This is different from the characteristic of dynamic embrittlement discussed earlier in Section 3.1, that a very small amount of oxygen would weaken the grain boundary strength ahead of crack tip significantly.

While the sensitivity of grain boundary strength to oxygen concentration and grain boundary structure would be an important subject to further explore in the future, here we give a hypothetical modification to the ab initio results to enhance the effect of oxygen. The blue dotted line in Figure 67 considers a rapid decrease in grain boundary strength at low oxygen concentrations up to 0.01, in atomic fraction, and then saturated at the same level at the highest concentration. With such a construction, crack growth was found to switch to an inter-granular cracking mode as shown in Figure 72(a-c). In fact the initial crack (shown by the arrow in Figure 72(a)) did not continue to grow, while a second crack (in yellow circle) was found to form nearby. The oxygen concentration contour (Figure 72(d)) indicates that at this time, oxygen in the surrounding area of the initial crack has reached some critical level (X_O=0.01) through grain boundary diffusion. In principle the initial crack could continue to grow by switching its direction toward grain boundary. However the grain boundaries intersected by the crack were oriented in an unfavorable direction with respect to the applied load, which was in the vertical direction of the figures.

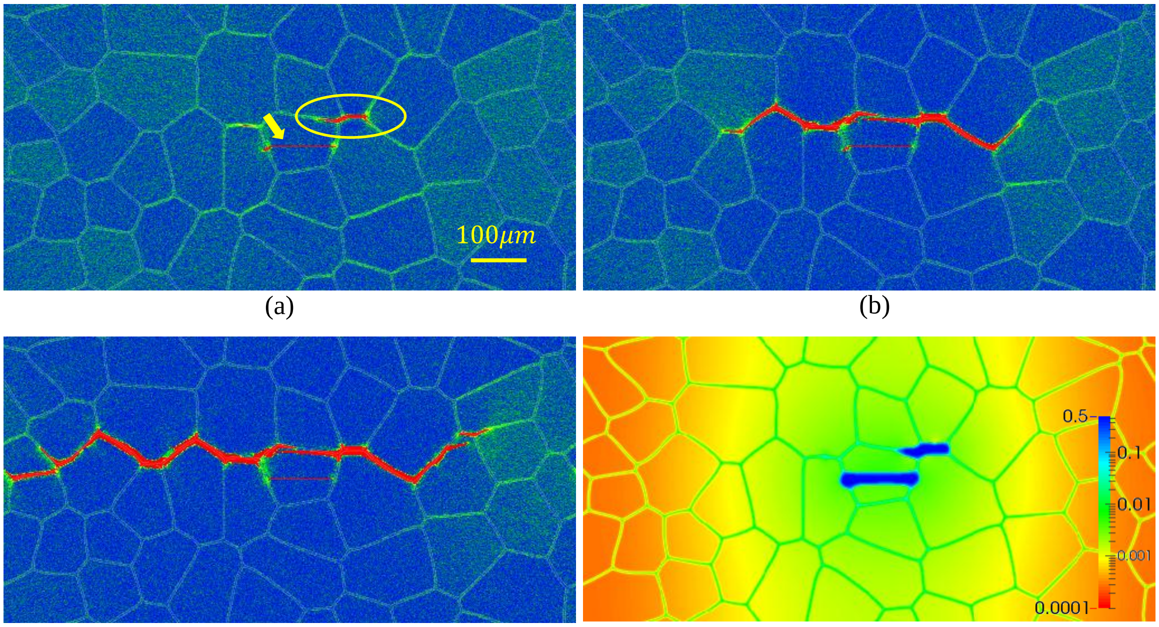

(a) (b)

(c) (d)

Figure 72: Crack growth under oxygen effect by using the blue dotted line in Figure 67: (a)-(c) snapshots at 82, 97, and 124hrs; (d) shows oxygen concentration distribution at the same time of (a).

For comparison, we also simulated the same conditions but used the original calculation result (the black dashed line in Figure 67(a)) and, in a third case, without the oxygen effect. The results are shown respectively by Figure 73(a) and (b). In both cases, we found the crack growth remained mainly trans-granular. While the overall growth rates were both slower, the case without oxygen effect was the slowest.

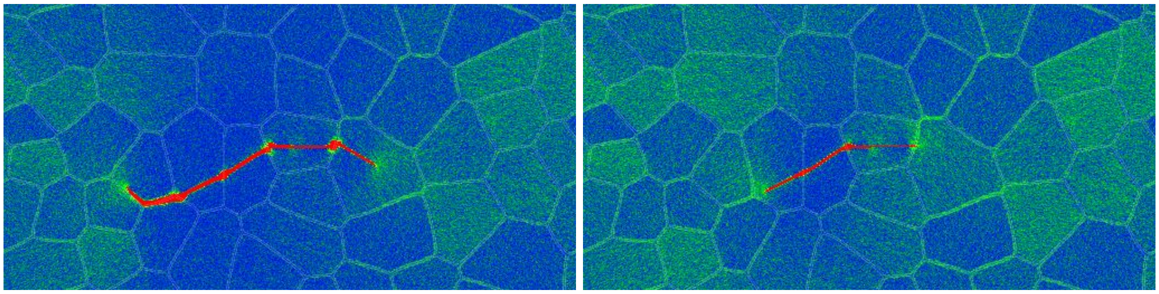

(a) (b)

Figure 73: (a) Crack growth under oxygen effect characterized by the ab initio result, the dashed line in Figure 67, and (b) without oxygen effect. Both are snapshots taken at the same time as Figure 72(c).

4.5. Summary and discussion

Alloy 282 gamma prime microstructures were quantitatively modeled. Precipitation model and phase field model were applied to Alloy 282, calibrated to short-term experiment data, and validated by lab aging heat treatment data in the range of 1300-1650˚F for up to 8000 hours. Precipitate spatial distributions and particle morphologies from phase field modeling were also validated against experimental observations. Gamma prime coarsening was then predicted for long-duration thermal exposure under A-USC conditions for up to 20 years. The simulated microstructures were reduced to inter-particle spacing and gamma prime volume fraction, which were provided to the creep modeling in Task 5.

Thermodynamic modeling of oxides in Alloy 282 was used to understand the experimental observations of oxidation at both free surface and crack-tip fracture surface in Task 2. The oxygen partial pressure, due to either testing environment or the location of the oxides in the specimen, and temperature effects on oxide phase formation were found in agreement with the experimental observation. In particular, lower oxygen partial pressure (such as in steam environment) and higher temperature (1600˚F) tended to suppress formation of NiO and Ni-Cr spinel phases at crack tip.

Growth of microstructurally short cracks in the polycrystalline alloy was modeled with the phase field method. Grain orientation and grain boundaries were explicitly treated. Environmental effects due to oxidation and spatial oxygen diffusion on crack propagation were incorporated, with inputs from the ab initio modeling in Task 3. Simulations of crack growth under the combined oxidation and microstructure effects indicated that crack growth rate and pathway (trans-granular vs inter-granular) could be sensitively dependent on the relative speed of crack growth with respect to oxygen diffusion, oxide formation, and on the sensitivity of grain boundary strength to oxygen concentration.

The application of phase field framework to crack modeling in Task 4 has demonstrated a potentially powerful way to incorporate microstructural and environmental interaction factors, which are not typically treated in conventional finite element methods. It can become particularly beneficial when dynamic evolution of microstructure and/or environmental (e.g., oxidation) effects are playing substantial roles. The latter is obvious in the context of the discussion of SAGBO vs. DE cracking mode in Section Task 3. Ultimately the crack evolution under various aforementioned factors, through phase field simulations, can provide inputs to finite element modeling in a way comparable to what experimental testing does, i.e., a *continuous* crack growth rate as loading conditions, microstructures, and environmental effects are varied. It should be noted that providing this type of input is also non-trivial for experimental testing, which requires advanced crack detection techniques with fine time-resolution or in-situ capabilities. At present, however, a direct link of phase field crack modeling to finite element and crack-tip plasticity based modeling (in Task 6) appears to be difficult. There are two main challenges learned from the current study. First, an adequate constitutive material behavior model for the phase field crack model is lacking. Second, the loading and boundary conditions are rather simplistic, which include only constant force or constant strain rate. These factors have restricted the outcome of phase field crack modeling to only a qualitative, mechanism focused study in the present program. However, future work can employ a similar approach as in the finite element methods (see Section 6.2) to establish a constitutive material model in the phase field framework. In the meantime, implementation of adaptive numerical methods appears to be important for overcoming both time and length scale limit, which in turn would allow the phase field crack model to employ the realistic loading and boundary conditions.

Task 5: Microstructure and damage-based creep prediction

The goal of this task is to understand the controlling mechanisms of creep deformation in Alloy 282 under A-USC steam turbine operation conditions, to develop a model capable of capturing the experimentally observed creep behaviors, and to predict the long time creep performance of the alloy.

5.1. Historical creep study on Alloy 282

A series of creep study were performed in the past with peak-aged Alloy 282. The alloy was processed with solution annealing (2050-2100˚F followed by air cool) and additional 8 hours aging at 1450˚F. The additional aging step resulted in coarser precipitate size (20-50nm), compared with 5-15nm in the "as produced", solution annealed microstructure. These creep tests were performed at various stresses between 15Ksi and 45Ksi and temperatures between 1375˚F and 1450˚F. The minimum requirement for a steam turbine rotor alloy in an A-USC coal-firing power plant includes yet a lower stress at about 5Ksi at 1400˚F.

The creep curves at 1400˚F are presented in Figure 74. The raw experimental data has been numerically smoothed for better display. These curves exhibit three typical regimes: a primary creep regime with a rapid increase in strain; a secondary creep regime with a slower, sometimes steady-state, increase in creep strain; and a tertiary creep regime where the strain increases again rapidly until rupture. The span of each regime varies under test conditions. At high stresses (>35Ksi), the secondary regime is very transient. Typically, the creep strain rate curve shows a convex shape, with a minimum value commonly referred to as the "minimum creep rate". The creep tests under high stress were performed up to rupture. At intermediate stresses (20 - 35Ksi), the creep curves show a wider secondary regime with a constant strain rate (the "steady-state strain rate"). Some of these tests (i.e. 27.5Ksi, 32.5Ksi) were interrupted before rupture for characterization of deformation microstructures. At low stresses (15 - 20Ksi), the creep curves show a much extended steady state. Note that even after more than 10,000 hours the secondary creep was still present without any indication of tertiary regime initiation. These tests were interrupted before rupture since they would take too long time to failure (estimated over 40,000hrs).

The goal of the current study is to understand the creep behaviors of Alloy 282, to develop a creep model able to capture the experimental observations, and to predict the longer time behaviors. The model development requires first a sufficient understanding of the possible deformation mechanisms, which are known to be closely related to the microstructural features of the alloy.

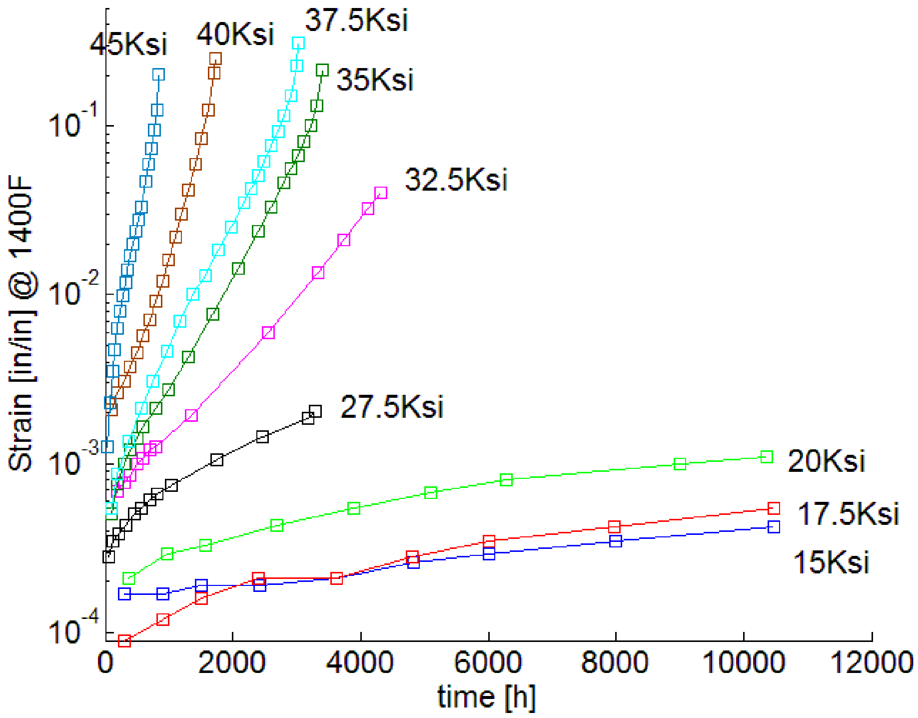

Figure 74: Creep curves of peak-aged Alloy 282 at 1400˚F. Note secondary creep and clear steady-state at stresses of 15, 17.5, 20Ksi, and pronounced tertiary creep at stresses above 35Ksi.

5.2. Observations of creep deformation mechanisms in Alloy 282

It has been generally accepted that the inelastic deformation in FCC metals is generated by fast traveling of dislocations through the crystalline structure at a stress above yield point. However, when dislocations glide, they may encounter a series of obstacles that slow down their motion. The time spent on the attempts for overcoming these obstacles may be significantly higher than the traveling time, and thus dictate the deformation rate observed at a macroscopic scale. Often, we assume that the traveling time is negligible compared with the time at the obstacles. In a homogeneous microstructure, the obstacles can be stationary dislocations (or “forest dislocations” that do not experience enough driving force to move). In precipitate-strengthened alloys such as Alloy 282, coherent γ’ precipitates act as major pinning obstacles. Dislocations may bypass the precipitates by either cross slip and climb [16,30,31], bowing around the precipitates (Orowan looping), or cutting through the precipitates [32]. Figure 75 summarizes the historical observations of one or two dominant mechanisms in Alloy 282 in the stress regime of current interest:

1. At low stresses (15-20Ksi), moderate strains (0.1-0.3%), and low strain rates (10^{-7}/s), Orowan looping and stress-assisted dislocation climb were frequently observed

2. At high stresses (30-40Ksi), the strain increased rapidly with a strain rate as high as 10^{-2} -10^{-3}/s. Precipitate shearing was typically observed at high strain levels (18-25%).
3. At intermediate stresses (20-30Ksi), both dislocations climb and precipitate shearing mechanisms were observed. The upper right corner of Figure 75 shows images of the two mechanisms identified at 23% creep strain, 27.5Ksi and 1450˚F.

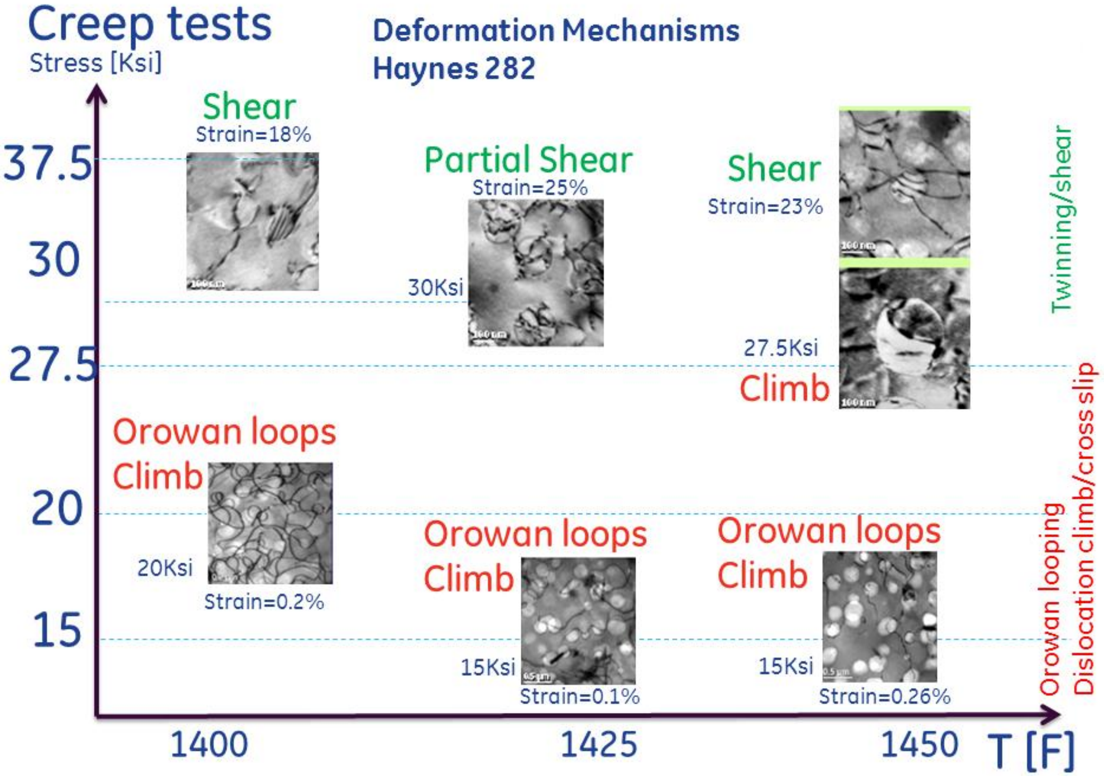

Figure 75: Deformation modes observed in Alloy 282 creep specimens. Courtesy of Mallik Karadge.

The above observations capture dislocation creep mechanisms in Alloy 282 over a range of stress above 15Ksi and creep strain above 0.1%. However, consider the lower 5Ksi stress requirement for AUSC turbine rotor materials, diffusion creep may also play an important role [33]. In order to infer whether a mechanism transition occurs, the macroscopic data are plotted in terms of Log (minimum strain rate) versus Log (stress) in Figure 76, at three temperature levels: 1400˚F, 1425˚F, 1450˚F. At each temperature the data seem to follow a bilinear trend. The change in the slope may suggest a shift of creep mechanism between dislocation creep and diffusion creep.

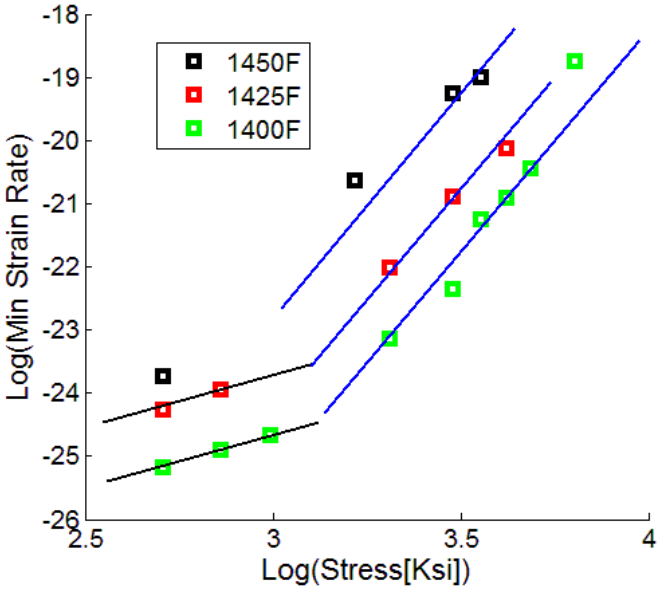

Figure 76: Minimum strain rate vs. stress from Alloy 282 creep data. Symbols are experimental data. Lines highlight the bilinear trend.

5.3. Creep model formulation

In order to capture both diffusion and dislocation mechanisms in a unified creep model we consider the total creep strain, ε^{creep}, as a superposition of dislocation component, ε^{disloc}, and diffusion component, $\varepsilon^{diffusion}$:

$$\varepsilon^{creep} = \varepsilon^{disloc} + \varepsilon^{diffusion} \tag{5.1}$$

5.3.1. Dislocation component

For dislocation gliding and climb-bypassing precipitates, Dyson et al[16,30,31] proposed a hyperbolic sine dependence of the strain rate, $\dot{\varepsilon}^{disloc}$, on the net stress required to advance a dislocation:

$$\dot{\varepsilon}^{disloc} = \rho A\, f(1-f)\left(\sqrt{\frac{\pi}{4f}}-1\right)\sinh\left(C\,\frac{\sigma_{eff}-\sigma_B-\sigma_o}{MkT}\,b^2\lambda\right)\, H(\sigma_{eff}-\sigma_B-\sigma_o) \tag{5.2}$$

where H is the Heaviside function $H(x) = \begin{cases} 1 & \text{if } x \geq 0 \\ 0 & \text{if } x < 0 \end{cases}$

Where A and C are constant parameters, ρ is the density of dislocations, f is the volume fraction of precipitates, M is Taylor factor, k is Boltzmann constant, T is the absolute temperature, b is the Burgers vector, and λ is the average spacing between precipitates. Since each gliding dislocation encounters a series of obstacles, the net stress that drives the dislocation motion is taken as the local effective stress, σ_{eff}, subtracted by a penalty due to the interaction with other dislocations (forest dislocation strengthening term), σ_o, and a penalty due to the interaction with precipitates (back stress), σ_B. The effective stress, σ_{eff}, is further discussed in Section 5.3.3.

Using the Taylor law, the dislocation strengthening term is proportional to the square root of dislocation density ρ [34]:

$$\sigma_o = 0.25MG(T)b\sqrt{\rho} \tag{5.3}$$

where $G = E(T)/2(1+\nu)$ is the shear modulus, and ν the Poisson's ratio.

We consider that dislocation creep proceeds via either climb-bypass or shearing precipitates. For shearing precipitates with weakly coupled dislocation pairs, the back stress can be calculated as [32]:

$$\sigma_{shear} = \frac{\gamma_{APB}}{2b}\left[\left(\frac{12\gamma_{APB}fr}{\pi G b^2}\right)^{1/2} - f\right] \tag{5.4}$$

Where γ_{APB} is the anti-phase boundary energy, r is the average size of precipitates. The hypothesis of the weakly coupled dislocations is made on the consideration that the space between the precipitates is large compared with their radius (about three times larger in Alloy 282). For strongly coupled dislocations σ_{shear} is expected to be slightly higher [32]. The back stress for dislocation climb-bypass, on the other hand, is calculated as[16]:

$$\sigma_{climb} = \frac{2f}{1+2f}\sigma_{eff}\left[1 - \exp\left(-\frac{1+2f}{2(1-f)}E\frac{\varepsilon^{disloc}}{\sigma_{eff}}\right)\right] \tag{5.5}$$

Where σ_{eff} is the effective stress, as described earlier and E is the elastic modulus.

The observations in Figure 75 indicate that the climb-bypass mechanism occurs at intermediate stress levels (20-40Ksi), and that the shear mechanism is active at higher stresses (> 40Ksi) or at high strains. For simplicity, we consider the creep deformation is driven predominantly by the weaker mechanism, either shearing or climb-bypass at a given time, although there could be a transitional regime where both are active. The back stress is thus taken as:

$$\sigma_B = \min(\sigma_{shear}, \sigma_{climb}) \tag{5.6}$$

A few historical TEM measurements provide an estimate of dislocation density in Alloy 282: $2\times 10^{13}/m^2$ at 0.2% creep strain under 27.5Ksi stress, $4\times 10^{13}/m^2$ at 0.2% strain and 32.5Ksi, and $1.4\times 10^{14}/m^2$ at 4% strain and 32.5Ksi. Figure 77 shows TEM images of dislocation structures in Alloy 282 creep samples at 0.2%

and 4% strain. We consider that the dislocation density has a linear dependence on creep strain before a constant saturation value is reached at a certain critical strain, ε^{crit}. A linear dependence of ε^{crit} on stress is fit to the above TEM data.

$$\rho = \begin{cases} \rho_f \varepsilon / \varepsilon^{crit} & \text{if } \varepsilon \leq \varepsilon^{crit}(\sigma_{applied}, T) \\ \rho_f & \text{if } \varepsilon > \varepsilon^{crit}(\sigma_{applied}, T) \end{cases} \tag{5.7}$$

with $\varepsilon^{crit} = B\ \sigma_{applied}[MPa]$.

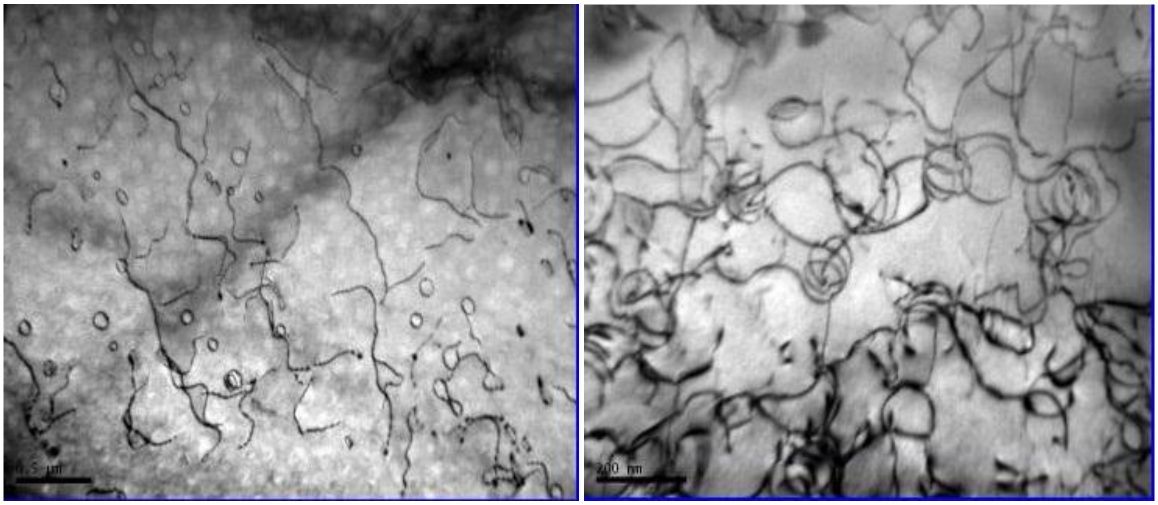

(a) (b)

Figure 77: Dislocation structures at 1400˚F at (a) 0.2% and (b) 4% creep strain. Courtesy of Mallik Karadge.

Equations (5.1)-(5.5) contain two parameters that require special attention: precipitate size and inter-space. The phase field simulations (see Sections 4.1.3 and 4.1.4) showed that considerable coarsening of γ' precipitates could occur during long-term exposure to temperatures between 1300˚F and 1500˚F (Figure 33). Because creep also implies a long time exposure to a given temperature, an accurate evolution of the precipitate size needed to be incorporated. This was accomplished by using directly the validated phase field results for the γ' size evolution with time in the creep model. In addition, the linear relationship between the inter-particle spacing, λ, and the average precipitate size (see Section 4.2) was utilized

5.3.2. Diffusion component

According to Cocks and Ashby[35,36] the diffusion creep strain rate $\dot{\varepsilon}^{diffusion}$ can be contributed by multiple sources: lattice diffusion $\dot{\varepsilon}^{lattice\_diff}$, grain boundary diffusion $\dot{\varepsilon}^{boundary\_diff}$, surface diffusion at the grain boundary cavities $\dot{\varepsilon}^{cavity\_surface\_diff}$, and grain boundary diffusion near cavities $\dot{\varepsilon}^{cavity\_boundary\_diff}$:

$$\dot{\varepsilon}^{diffusion} = \dot{\varepsilon}^{lattice\_diff} + \dot{\varepsilon}^{boundary\_diff} + \dot{\varepsilon}^{cavity\_boundary\_diff} + \dot{\varepsilon}^{cavity\_surface\_diff} \quad (5.8)$$

The grain boundary and lattice diffusion components, which do not contribute to the cavity growth, can be written as:

$$\dot{\varepsilon}^{boundary\_diff} = 3\pi\xi \left(\frac{l}{d}\right)^3 \sigma_{applied}(1 + \varepsilon^{creep}) \quad (5.9)$$
$$\dot{\varepsilon}^{lattice\_diff} = \xi\beta\sigma_{applied}(1 + \varepsilon^{creep}) \quad (5.10)$$

where $\beta = \frac{3D_V}{D_B\delta_B}\frac{l^3}{d^2}$.

Considering the self-diffusivity of Ni: $D_V = 9.2 \times 10^{-5} \exp\left(-\frac{287kJ/mol}{RT}\right) m^2/s$ for bulk diffusion and $D_B\delta_B = 7.7 \times 10^{-14} \exp\left(-\frac{162kJ/mol}{RT}\right) m^3/s$ for grain boundary diffusion, reported by Divinski et. al[37], and the ratio $l/d \sim 0.1$, $d = 150\mu m$, we estimated the coefficient $\beta \sim 7.3 \times 10^{-4}$.

As discussed by Cocks and Ashby[36], the growth of cavities through diffusion is associated also with the change in the overall strain rate. The strain rate contribution due to cavities boundary diffusion is expressed in terms of the applied stress $\sigma_{applied}$, grain size *d*, and a damage variable $\varpi_{boundary\_diff}$ accounting for the cavities change due to diffusion into the neighboring grains:

$$\dot{\varepsilon}^{cavity\_boundary\_diff} = \xi \frac{l}{d} \frac{\sigma_{applied}}{\ln(1/\varpi_{boundary\_diff})} \quad (5.11)$$

The strain rate contribution due to cavities surface diffusion is also expressed in terms of the applied stress and a damage variable $\varpi_{surface\_diff}$ associated with cavities change due to diffusion at the cavities surface:

$$\dot{\varepsilon}^{cavity\_surface\_diff} = \xi\alpha \frac{\sqrt{\varpi_{surface\_diff}}\,\sigma_{applied}{}^2}{(1-\varpi_{surface\_diff})^3} \quad (5.12)$$

The evolution laws for $\varpi_{boundary\_diff}$ and $\varpi_{surface\_diff}$ are described in Section 5.3.3.

In equations (5.11) and (5.12) the parameter ξ is a fitting constant and α is a scaling parameter that depends on the grain size *d*, surface energy of the material γ, surface diffusion coefficient $D_S\delta_S$, boundary diffusion coefficient $D_B\delta_B$, and the average distance between two neighboring voids *l*:

$$\alpha = \frac{D_S\delta_S}{D_B\delta_B}\frac{1}{\sqrt{2}}\frac{l^2}{d\gamma} \quad (5.13)$$

Based on the reported diffusivities values for various materials[37] we consider $D_S\delta_S$ on the same order of magnitude as $D_B\delta_B$. Also a value of 2J/m^2 for the surface energy and the earlier considered ratio $l/d \sim 0.1$, $d = 150\mu m$ lead to an estimated value $\alpha \sim 0.5 MPa^{-1}$.

5.3.3. Damage variable evolution and effective stress

Although the master equation (5.2) is able to describe a nonlinear increase of creep strain toward later times, tertiary creep and especially the associated grain boundary cavity growth are not well accounted for. The nucleation and growth of these voids at grain boundaries are related to a macroscopic change of the effective cross-sectional area of the creep sample, A.

Denoting by A_0 the initial cross-sectional area and by ϖ the factor related to its change: $\varpi = 1 - A/A_0$ (i.e., the area fraction of the cavities), the effective stress in the gage area of a creep specimen can be written as:

$$\sigma_{eff} = \frac{\sigma_{applied}}{(1-\varpi\,)}(1+\varepsilon^{creep}) \tag{5.14}$$

Following [33,35,36] we assume that the cavities can grow though deformation of the neighboring grains ϖ_{disloc} or diffusion into the neighboring grains ϖ_{diff}

$$\varpi = \varpi_{diff} + \varpi_{disloc} \tag{5.15}$$

We make the simplifying assumption that the area of each cavity formed during deformation can be linearly decomposed into an area formed due to plasticity of the neighboring grain and an area formed due to diffusion (along the cavity surface or grain boundaries). Thus, the total cavities area fraction ϖ has a diffusional component ϖ_{diff} and a plastic component ϖ_{disloc}. The cavities are considered spherically and uniformly distributed at the grain boundaries. Schematics of possible cavity shapes formed due to various mechanisms were included in Figure 78.

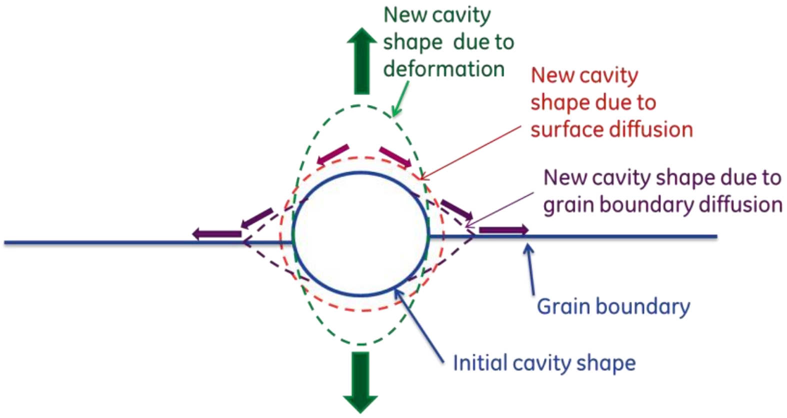

Figure 78: Cavity changes due to grain deformations and diffusion.

According to[33], the combined effects of diffusion and deformation become relevant at temperatures above half melting temperature (>1200˚F) and at stress levels beyond 10^{-3}G (i.e. 7-9Ksi at 1400 -1450˚F) for Alloy 282.

A simple linear dependence on strain is used for the dislocation component [38,39]:

$$\dot{\varpi}_{disloc} = D\dot{\varepsilon}^{disloc} \tag{5.16}$$

The diffusion damage variable couples the boundary diffusion component $\varpi_{boundary\_diff}$ and cavity surface diffusion component $\varpi_{surface\_diff}$:

$$\varpi_{diff} = \varpi_{boundary\_diff} + \varpi_{surface\_diff} \tag{5.17}$$

As proposed by Cocks and Ashby[36] the boundary diffusion damage variable evolves as:

$$\dot{\varpi}_{boundary\_diff} = \frac{\xi}{2}\frac{\sigma_{applied}(1+\varepsilon^{creep})}{\sqrt{\varpi_{boundary\_diff}}\ln(1/\varpi_{boundary\_diff})} \tag{5.18}$$

while the surface diffusion damage variable evolves as:

$$\dot{\varpi}_{surface\_diff} = \frac{\xi\alpha}{4}\frac{d}{\gamma}\frac{\sqrt{\varpi_{surface\_diff}}\left[\sigma_{applied}(1+\varepsilon^{creep})\right]^3}{(1-\varpi_{surface\_diff})^3} \tag{5.19}$$

Equations (5.1)-(5.19) constitute the proposed creep model formulation for capturing the main creep mechanisms of diffusion, dislocation climb-bypass, and to some extend particle shearing. These equations contain 5 parameters that have been fit to the Alloy 282 creep data at 15, 27.5, and 32.5Ksi, at 1400˚F and 1450˚F. The model parameters in Equations (5.1)-(5.19), determined by microstructural characterization, thermodynamic calculations, phase field simulations, and parameter fitting, are summarized in Table 6.

Table 6: A summary of the parameters in the creep model

Parameter name	Symbol	Value	Source
Activation volume	Ω	$1.2 \times 10^{-29} m^3$	Thermodynamic calculations
Burgers vector	b	2.54Å	Ni lattice parameter
Taylor Factor	M	3.07	Typical for FCC metal
Average grain size	d	$150\mu m$	Characterization
Void diameter/grain diameter ratio	l/d	0.1	Estimated
Lattice diffusion parameter	β	7×10^{-4}	Calculated from $\beta = \frac{3D_V}{D_B\delta_B}\frac{l^3}{d^2}$.
Self-diffusion coefficient of Ni	D_V	$9.2 \times 10^{-5} \exp\left(-\frac{287}{RT}\frac{kJ}{mol}\right)\ m^2/s$	Ref.[37]

Bulk diffusion parameter	$D_B\delta_B$	$7.7 \times 10^{-14} \exp\left(-\frac{162}{RT}\frac{kJ}{mol}\right)$ m^3/s	Ref.[37]
Surface Energy	γ	2 J/m^2	Estimated
Anti-phase boundary energy	γ_{APB}	0.15 J/m^2	Estimated
Boundary diffusion parameter	α	$0.5MPa^{-1}$	Calculated from $\alpha = \frac{D_S\delta_S}{D_B\delta_B}\frac{1}{\sqrt{2}}\frac{l^2}{d\gamma}$
Precipitates volume fraction	f	a=(T-1033.2)/21.96 f=0.0035714a^2 - 0.011068a + 0.18774 T - temperature in K	Thermodynamic calculation
Precipitate mean radius	r	Precipitation model predictions	Precipitation model predictions
Inter-precipitates spacing	λ	λ~3r	Phase field simulation
Elastic Modulus	E	26.859T^2 - 57404T + 3.0796e+07 [MPa] T temeperature [K]	Tensile test data
Poisson's ratio	ν	0.3	Estimated
Initial and saturation dislocation densities	ρ_f	$8 \times 10^{13}/m^2$	Microstructure observations
Creep strain rate coefficient	A	8.8E-14 1/s	Fitted
Dislocation density parameter	B	1e-5	Fitted
Creep strain rate parameter	C	0.25	Fitted
Damage evolution parameter	D	0.02	Fitted
Creep diffusion parameter	ξ	$5 \times 10^{-12}s^{-1}MPa^{-1}$	Fitted

5.4. Model predictions and sensitivity to microstructure

5.4.1. Alloy 282 creep predictions and evaluation

The model predictions are presented in Figure 79-Figure 82. Both creep strain and strain rate are compared with experimental data. Visually we can observe a good agreement. To further quantify the agreement of the model, we use the following Z – parameter [40,41]:

$$Z = 10^{2.5\mathrm{Std}\left[\log\left(\varepsilon_{predicted}\right)-\log\left(\varepsilon_{actual}\right)\right]} \quad (5.20)$$

which accounts for the standard deviation of the difference between the predicted strain and the experimental strain in logarithmic scale. In such a test, a model is considered ideal if Z is smaller than 2, acceptable if Z is between 2 and 4, and unacceptable if Z is higher than 4. Table 7 summarizes the calculated Z values for data points from 1400˚F (second column), 1425˚F (third column), 1450˚F (forth column) or combined (last column). The values were calculated at several strain levels. The Z-parameter takes small values (<2) for strains between 0.3 and 1%, and slightly higher values (but still less than 3) for the rest of creep strains.

Table 7: Error estimation (Z values) for the creep model at given creep strain.

Creep strain	Z 1400°F	Z 1425°F	Z 1450°F	Z cumulated
0.1%	2.27	1.60	1.20	2.23
0.3%	2.05	1.56	1.01	1.86
0.5%	1.77	1.62	1.02	1.77
0.7%	1.58	1.58	1.03	1.79
1%	1.47	1.57	1.07	1.91
1.5%	1.75	1.53	1.00	2.15
3%	1.88	1.51	1.01	2.32

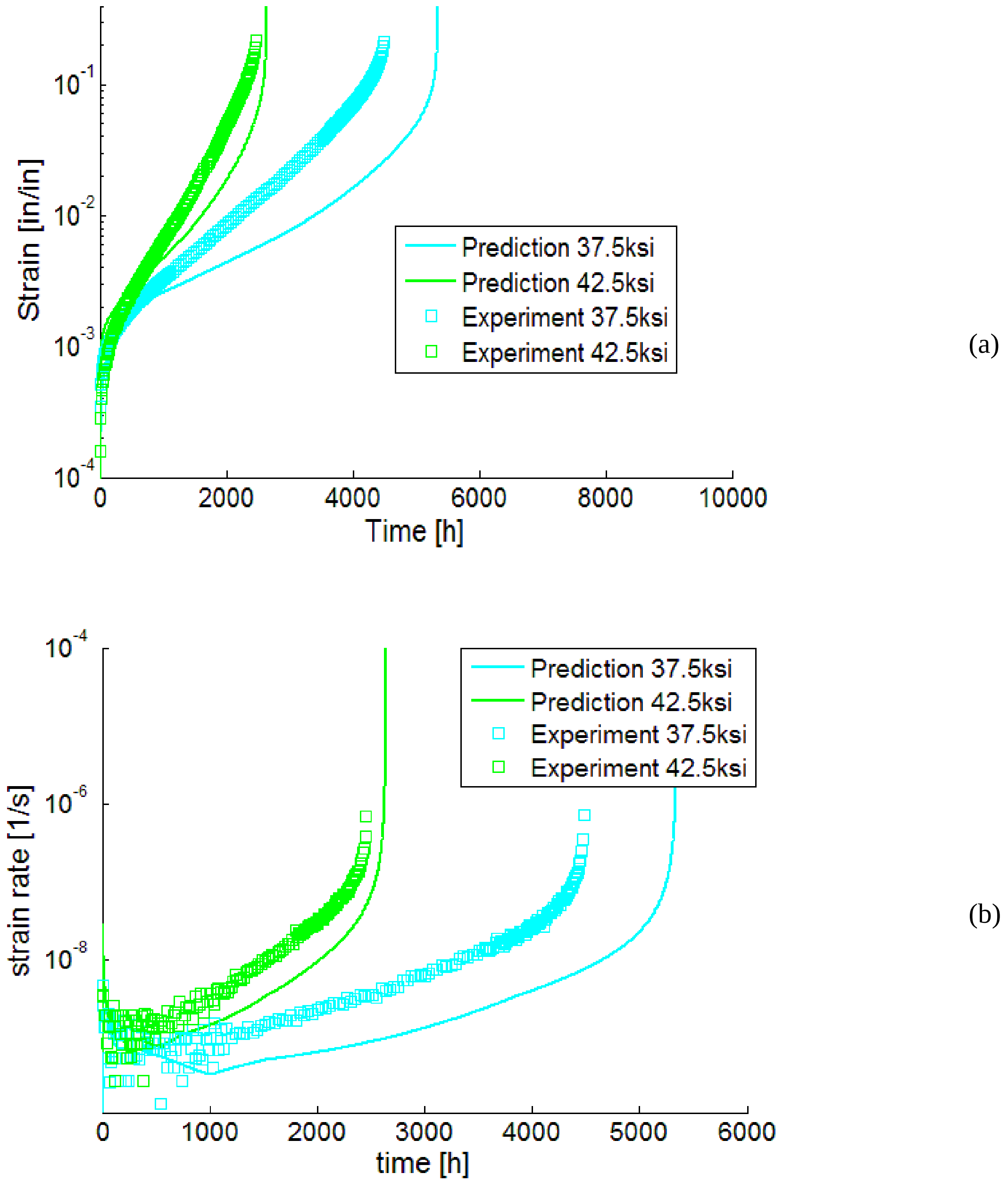

Figure 79: Alloy 282 creep experimental data (symbols) and model prediction (curves) at 1375˚F: (a) creep strain, (b) creep strain rate.

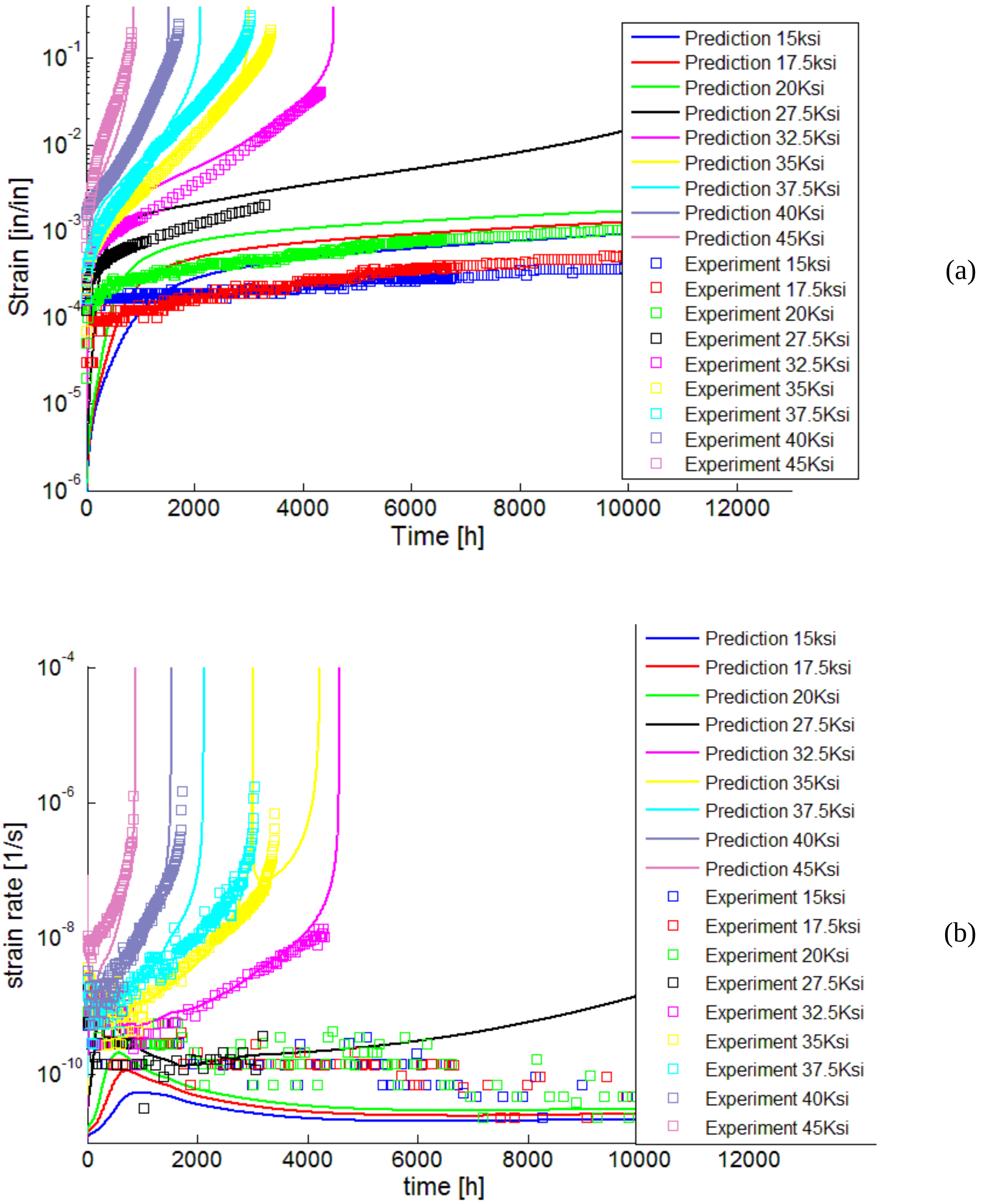

Figure 80: Alloy 282 creep experimental data (symbols) and model prediction (curves) at 1400˚F: (a) creep strain, (b) creep strain rate.

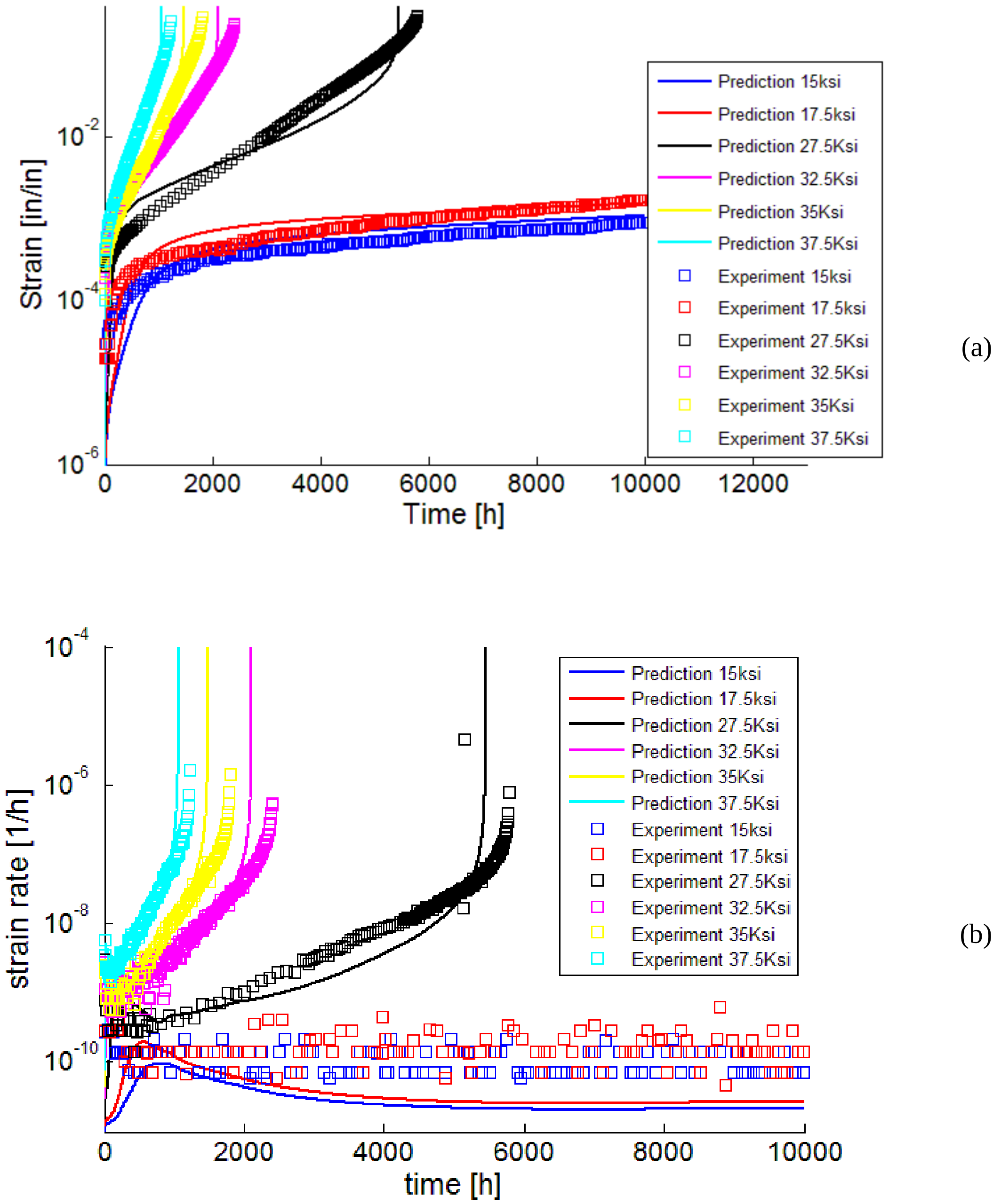

Figure 81: Alloy 282 creep experimental data (symbols) and model prediction (curves) at 1425˚F: (a) creep strain, (b) creep strain rate.

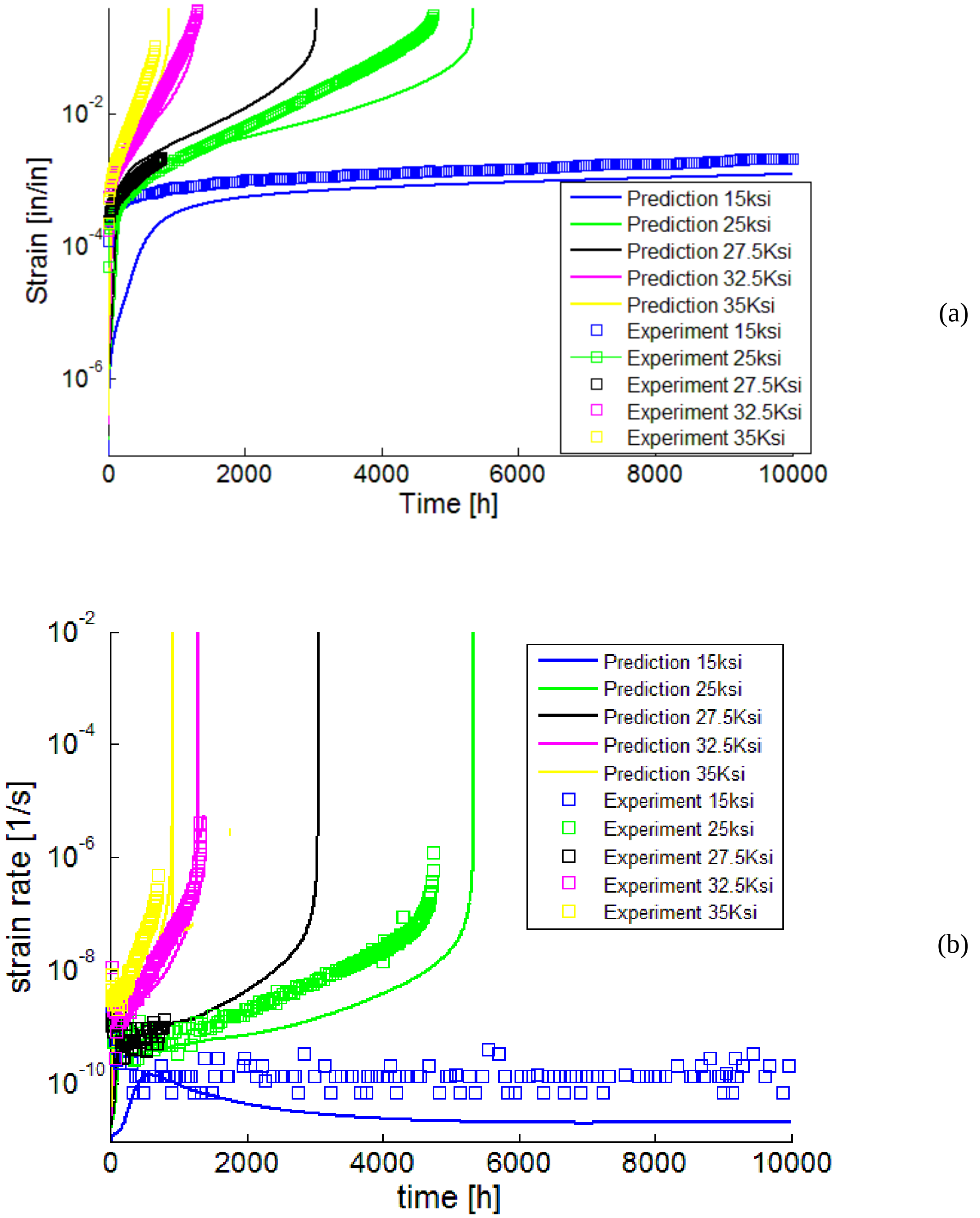

Figure 82: Alloy 282 creep experimental data (symbols) and model prediction (curves) at 1450˚F: (a) creep strain, (b) creep strain rate.

A comparison is made in Figure 83 between the predictions by the creep model and that by a linear extrapolation from the secondary creep regime. We calculated the time at which the creep strain reached a selected value (20%). As expected, the time to 20% strain predicted by the creep model is shorter over the entire stress range, by up to one order of magnitude. This means the linear extrapolation has over-predicted the time to reach 20% strain. In consequence, the method based on linear extrapolation from secondary creep regime data might also lead to over-predictions of creep rupture times.

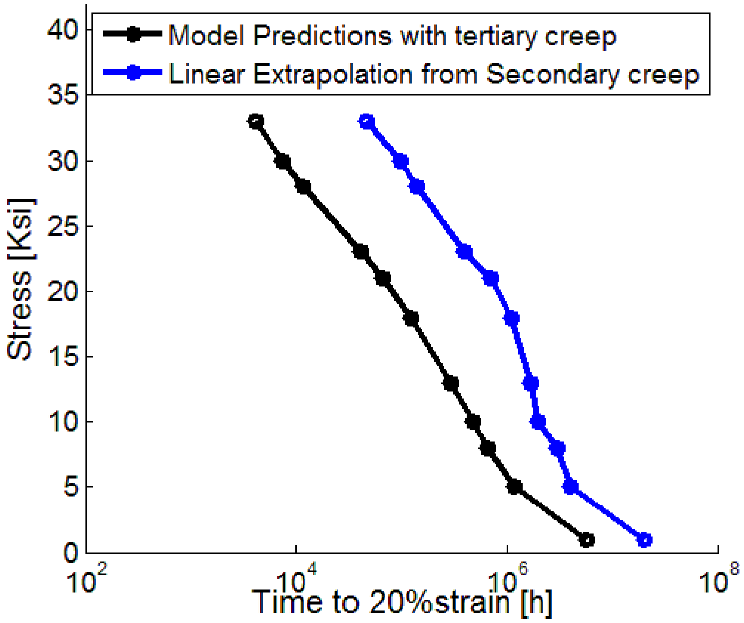

Figure 83: Time to 20% creep strain predicted by the creep model and by linear extrapolation of the secondary creep regime.

Figure 84 presents the typical evolution of the damage variable during the accumulation of creep strain. We see that, similar to creep strain accumulation, the damage variable experiences a fast increase right before reaching the rupture time. One could thus estimate the rupture time as the particular moment when this rapid change occurs (either in the strain evolution or in the damage variable evolution). However, for a better physical picture, the rupture time is estimated here as the time at which the effective stress reaches the ultimate tensile strength (UTS) at the test temperature. This can be expressed as the time t_c for which:

$$1 - \varpi(t_c) = \frac{\sigma_{applied}}{\sigma_{UTS}}[1 + \varepsilon(t_c)] \tag{5.21}$$

The ultimate stress values σ_{UTS} used in the model are presented in Figure 4.

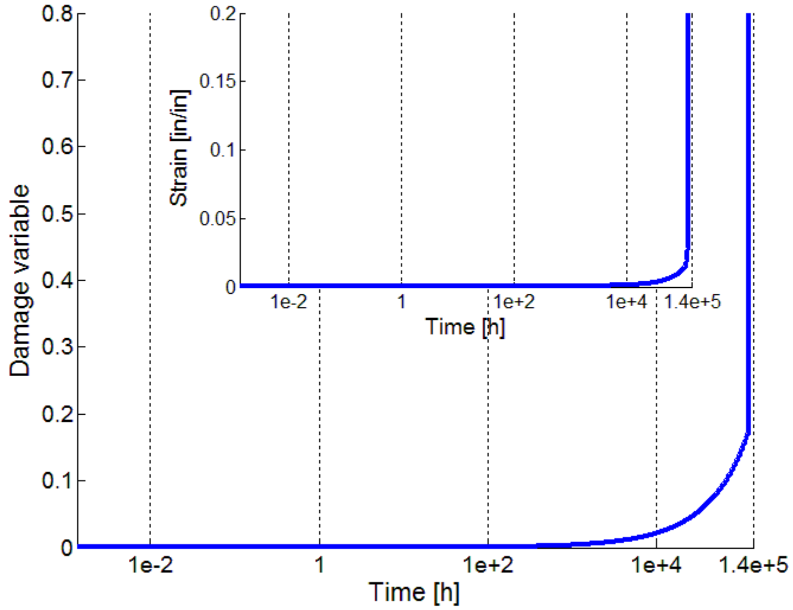

Figure 84: Damage variable evolution at 1450˚F, 15ksi. The inset shows the creep strain evolution.

Figure 85 compares the predicted and measured creep strain at rupture. Note the rupture strain is dependent on the applied stress and temperature, as damage evolution and creep mechanisms may change. It is shown that the rupture strain tends to decrease at lower temperature and higher stress. Thus, a creep rupture criterion based on a critical strain value does not appear to be ideal for capturing the experimental observations in a general sense.

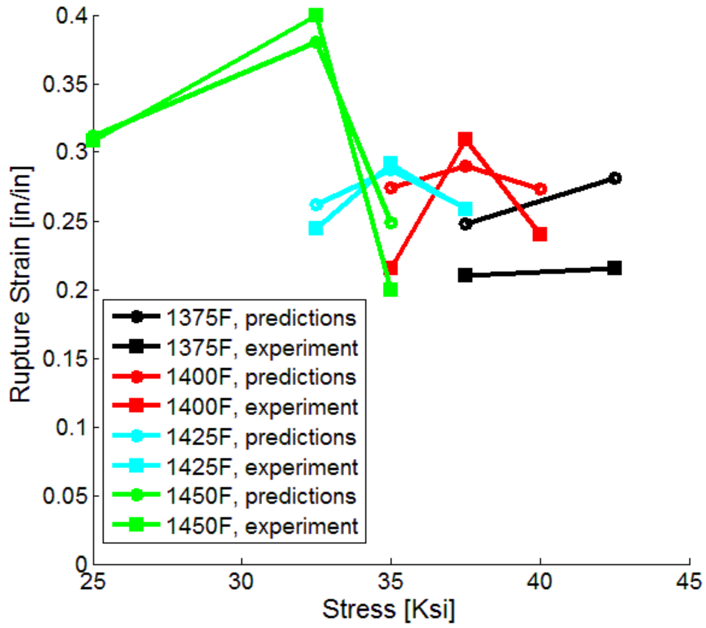

Figure 85: Comparison of rupture strains predicted by the model and experimental data.

The variation of the stress with the Larson-Miller parameter (LMP) calculated at 1400˚F was compared with experimental data in Figure 86. For the comparison, the experimental data in Ref [42] were digitized and tabulated along with model predictions in Table 8. An additional set of experimental data are extracted from the GE historical data presented in Figure 79 - Figure 82. Note some of these curves were completed until failure, while others were interrupted before rupture. The rupture times for those complete-to-rupture conditions are compared with the model predictions in Table 9. The blue line is the prediction by the entire model as described by Equations (5.1)-(5.19). In order to understand the contribution of individual mechanisms, predictions were all made by activating only selected components: (i) diffusion creep only; (ii) precipitate shearing and dislocations-dislocations interactions; (iii) dislocation climb-bypass and dislocations-dislocations interactions. It was observed that the low stress regime (<15Ksi) was dominated by diffusion creep, the intermediate stress regime (15-50ksi) was dominated by dislocation climb-bypass, while the high stress regime (>50Ksi) was mainly dominated by precipitate shearing and dislocation-dislocation interactions. The LMP plot of experimental creep data[42] is compared with the model predictions at two temperatures: 1400˚F and 1450˚F in Figure 87. The two predicted curves overlapped in the dislocation creep regime but they appeared to dissociate in the low-stress regime where diffusion creep dominated. Note the non-overlapped curves would appear as data 'scatter' in a conventional LMP plot, where temperature is not differentiated.

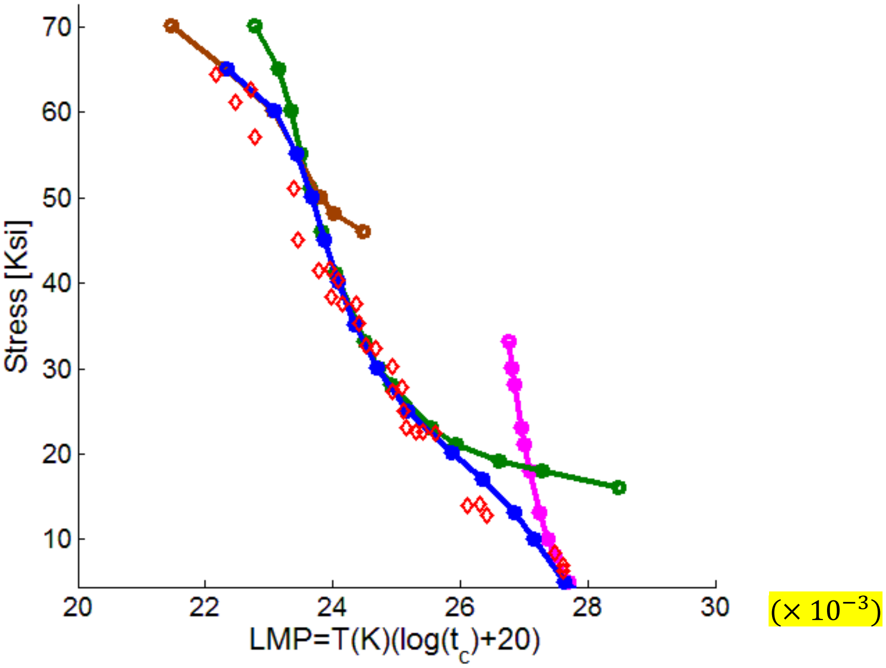

Figure 86: Comparison of Larson Miller plot of experimental creep data (diamond symbols) and model predictions with selected creep mechanisms: i) diffusion creep only (magenta line); ii) dislocation creep via precipitate shearing (brown line); iii) dislocation creep via climb-bypass (green line); iv) combined diffusion and dislocation creep (blue line).

Table 8: Comparison between predicted and experimental Larson Miller parameter (LMP)

Stress, ksi	$LMP \times 10^{-3}$		
	Experiment (Ref [42])	Predicted (1400˚F)	Predicted (1450˚F)
3.5	28.9	27.2	27.9
6.2	27.6	26.8	27.5
6.8	27.6	26.8	27.5
8.4	27.5	26.6	27.3
12.7	26.4	26.3	26.9
14.1	26.3	26.2	26.7
13.9	26.1	26.2	26.7
22.5	25.3	25.5	25.5
23.0	25.1	25.4	25.4
25.0	25.1	25.2	25.2
27.7	25.1	24.9	24.9
30.1	24.9	24.7	24.7
32.2	24.7	24.5	24.5
32.6	24.5	24.4	24.5
35.1	24.4	24.3	24.3
37.5	24.1	24.1	24.2
38.3	24.0	24.1	24.2
40.2	24.1	23.9	24.1
41.4	23.8	23.9	24.0
44.9	23.4	23.7	23.9

Table 9: Comparison between predicted and experimental time to rupture

Stress, ksi	Time to rupture (hour)					
	Predicted at 1400˚F	Measured at 1400˚F	Predicted at 1425˚F	Measured at 1425˚F	Predicted at 1450˚F	Measured at 1450˚F
45	877	836	460	-	310	-
40	1526	1700	470	-	502	-
37.5	2186	3029	1062	1223	672	-
35	3232	3250	1480	1800	900	680
32.5	4604	-	2100	2377	1304	1260
27.5	13290	-	5450	5700	3174	-
25	24694	-	11692	-	5335	4600

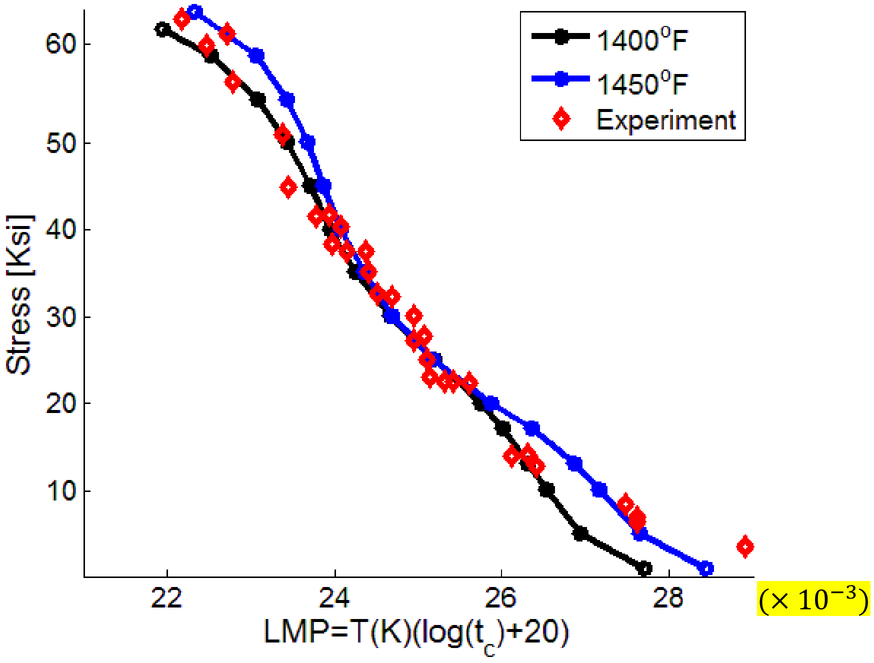

Figure 87: Larson Miller plot of experimental creep data vs. model predictions at 1400˚F and 1450˚F.

5.4.2. Dependence of creep on precipitate microstructure

Microstructures are represented in the creep model by γ’ precipitate size *r* (Equation (5.4)), inter-particle spacing λ (Equation (5.2)), volume fraction *f* (Equations (5.2), (5.4), (5.5)), and grain size *d* (Equations (5.9)-(5.19)). While the grain size and the γ’ volume fraction are considered to be constant in time at a given temperature, the precipitate size and the inter-particle space vary with both temperature and exposure time. In order to understand how the precipitate evolution affects the creep properties, we compare in Figure 88 the predicted creep to rupture at 1450˚F with a second prediction case, in which γ’ evolution is frozen after first 500 hours. The inset shows the change of the mean γ’ size for the two cases. A noticeably longer rupture time was predicted for the frozen microstructure at intermediate stresses (4-35Ksi). It can be expected that continuous coarsening of γ’ precipitate leads to an increase in inter-particle spacing with time, so that the γ’ pinning effects on mobile dislocations are weakened, and thus creep strain rate increases. In the low stress regime (<4Ksi), however, the microstructural changes did not show to affect creep evolution since the dominating diffusion effects were not sensitive to γ’ size. In the high stress regime (>35Ksi) creep evolutions were also merged where the rupture time was relatively short, compared with the time for microstructural changes.

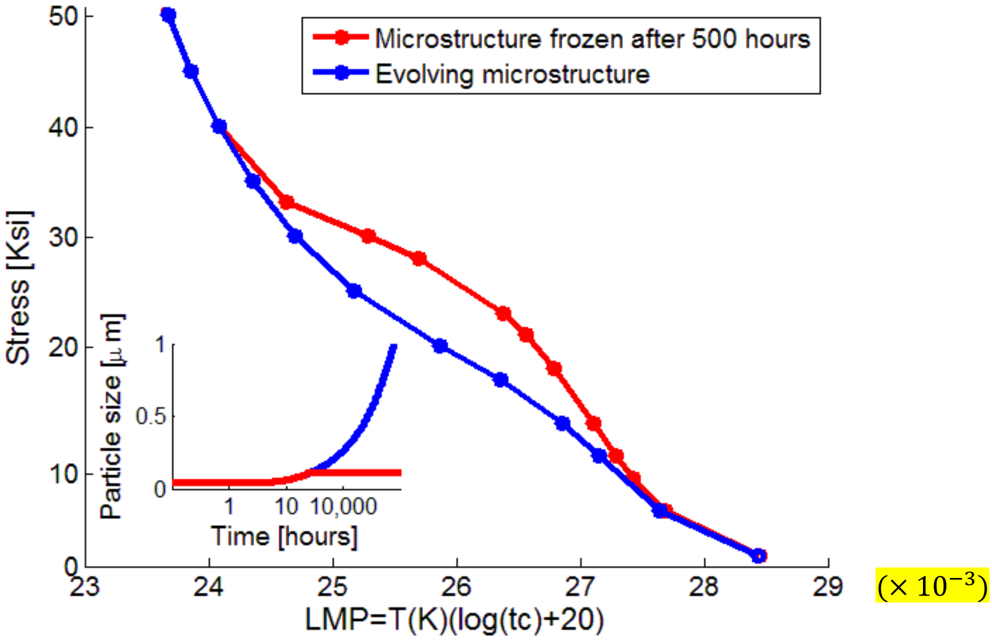

Figure 88: Larson Miller plot of the predicted creep at 1450˚F with (i) continuous microstructure coarsening until rupture, (ii) microstructure frozen after 500 hours. The inset shows the corresponding mean precipitate size for the two cases.

5.5. Summary

A continuum damage based model was developed for predicting creep behaviors of Alloy 282 for a range of temperature and stress conditions (1375-1450˚F, 15-45Ksi) relevant to the A-USC turbine rotor operation. The model has been calibrated on a small set of creep strain versus time experimental data at temperatures of 1400˚F and 1450˚F, and stresses of 15Ksi, 27.5Ksi, and 32.5Ksi. The main creep mechanisms considered were diffusion creep at low to intermediate stress, and dislocation climb-bypass and γ' shearing at intermediate to high stresses. The model was validated against experiment at temperatures of 1375˚F, 1400˚F, 1425˚F, 1450˚F, and various stresses between 15Ksi and 45Ksi. The γ' shearing mechanism was introduced only through a correction of the back stress needed for dislocations to overcome the precipitates. The model may require additional modifications in the regime where the particle shearing mechanism is more pronounced (e.g., at high stresses). For this reason we recommend limiting the application of the model to stresses lower than 50-60Ksi.

Task 6: Multi scale crack growth modeling considering oxidation, visco-plasticity and fatigue

6.1. Overall approach

The effort described herein addresses modeling of fatigue crack growth at two targeted temperatures, 1200˚F and 1400˚F, in Alloy 282. Since different crack growth mechanisms are expected, various tests are performed to calibrate and validate constitutive material models, crack growth rate models, and to assess contribution of the environment (oxidation) to the crack propagation process. This task made use of the measurement data (Task 2), models (Task 5) and conclusions generated in other tasks to perform additional testing and perform simulations to predict crack growth under various conditions. The overall procedure is shown in Figure 89 and uses a modeling framework proposed by Pommier [43-46].

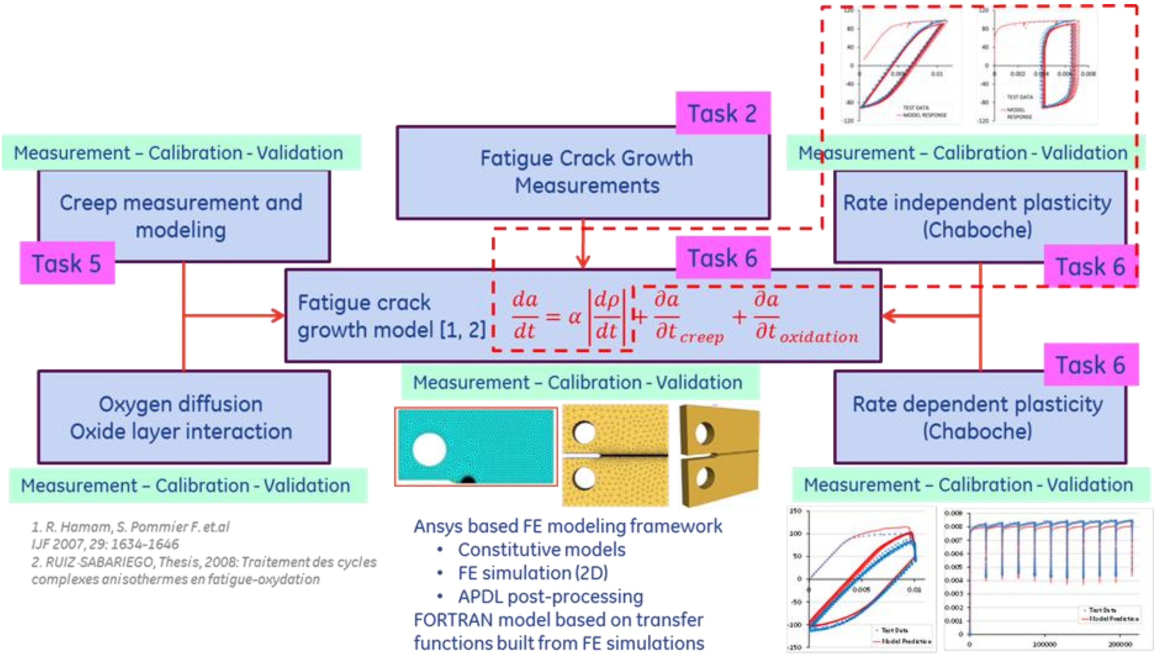

Figure 89: Overall modeling effort and interactions with other tasks.

The crack growth model shown in Figure 89 contains the following terms:

da/dt	Total crack growth rate
$\vert d\rho/dt \vert$	Rate of plastic flow intensity factor [43-46]
α	Calibration parameter
$(\partial a/\partial t)_{creep}$	Crack growth rate due to creep deformation
$(\partial a/\partial t)_{oxidation}$	Crack growth rate due to oxidation

The first aspect that had to be captured was the relationship between crack tip plasticity (rate independent response) and fatigue crack growth (da/dt=α*|dρ/dt|). The procedure is shown in Figure 90 and used round bar specimens for testing to capture bulk plasticity, rate independent constitutive modeling, compact tension specimen testing and finite element modeling to predict crack tip plasticity history to further calibrate (find α parameter) and validate the crack growth rate law against various measurement data.

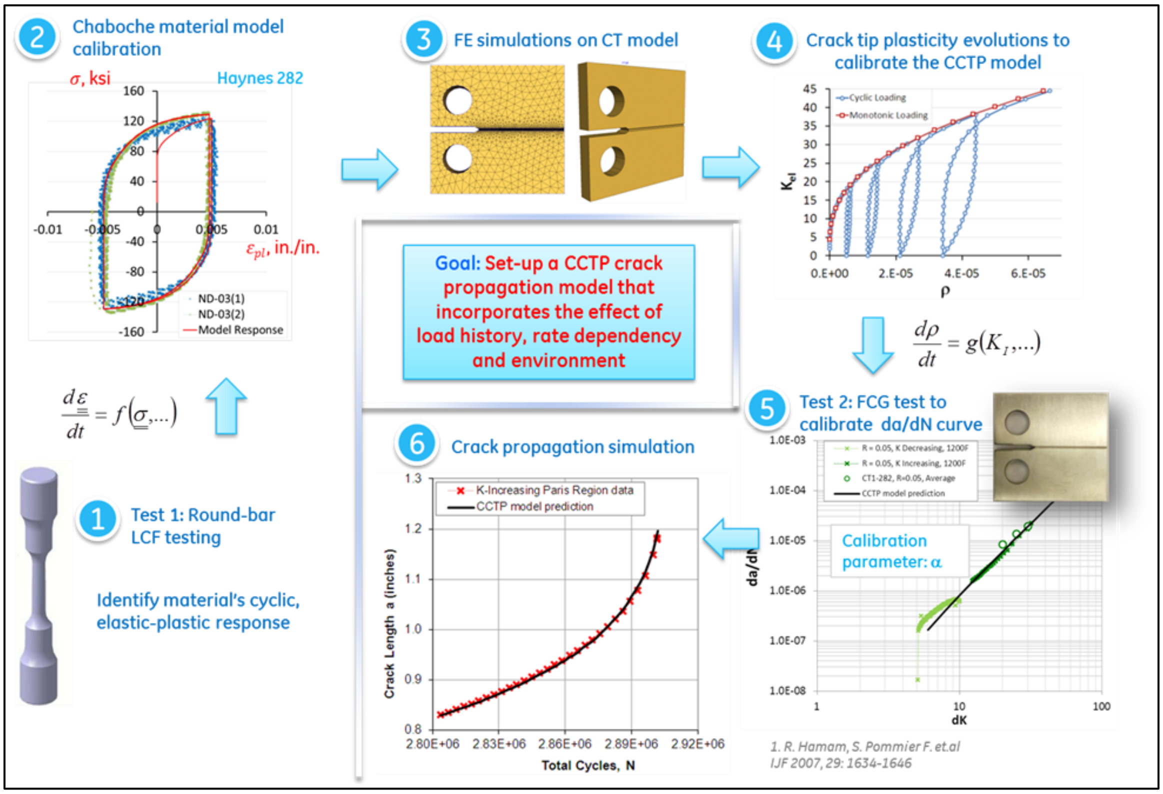

1. R. Hamam, S. Pommier F. et.al IJF 2007, 29: 1634-1646

Figure 90: Confined crack-tip plasticity model based on a framework proposed by Hamam and Pommier [44].

6.2. Development of constitutive material models

Constitutive equations of the rate-dependent material model Chaboche with Voce-hardening option are listed in Figure 91. The first equation represents the yield function *F*. In this equation, $\{s\}$ refers to the deviatoric stress tensor, $\{\alpha\}$ is the back stress tensor, and *R* is the isotropic hardening variable, also known as the yield surface. The back stress tensor $\{\alpha\}$ represents the translation of the yield surface, which evolves with the accumulated plastic strain $\check{\varepsilon}^{pl}$ as given in the second equation for kinematic hardening. The parameters C_i, γ_i are the constants that need to be determined during the calibration process. In this work, only two kinematic hardening models were used with four parameters C_1, γ_1 and C_2, γ_2. Third equation, known as a Voce hardening rule, corresponds to the

isotropic expansion of the yield surface *R*, and it has four parameters K_0, R_0, R_∞, and *b* that need to be determined. The final equation represents the exponential visco-hardening rule, which dictates the rate sensitivity of the material constitutive model. It introduces two additional constants making it a total of 12 material parameters that need to be defined during the calibration process.
For rate independent material calibration, the last equation in Figure 91 is not part of the constitutive law, so the total number of parameters in the rate-independent constitutive model is reduced to 10 (i.e., with the absence of *m* and *K*).

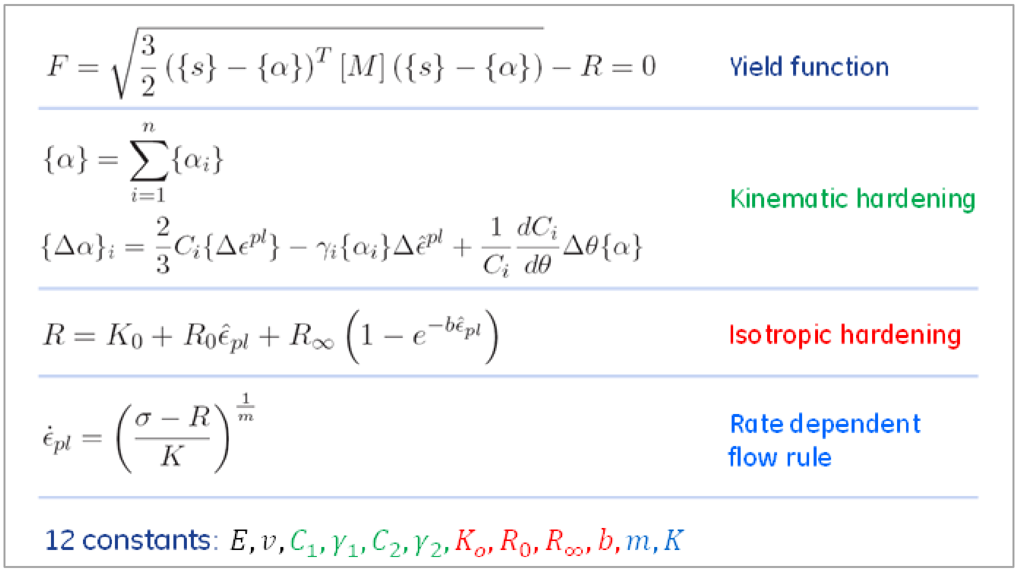

$$F = \sqrt{\frac{3}{2}\left(\{s\}-\{\alpha\}\right)^T [M]\left(\{s\}-\{\alpha\}\right)} - R = 0$$

Yield function

$$\{\alpha\} = \sum_{i=1}^{n}\{\alpha_i\}$$

$$\{\Delta\alpha\}_i = \frac{2}{3}C_i\{\Delta\epsilon^{pl}\} - \gamma_i\{\alpha_i\}\Delta\hat{\epsilon}^{pl} + \frac{1}{C_i}\frac{dC_i}{d\theta}\Delta\theta\{\alpha\}$$

Kinematic hardening

$$R = K_0 + R_0\hat{\epsilon}_{pl} + R_\infty\left(1 - e^{-b\hat{\epsilon}_{pl}}\right)$$

Isotropic hardening

$$\dot{\epsilon}_{pl} = \left(\frac{\sigma - R}{K}\right)^{\frac{1}{m}}$$

Rate dependent flow rule

12 constants: $E, v, C_1, \gamma_1, C_2, \gamma_2, K_o, R_0, R_\infty, b, m, K$

Figure 91: Governing equations of the material model Chaboche with Voce hardening [47].

6.2.1. Rate independent constitutive modeling

Round bar and compact tension (CT) specimens were used to collect bulk stress-strain and fatigue crack growth rate data. These specimens were machined from a rolled Alloy 282 billet. The billet was received in a solution-aged condition using a standard two-step heat treatment process[6], which transitioned the material into high strength.

A material constitutive model representing the cyclic stress-strain behavior is needed for CCTP model calibration[45]. Figure 92 presents an example materials stress-plastic strain data for Alloy 282 at 1200˚F test temperature in lab air. ANSYS [47] built-in Chaboche type constitutive model was used with both isotropic and kinematic hardening behaviors to capture this bulk material response. Material parameters listed in Table 10 were calibrated for test temperatures 1200˚F and 1400˚F using in-house optimization software PEZ. Predictions based on 1200˚F calibrated parameters are also plotted in Figure 92 by solid lines at different load ratios and strain ranges. The optimized material model captures the test data reasonably well.

Table 10: ANSYS built-in Chaboche material model parameters for Alloy 282

T	E, ksi	ν	σ_y, ksi	C_1, ksi	γ_1	C_2, ksi	γ_2	R_o, ksi	R_∞, ksi	b
1200F	2.5E4	0.3	72	8.3E4	7.6E3	1.7E4	360	2.6	0.036	5.9
1400F	2.3E4	0.3	63	8.6E4	4.8E3	1.0E4	600	5.0E-5	5.2E-4	7E-3

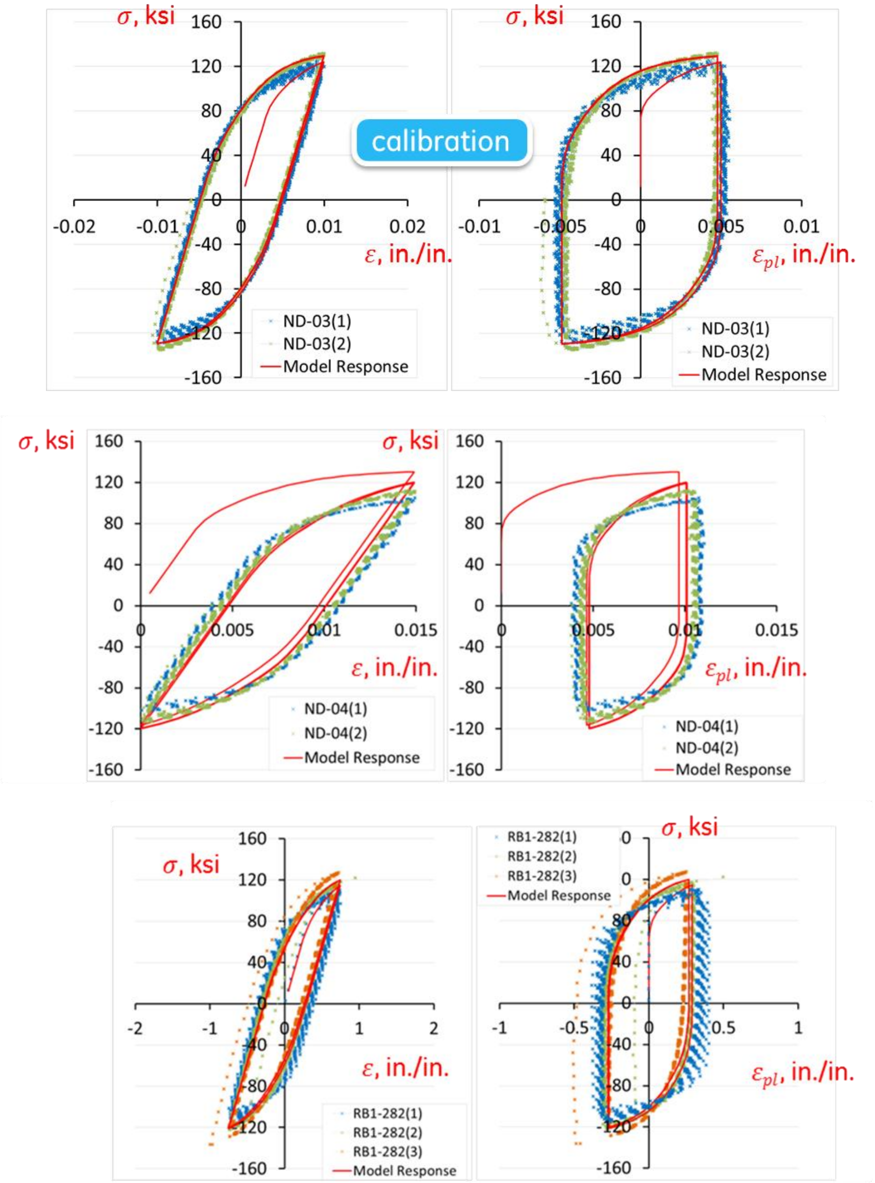

Figure 92: Stress-plastic strain data and material model prediction for Alloy 282 at 1200˚F.

6.2.2. Rate dependent constitutive modeling

Rate dependent Chaboche material model was calibrated to predict time dependent response of Alloy 282. Material test data was obtained for four zero-to-max strain ranges: [0, 0.0125], [0, 0.01], [0, 0.008], and [0, 0.007]. The stress-strain measurements for the applied strain range [0, 0.0125] are shown in Figure 93 (left). The hold-time period at the max strain for each test was about 6 hours, which allowed the applied max stress to relax as shown in Figure 93 (right). Plastic and total strain histories of the material from the same test are given in Figure 94. The objective was to obtain a proper parameter set for a constitutive model that captures all these rate dependent material behaviors.

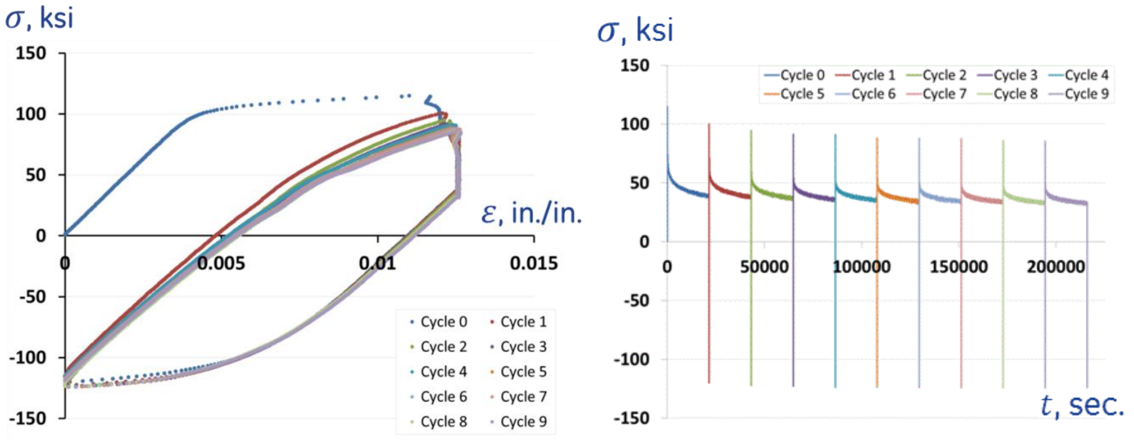

Figure 93: Stress-strain (left) and stress history (right) responses of Alloy 282 for the strain range [0, 0.0125]

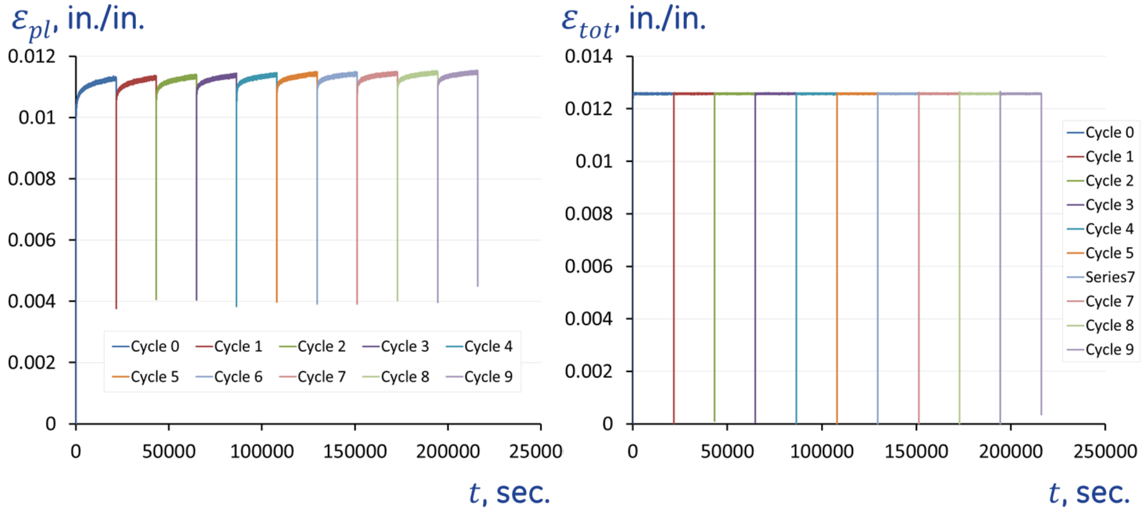

Figure 94: Plastic strain (left) and total strain (right) history of Alloy 282 from the constant strain amplitude test with a strain range [0, 0.0125].

Each test measurement contained over 130,000 data points. They were filtered to about 1,300 points, which were then used as the applied load steps for the FE model. The input to the FE model was the total strain history $\varepsilon_{tot}(t)$ prescribed in terms of the displacement load $u_y(t)$. The outputs were the stress and the plastic strain histories ($\sigma_y(t)$ and $\varepsilon_y^p(t)$) along the loading direction. The material parameters were calibrated manually (by trial and error) to reduce the difference between observed and predicted stress response.

Two different parameter sets for the material model are proposed, which are given in Figure 95. The first one was calibrated using the data with the largest applied strain range [0, 0.0125], while the second one was calibrated with the second largest strain range [0, 0.01] (see Figure 95). In Figure 96, the stress and strain histories of these models are compared with the corresponding test data.

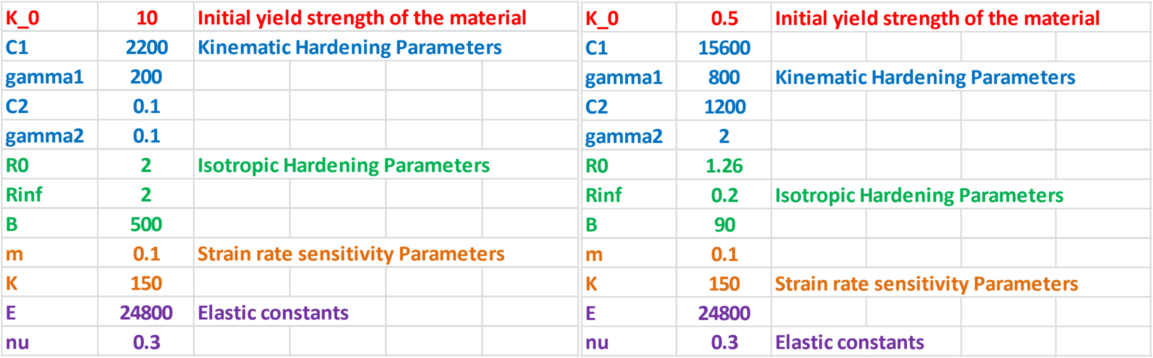

K_0	10	Initial yield strength of the material	K_0	0.5	Initial yield strength of the material
C1	2200	Kinematic Hardening Parameters	C1	15600	
gamma1	200		gamma1	800	Kinematic Hardening Parameters
C2	0.1		C2	1200	
gamma2	0.1		gamma2	2	
R0	2	Isotropic Hardening Parameters	R0	1.26	
Rinf	2		Rinf	0.2	Isotropic Hardening Parameters
B	500		B	90	
m	0.1	Strain rate sensitivity Parameters	m	0.1	
K	150		K	150	Strain rate sensitivity Parameters
E	24800	Elastic constants	E	24800	
nu	0.3		nu	0.3	Elastic constants

Figure 95: Parameter sets for the material constitutive model: (left) model 1, (right) model 2.

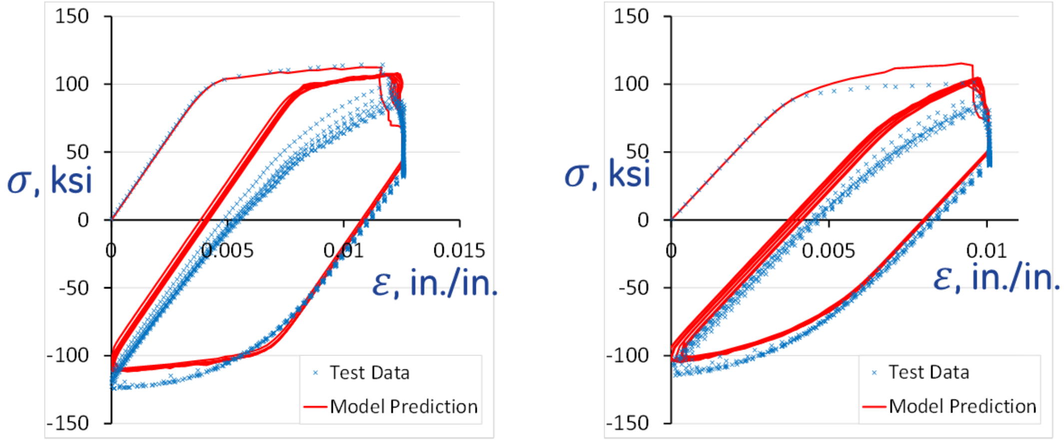

Figure 96: Stress-strain response of the calibrated models: (left) model 1, (right) model 2.

Figure 97 through Figure 100 compare the first material model response with the experimental measurements for the remaining strain ranges. Figure 101 through Figure 103 compare the second model response with the experimental data.

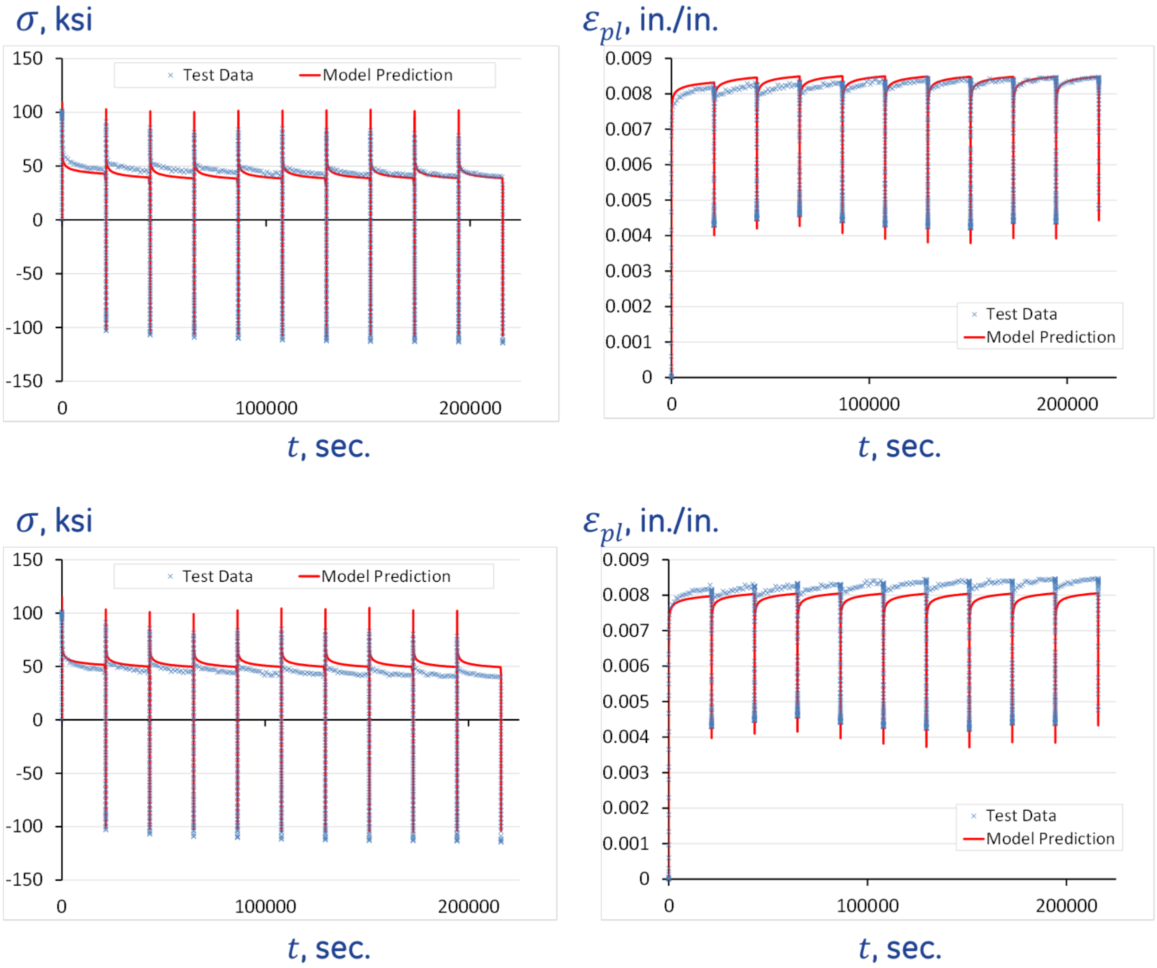

Figure 97: Stress and strain histories of the calibrated models: (top) model 1, (bottom) model 2.

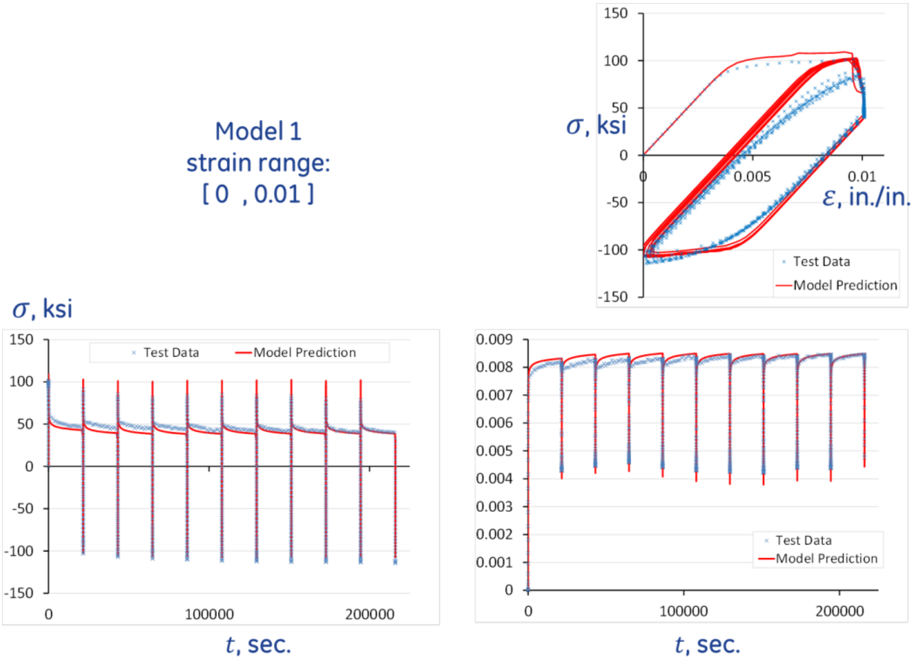

Figure 98: Model 1 response compared with test data for the strain range [0, 0.01].

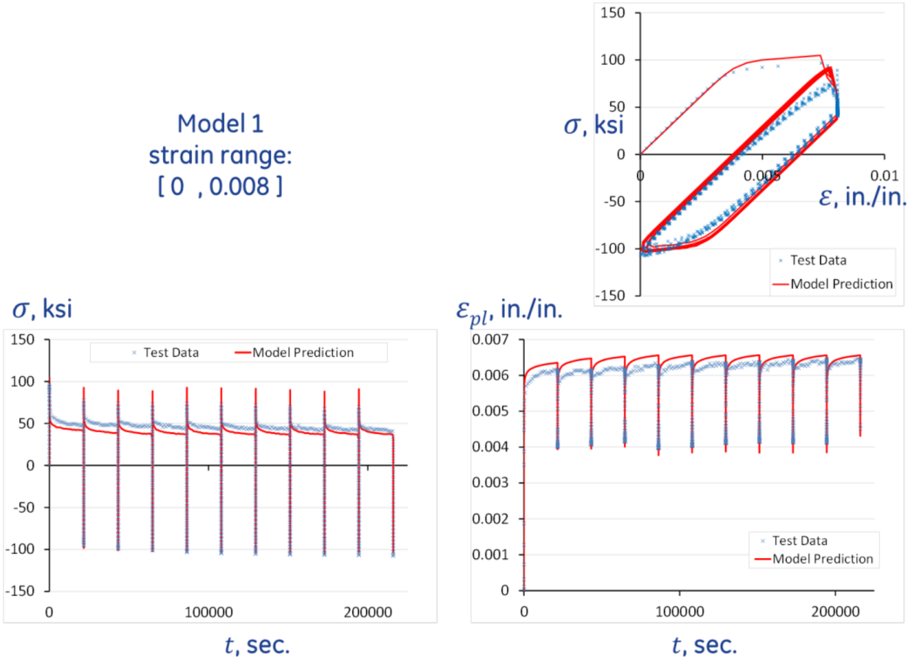

Figure 99: Model 1 response compared with test data for the strain range [0, 0.008].

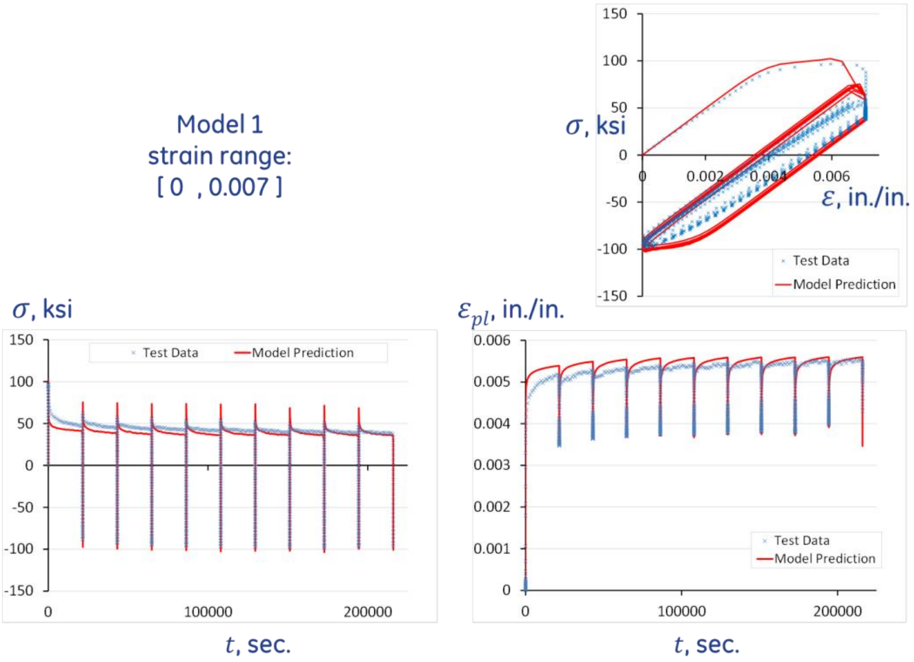

Figure 100: Model 1 response compared with test data for the strain range [0, 0.007].

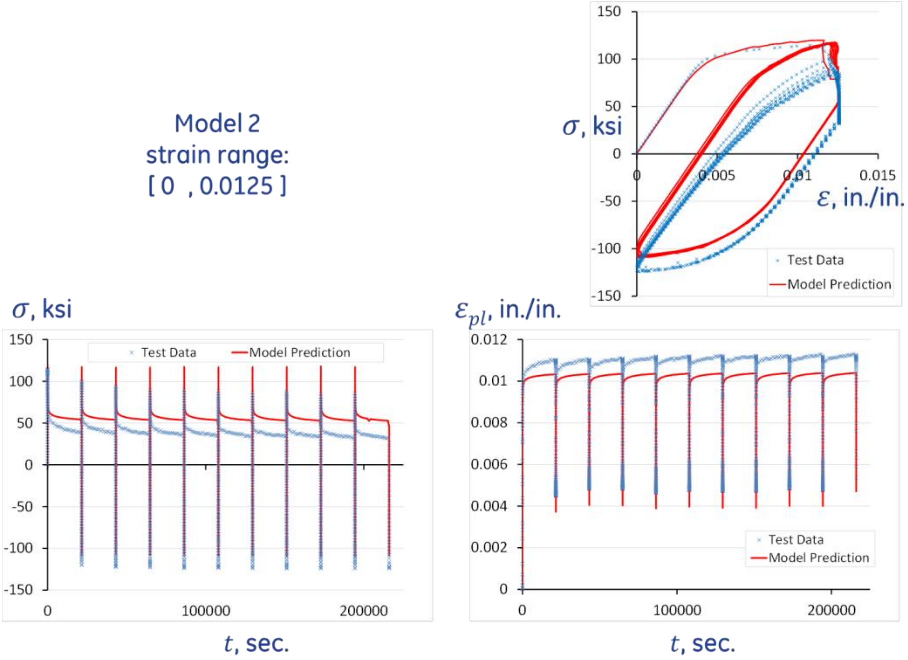

Figure 101: Model 2 response compared with test data for the strain range [0, 0.0125].

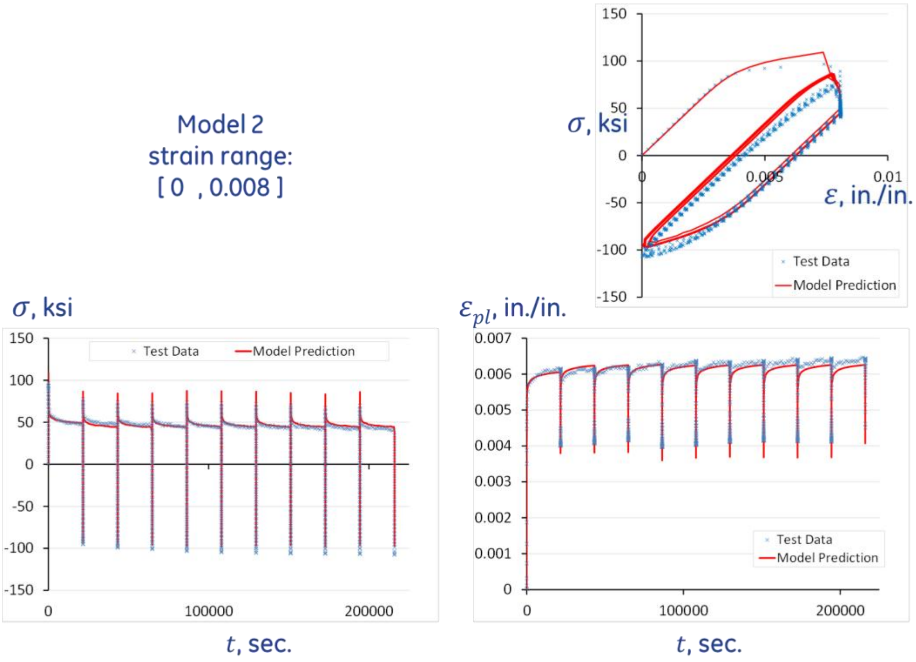

Figure 102: Model 2 response compared with test data for the strain range [0, 0.008].

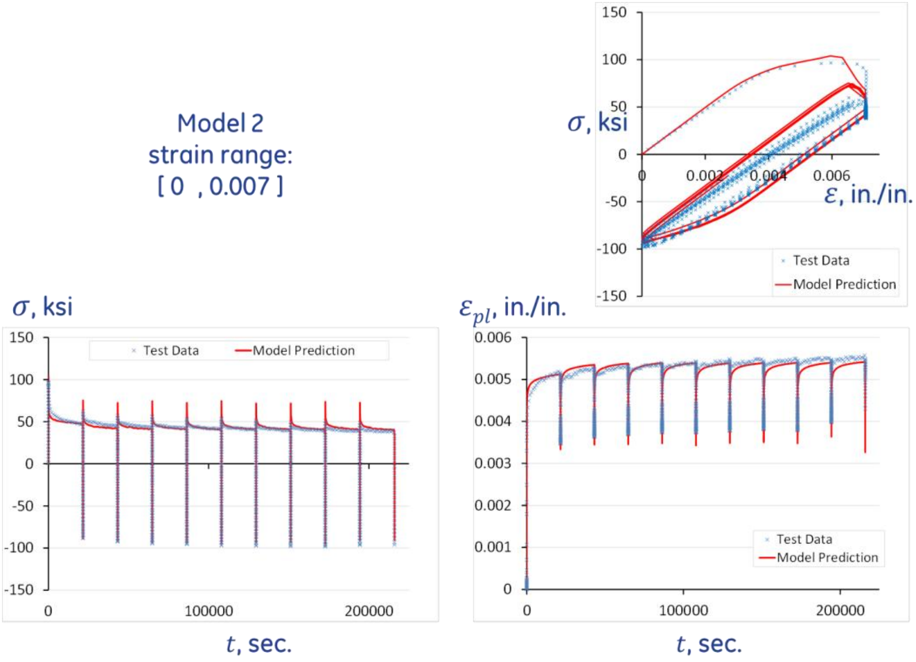

Figure 103: Model 2 response compared with test data for the strain range [0, 0.007].

6.3. CCTP model calibration

6.3.1. Crack tip blunting

As mentioned previously, we made use of a modeling framework proposed by Pommier[45]. Main concepts of the methodology are described below. For further details on the model formulations, reader is advised to review[43-45].

Figure 104 shows the elastic and elastic-plastic crack face displacement profiles obtained from a 2D plane stress model of a CT specimen for the applied load of K_I=32$ksi\sqrt{in}$. To keep consistency with the test data, the CT specimen was modeled to obtain the crack face displacement solutions. Figure 105 shows the model dimensions and the 2D FE mesh with prescribed boundary conditions. It is observed that after some distance behind the crack tip the elastic and elastic-plastic crack face displacement solutions differ by a constant value ρ, which is referred as crack tip blunting. In fact, the elastic-plastic crack face displacements in the LEFM (Linear Elastic Fracture Mechanics) region can be represented by the following relation[45]:

$$u_{elpl}(r) = \widetilde{K}_I u^e(r) + \rho \tag{6.1}$$

where $u_{elpl}(r)$ represents the displacement field of the crack face computed with an FE model that considers an elastic-plastic constitutive model; $u^e(r)$ represents the displacement field of the crack face computed with an FE model that considers an elastic constitutive model; $\widetilde{KI}$ represents the amplitude of the elastic displacement; ρ represents plastic flow intensity factor.

In a rate (i.e., differential) form, Equation (6.1) becomes

$$\frac{du_{elpl}(r)}{dt} = \frac{d\widetilde{K}_I}{dt} u^e(r) + \frac{d\rho}{dt} \tag{6.2}$$

The importance of crack tip blunting is the fact that the change in ρ has a direct relation to the crack propagation rate via the following damage law[44,45] :

$$\frac{da}{dt} = \alpha \left|\frac{d\rho}{dt}\right| \tag{6.3}$$

The law above can be conveniently extended to incorporate creep and environment effects[43]:

$$\frac{da}{dt} = \alpha \left|\frac{d\rho}{dt}\right| + \frac{\partial a}{\partial t}_{creep} + \frac{\partial a}{\partial t}_{oxidation} \tag{6.4}$$

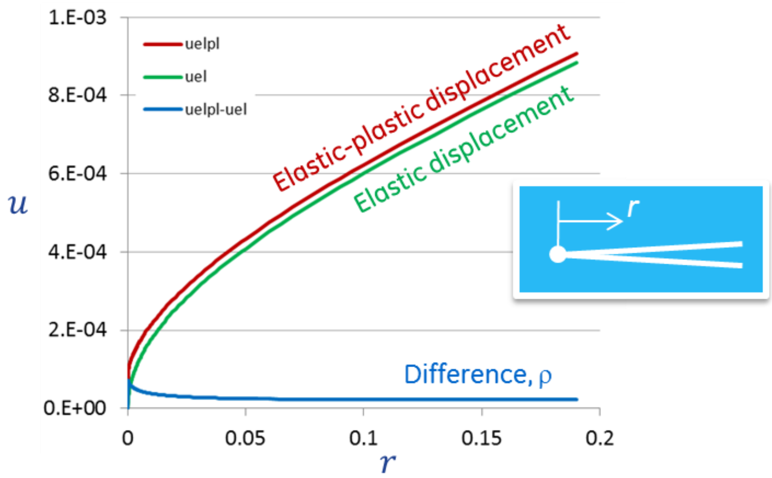

Figure 104: Crack face displacement profiles and the crack tip blunting ρ.

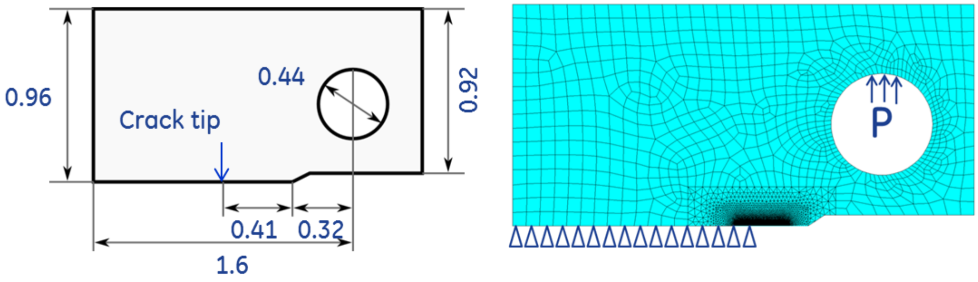

Figure 105: FE model dimensions (inches) and mesh of a CT test specimen.

6.3.2. Evolution equations

The objective is to use FE model of a CT specimen to determine the evolution of crack tip blunting ρ with respect to applied remote load (K_I) and the crack growth (*da*), and set-up a FORTRAN based CCTP model for crack propagation. The evolution of ρ with respect to *K* for Alloy 282 alloy at 1200˚F is given in Figure 106. It contains monotonic and cyclic plastic zones shown in green and blue symbols, respectively.

To be able to represent such crack tip deformation behavior in incremental fashion, the evolutions equations of total of four internal variables are needed, first two associated with monotonic plastic zone (φ_m, φ_{xm}), and the last two representing the cyclic plastic zone (φ_c, φ_{xc}):

$$\frac{\partial \varphi_m}{\partial \rho}, \frac{\partial \varphi_{xm}}{\partial \rho}, \frac{\partial \varphi_c}{\partial \rho}, \frac{\partial \varphi_{xc}}{\partial \rho} \text{ and } \frac{\partial \varphi_m}{\partial a}, \frac{\partial \varphi_{xm}}{\partial a} \quad (6.5)$$

The transfer functions were modified from what was suggested in the literature to obtain a better approximation of the FE results. For example the two plots in

Figure 107 compare the FE solutions of cyclic deformation response with the predictions by the evolution equations given in the plot. The modified incremental formulation shown on the right seems to better characterize the FE solutions. The improvement in the CCTP model predictions against the FE results can also be seen in Figure 108 for both monotonic and cyclic loads of different levels.

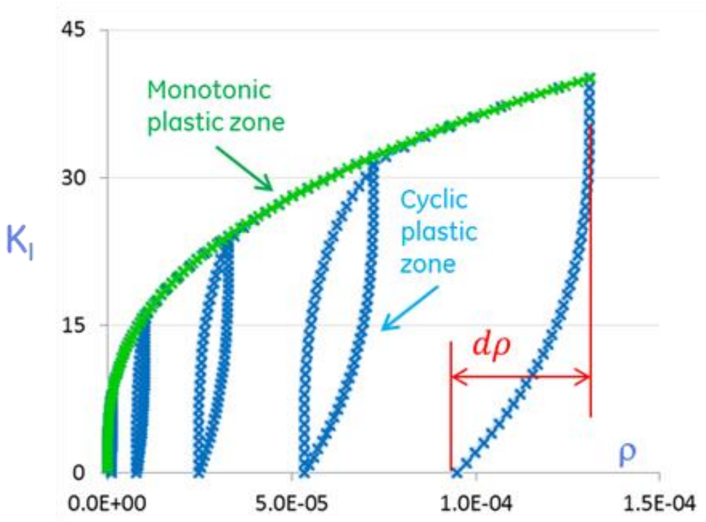

Figure 106: FE model solutions of crack tip blunting and CCTP model predictions.

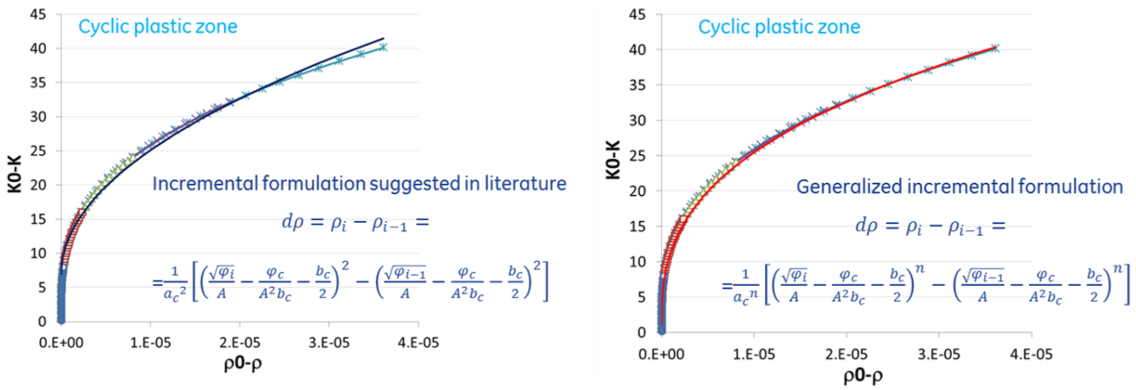

Figure 107: Predictions with calibrated evolution equations against the FE solution for the cyclic plastic zone.

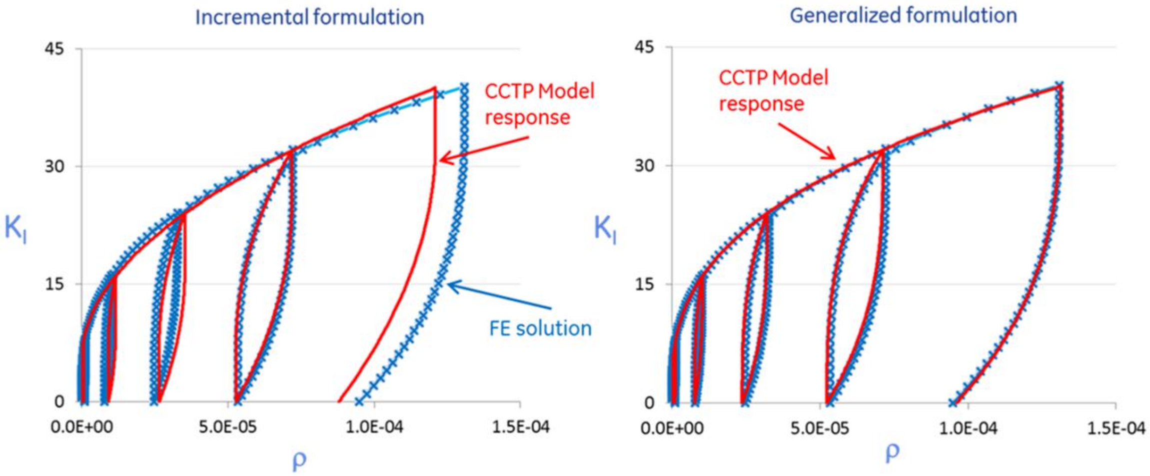

Figure 108: Predictions with calibrated evolution equations against the FE solution for both monotonic and cyclic loading.

6.3.3. Overload and crack closure effects

To include the load history effect in FCGR predictions, evolution equations for crack tip closure were used as suggested in [45]. Following differential equations for size (φ_m) and center location (φ_{xm}) of monotonic plastic zone with respect to the crack size govern the crack closure and overload effects in the model:

$$\frac{d\varphi_m}{da} = p_a \varphi_m \tag{6.6}$$

$$\frac{d\varphi_{xm}}{da} = k_a \varphi_{xm} + k_b \varphi_m \tag{6.7}$$

The parameters p_a, k_a and k_b in these equations can be determined using simplified assumptions proposed in [45]. For example, the parameter p_a is estimated from the FE solution of average equivalent plastic strain gradient near the crack tip (Figure 109). The closure parameters k_a and k_b are determined from either crack propagation simulation (approach used in this work), or alternatively using the weight function for the cracked geometry along with the residual stress field obtained from the FE model in front of the crack tip at a zero load. The blue symbols plotted in Figure 110 are the FE solutions of K_{xm}, whereas the underlaid blue line is the CCTP model prediction calibrated against these FE results. Alternative approach to identify these three parameters would be to use the da/dN data at different load ratios and with different overloads levels.

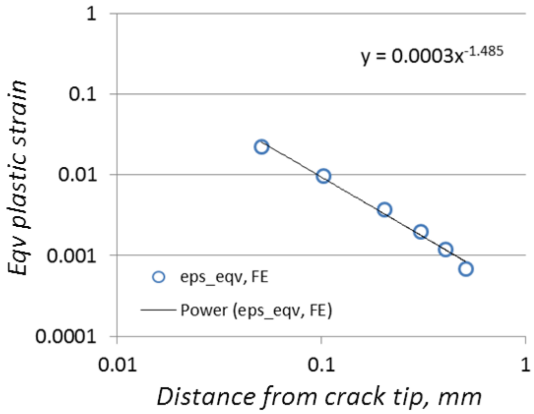

Figure 109: Average equivalent plastic strain levels near the crack tip were used to obtain the parameter p_a.

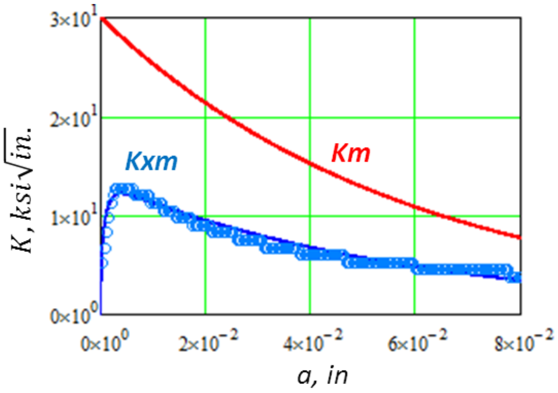

Figure 110: Crack closure governing variables K_m and K_{xm} with crack length.

In Figure 111, K_{xm} (closure level) is plotted by a red line and the green curve is K_m, the (size of monotonic plastic zone) both expressed in terms of stress intensity factors and are related to energy terms φ_m and φ_{xm} by a simple LEFM relation:

$$K = \sqrt{\frac{\varphi}{E}} \tag{6.8}$$

At the onset of overload event at *a*=0.1 inch, where a single cycle with 1.8 times of the maximum load is applied, the closure level (K_{xm}) is instantly reduced producing crack growth acceleration effect and the K_m is expanded. Next, as the K_m level gradually comes back down to initial value, the K_{xm} goes up to max level producing crack growth retardation effect. After reaching the peak value, K_{xm} is reduced back to the initial level thus putting an end to the transient crack growth retardation effect. Figure 112 shows the overload retardation effects occurring during K-increasing and constant dK crack propagation simulations. It must be noted that under-load (or compressive overload) effects, although seen in experience, are not accounted for in this model; it requires additional developmental work to add such effects.

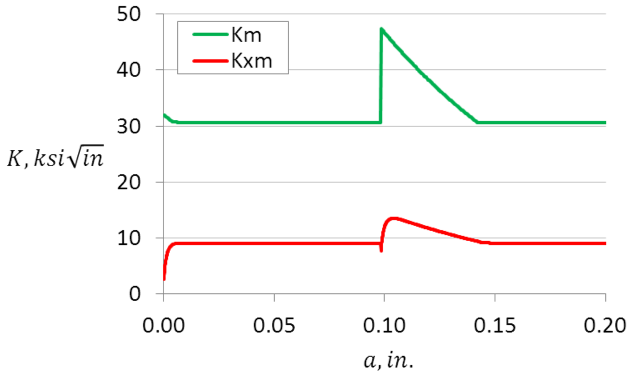

Figure 111: Crack closure governing variables K_m and K_{xm} with crack length.

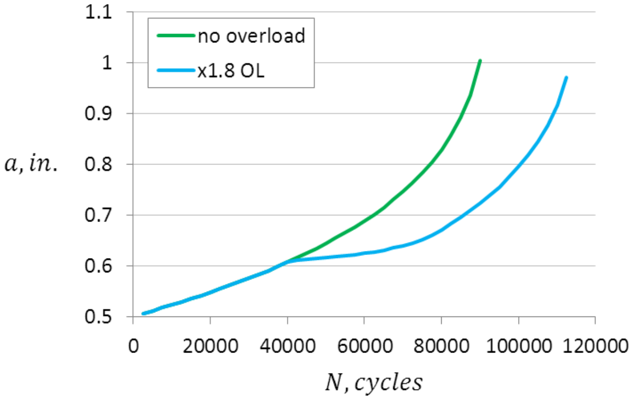

Figure 112: Model predictions showing 1.8X overload retardation effect during dK increasing crack growth simulation.

6.3.4. Model calibration

Figure 113 shows the experimental da/dN vs. dK data at 1200˚F and R=0.05, which was used to calibrate the CCTP model (also shown). During calibration, the value of α in (da/dt = αdρ/dt) was set to align the prediction vertically with the experimental data; the slope is predicted by the model.

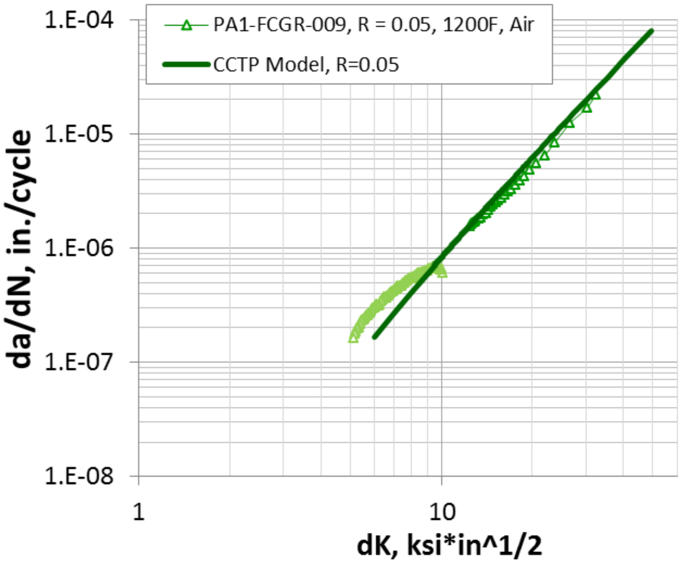

Figure 113: CCTP model calibration against crack growth rate data at 1200˚F and R=0.05.

6.3.5. Results and discussion

Figure 114-Figure 116 present the CCTP model predictions of cyclic crack growth rates for 1200˚F test temperature at three different load ratios: R=0.05, 0.25 and 0.5 for which experimental data have been collected. The slope of the lines representing the linear Paris regime of the *da/dN* curve is predicted by the model. In Figure 117, larger pool of experimental data for R=0.05, all tested at 20 cpm (cycle per minute), are plotted along with the model predictions. The dashed lines also included in the figure represent 2x bands, a typical scatter observed with crack growth data. The 2X bands are obtained using the predicted curve (solid line) in such a way so that the upper boundary is twice the lower boundary, while the prediction is at the midpoint of the two. Most of the experimental data seem to fall within this band except for lower ΔK regions of the data coming from specimen labeled as PA1-FCGR-009. This data set exhibits abrupt change in slope near $20ksi\sqrt{in}$. leading to exceptionally high crack growth rates at lower load ranges. Such "kinking" trend is rather frequently observed in our test data for Alloy 282 alloy at both 1200˚F and 1400˚F in steam and air. The exact cause of this behavior is not fully understood yet, but one possible explanation could be the presence of combined microstructure-environment effects leading to detectable crack growth acceleration above the threshold region.

Figure 118 and Figure 119 present similar type of data-to-prediction comparisons at two higher load ratios *R*=0.25 and 0.5. Presented FCGR data in these plots also include those tested in vacuum. The vacuum test specimen in Figure 116 (CT13-282) for *R*=0.25 exhibits lower crack growth rates at higher load end. However, it is difficult to conclude that this is due to absence of environment effects based on a single test data since it may as well be coming from the experimental noise. Although, one plausible difference observed in vacuum data might be the absence of accelerated crack growth near threshold regime. It is observed in both plots in Figure 115-Figure 116 that the vacuum da/dN data transition down to threshold at noticeably higher dK levels of near $10ksi\sqrt{in}$. Within the Paris region (i.e. region II), majority of the air and vacuum data at R=0.25 and 0.5 lie within the 2X band predictions. Hence, the calibrated CCTP model seems to capture average load ratio effects for the range *R*=0.05 to 0.5 reasonably well. It must be noted, however, that the model does not predict further shifts in da/dN curves beyond *R*=0.5 if such trend existed in the data, because predicted crack closure is absent for *R*>0.3 in the calibrated model.

Figure 117-Figure 119 present da/dN data tested at 1400˚F along with corresponding predictions. Similar to previous plots, 2X bands estimated from the predicted line are also included by dashed lines in the figure. Figure 117 shows the data tested in air, steam and vacuum at the load ratios of *R*=0.05 and 0.1. The model calibrated for 1400˚F test temperature captures the average crack growth rate behavior. Majority of the experimental scatter are bounded by the 2X band with a couple of exceptions. The specimen PA1-FCGR-001 tested in air at *R*=0.05 exhibits change in slope near $20ksi\sqrt{in}$, below which crack growth acceleration is detected in a similar way to previously discussed data at 1200˚F. This data falls outside the upper boundary of 2X band at load levels $\Delta K < 15ksi\sqrt{in}$. Also, PA1-FCGR-001 produced exceptionally high growth rates that come out of 2X band for $\Delta K < 26ksi\sqrt{in}$. It appears as if CT12 exhibits kinking at little higher load level of around $26ksi\sqrt{in}$.

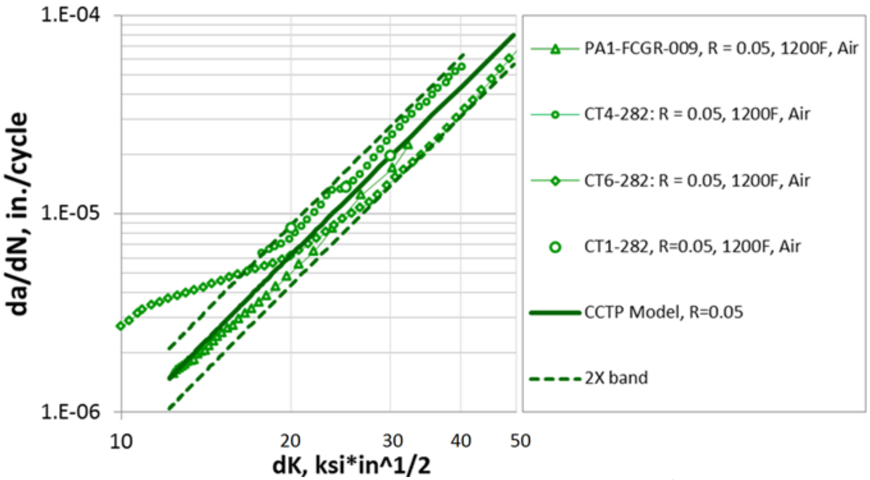

Figure 114: CCTP model prediction at R=0.05 and T=1200˚F with 2X band.

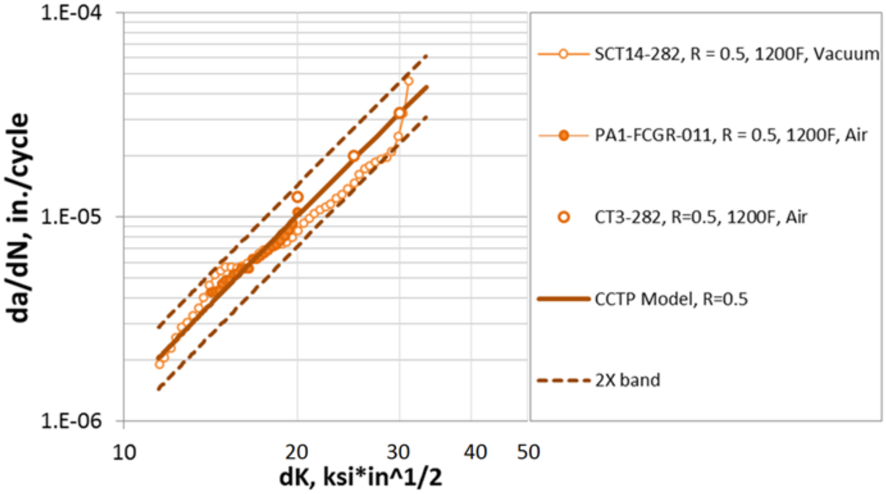

Figure 115: CCTP model prediction at R=0.5 and T=1200˚F with 2X band.

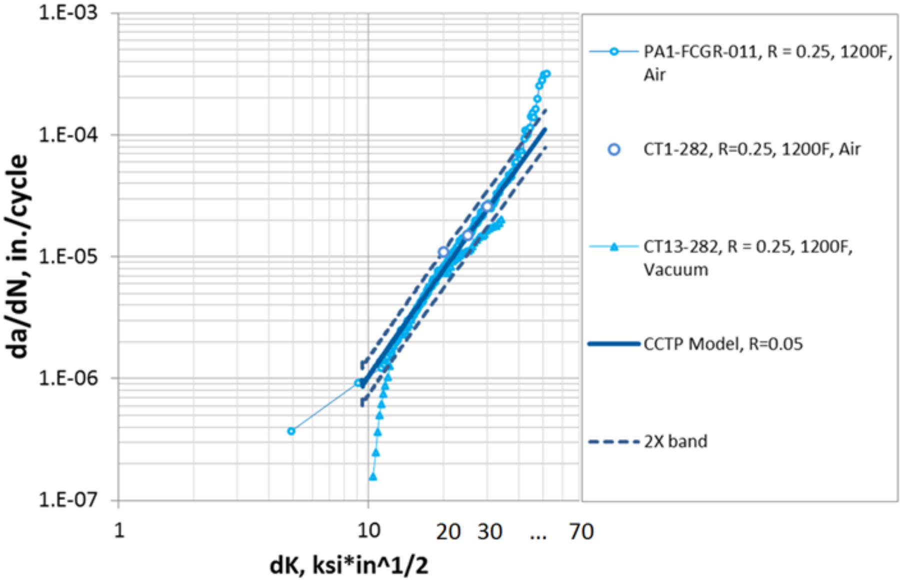

Figure 116: CCTP model prediction at R=0.25 and T=1200˚F with 2X band.

The FCGR measurements along with model predictions for *R*=0.25 and 0.5 at 1400˚F are plotted in Figure 118 and Figure 119. Only single specimen data per load ratio were available, which were tested in air. Thus, the experimental scatter is not captured at these two load ratios. However, the model predicts the slope of the data reasonably well at higher load ranges. Also, change of slope is observed pushing the crack growth rate measurements upward when $\Delta K < 20 ksi\sqrt{in.}$

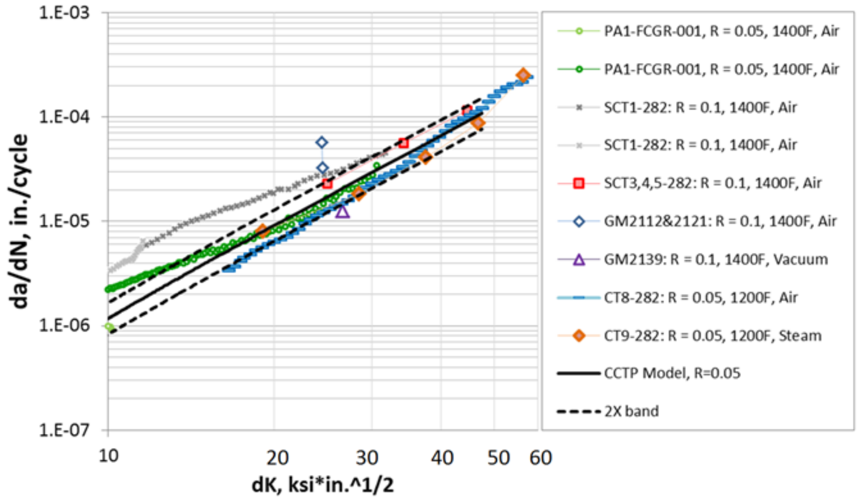

Figure 117: CCTP model predictions of cyclic FCGR for 1400˚F test temperature, R=0.05.

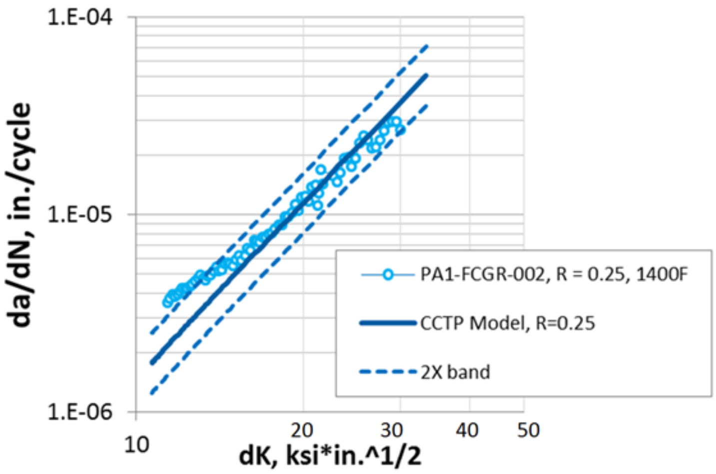

Figure 118: Prediction versus data at R=0.25, T=1400˚F.

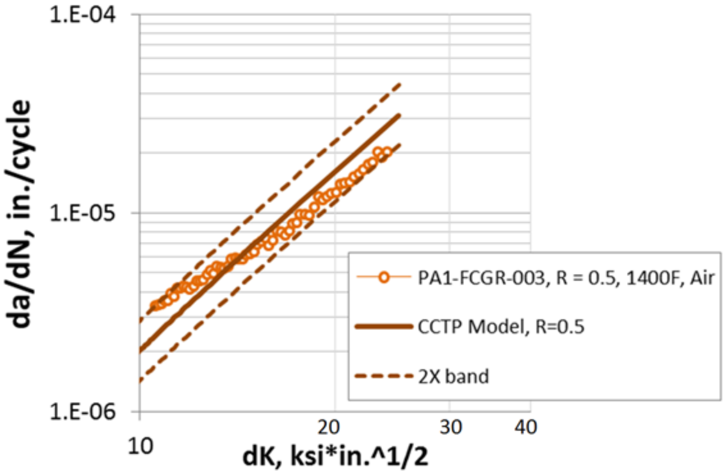

Figure 119: Prediction versus data at R=0.5, T=1400˚F.

6.4. Incorporate oxidation effects

One of the objectives of this work was to build a fatigue crack growth model that takes into account the damaging effects associated with hold-time, whether they are stemmed from harsh environment or creep deformation. A series of hold-time sweep tests on Alloy 282 indicated that the oxidation assisted damage mechanism dominates for temperatures 1400˚F and lower (see Section 2.1), since the hold-time effects under vacuum were negligible. As a natural extension to the incremental plasticity modeling framework described in previous sections, the team decided to evaluate the oxidation based growth modeling approach proposed in [46] (no creep effects considered). This phenomenological model introduces an additional term to the time independent damage law to bring in the time dependent portion of the crack growth rate:

$$\frac{da}{dt} = \alpha \frac{d\rho}{dt} + \frac{\partial a}{\partial t_{oxidation}} \qquad (6.9)$$

The evolution of the new damage term is established as follows. It is realized that this term should include two distinct oxidation phenomena. First is the oxygen diffusion along the grain boundaries, which weakens the bond and increases the crack growth rate. Second is the growth of a passivation oxide layer which limits the diffusion process of oxygen into the virgin material ahead of the crack tip. To account for the effect of the passivation layer, the oxidation term above is defined as a product of two parameters:

$$\frac{\partial a}{\partial t_{oxidation}} = \beta \cdot m \qquad (6.10)$$

where, β controls the maximum speed, at which crack may grow in the absence of passivation layer formation. The second term m regulates the magnitude of β and varies between 0 and 1 (i.e., $0 \leq m \leq 1$). When passivation oxide layer is thick for example, the rate of oxidation based crack growth becomes negligible ($m \ll 1$). The term β depends on temperature, whereas m varies with time and mechanical loading as follows:

$$\frac{\partial m}{\partial t} = -R_t \cdot m \qquad (6.11)$$

where, R_t is the calibrating parameter. The evolution equation (6.11) governs the growth of oxide layer over time to slow down the oxidation crack growth. During loading, $d\rho > 0$, the passivation layer is broken and underlying virgin material is exposed to environment leading to grain boundary embrittlement and intergranular crack growth:

$$\frac{\partial m}{\partial \rho} = -R_\rho \cdot (1 - m) \quad for\ d\rho > 0 \qquad (6.12)$$

where R_ρ is the second calibrating parameter.

During unloading, when the applied stress intensity factor dK_I increment is negative ($dK_I < 0$), the passivation layer is closed up and the crack tip is protected from environment:

$$\frac{\partial m}{\partial K_I} = -R_K \cdot m^2 \quad \text{for } dK_I < 0 \tag{6.13}$$

where R_K is the third calibrating parameter.

In order to calibrate this model, several crack growth test data were required. Table 11 below shows a list of test conditions proposed to fully calibrate and validate the oxidation based part of the damage model. However, due to funding and time constraint, only tests 1 through 6 were completed and used for the model calibration. Note that the team decided to run tests in steam environment to represent the engine-like condition.

Figure 120 shows the collected crack growth rate data tested at 1400˚F and 100s, 1,000s, 10,000s, and 100,000s hold times in steam. Also included in the plot is the baseline data tested in air with no hold time (labeled as 20cpm). First, it is observed that the effect of steam environment is negligible for the hold-times of up to 100s. The plot also indicates that the crack growth acceleration (i.e., upward shift in da/dN plot) does not change significantly beyond 10,000s. The data for the 1,000s hold time shows some environment interaction effect at lower ∆K levels. For the ∆K≥40ksi√in., 1,000s the data is converged to the baseline curve, indicating negligible effect of environment. However, more data is required to fully understand and conclude on the general trend-line caused by periodic exposure to steam.

Two separate calibrations were done using the available hold-time FCGR data tested in steam:

1. Assume the slope remains similar for different hold-time tests and prolonged exposure to environment causes a vertical shift in FCGR curves (Figure 120, calibrated parameters: $\beta = 4E\text{-}6, R_t = 1E\text{-}4, R_\rho = 200, R_K = 5000$)
2. Assume the change of slope for shorter 1000s hold time data is real material behavior (Figure 121, calibrated parameters: $\beta = 8E\text{-}7, R_t = 5E\text{-}5, R_\rho = 700, R_K = 6$)

In running the crack growth simulations above, the model was run for a few cycles until the Equations (6.11)-(6.13) (thus the crack growth rate response) reached a saturated level before the results are printed out. Typically maximum of three (3) to four (4) cycles were found adequate to reach saturation.

The calibrated model captures qualitatively the experimental shift due to different hold-times. However, to decide which calibration below is a better fit, more data (including lower ΔK loading levels) is needed first to better understand the average observed behavior.

Table 11: Proposed test matrix

Testing plan proposed to calibrate/validate CCTP model to capture environment effect						$\frac{\partial a}{\partial t} = m \cdot \beta$
Test No.	**Temp (F)**	**Environment**	**R ratio**	**Load-Hold-Unload (sec)**	**Load**	**Commments**
1	1400	air	0.05	1.5-0-1.5	dK increasing	dK sweep data with no environmental effects (for reference)
2	1400	steam	0.05	1.5-0-1.5	dK increasing	will be used to calibrate the model constant Rt that controls time dependent behavior: $\frac{\partial m}{\partial t} = -R_t m$
3	1400	steam	0.05	10-100-10	dK increasing	
4	1400	steam	0.05	10-1000-10	dK increasing	
5	1400	steam	0.05	10-10000-10	dK increasing	
6	1400	steam	0.05	10-100000-10	dK increasing	
7	1400	steam	0.05	1000-0-10	dK increasing	will be used to calibrate Rr in the incremental equation of m with respect to crack tip plasticity: $\frac{\partial m}{\partial \rho} = R_\rho(1-m)$
8	1400	steam	0.05	10-0-1000	dK increasing	
9	1400	steam	0.05	10-1000-10 w/ 10% overload	dK increasing	will be used to calibrate Rk in equation: $\frac{\partial m}{\partial K} = R_K m^2$
10	1400	steam	0.05	10-1000-10 w/ 20% overload	dK increasing	
11	1400	steam	0.05	10-1000-10 w/ 30% overload	dK increasing	
12…	1400	steam	0.05	10-1000-10 complex mission	dK increasing	for validation: tests with different hold times, oveloads, load ratios combined

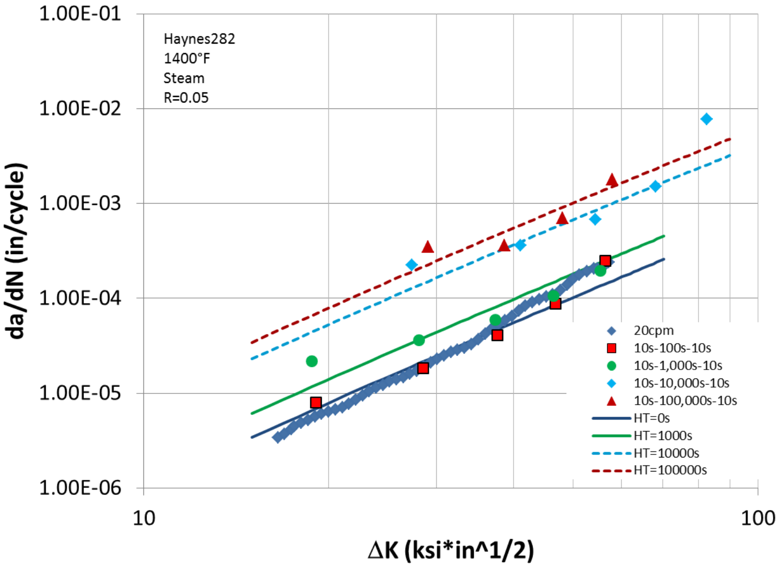

Figure 120: Crack growth data along with predictions using the first set of calibration parameters.

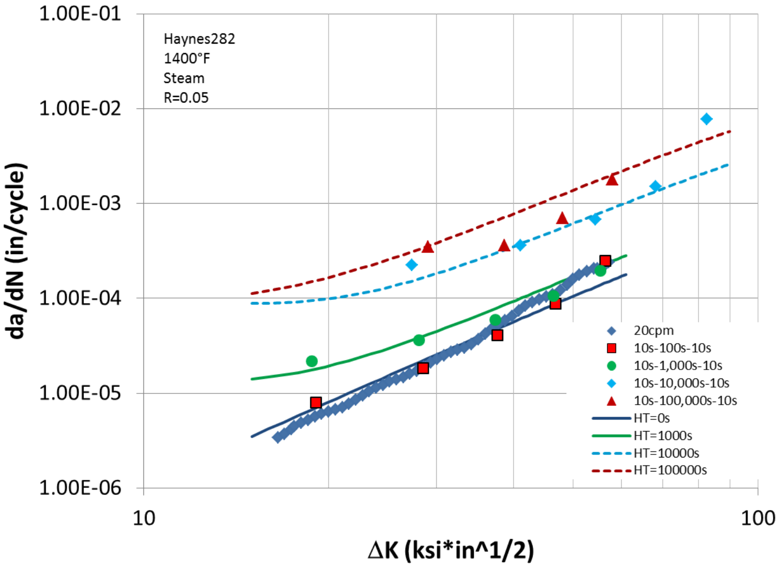

Figure 121: Crack growth data along with predictions using the second set of calibration parameters.

6.5. 3D Crack propagation simulation: FE model setup

Using the validated crack propagation model based on test data and 2D FE models, a 3D crack propagation simulation was implemented using ANSYS and 3DFAS (GE proprietary software tool). The compact tension 3D geometry was used to insert the initial crack and advance it to simulate the crack propagation process. Assuming crack advancement symmetry, only quarter model was used in the simulations. Processing (solution) and post-processing were carried out in

ANSYS while 3DFAS was used as a preprocessor (for advancing the crack and mesh the model).

A typical mesh is shown in Figure 122. One of the most difficult meshing tasks is to control the mesh pattern along the crack front. For the initial crack front the mesh pattern is shown in Figure 122, while Figure 123 shows the same mesh pattern after a given crack front advancement. The mesh pattern is used to extract displacement data on the crack faces necessary to post-process the results of each simulation and propagate the crack according to the established model ($da/dt = \alpha|d\rho/dt|$). Basically, the post-processing that we conducted in the 2D FE models is performed for each node along the crack front in the 3D model, and for each crack front increment throughout the entire crack growth simulation.

3D Mesh of the entire CT specimen

Due to symmetry only one quarter was used

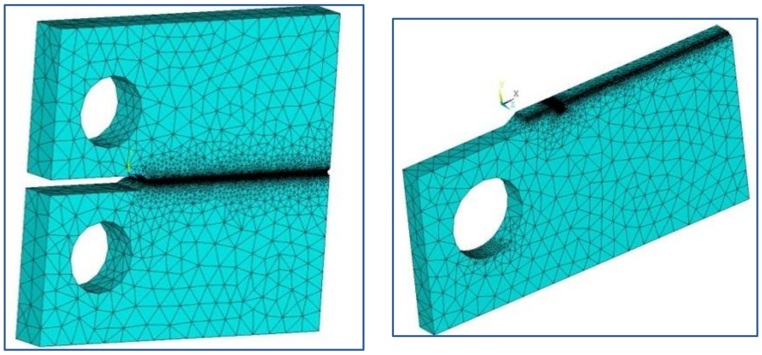

Crack front mesh

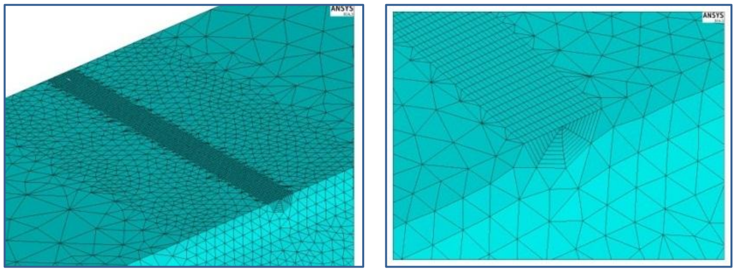

Figure 122: Typical FE mesh used in the 3D crack propagation simulation.

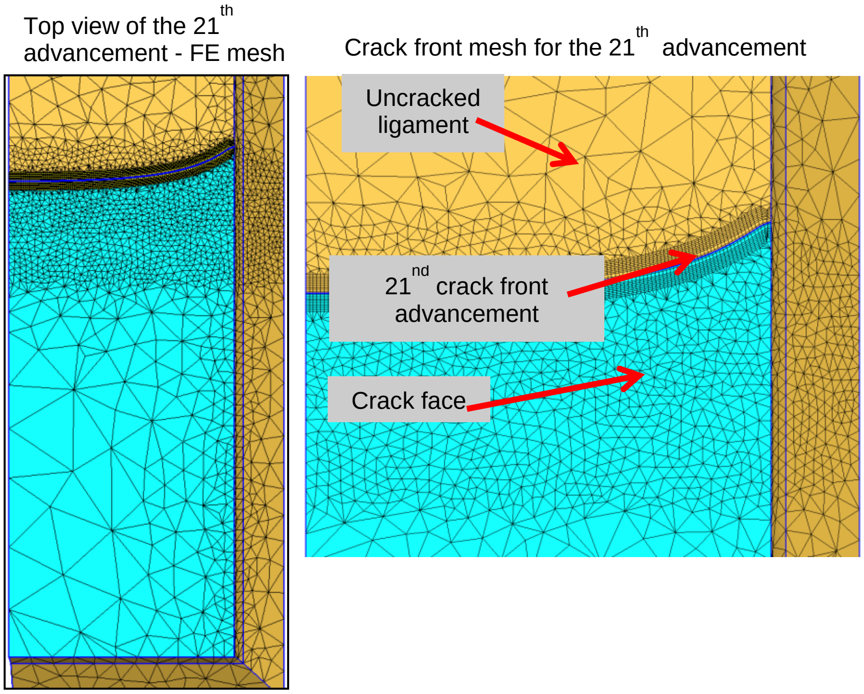
Top view of the 21th advancement - FE mesh

Crack front mesh for the 21th advancement

Uncracked ligament

21nd crack front advancement

Crack face

Figure 123: Example of the FE mesh after 21 advancements steps.

Two simulation steps are needed for each crack advancement simulation:

1. The first step uses an elastic constitutive model to capture elastic displacements behind each crack front node along the crack front
2. The second step uses the Chaboche constitutive model calibrated at 1400˚F.

The boundary conditions used in this simulation constrain the symmetry planes and rigid body motion while the loading is applied to several nodes in the pin holes of the CT specimen. The crack propagation simulation consists of following steps:

1. Insert initial crack, create the mesh using 3DFAS
2. Run elastic simulation
3. Run elastic-plastic simulation for a multi-cycle loading mission
4. Determine the $\boldsymbol{d\rho/dt}$ from the last loading cycle
5. Use the crack growth law $\boldsymbol{da/dt = \alpha|d\rho/dt|}$) to evaluate the crack growth rate
6. Advance the crack and mesh the model using 3DFAS

Steps 2 to 6 are repeated to simulate the growth of the crack. An example of the crack front advancement is shown in Figure 124 and Figure 125. No user intervention is needed while crack propagation simulation is performed for a given number of increments.

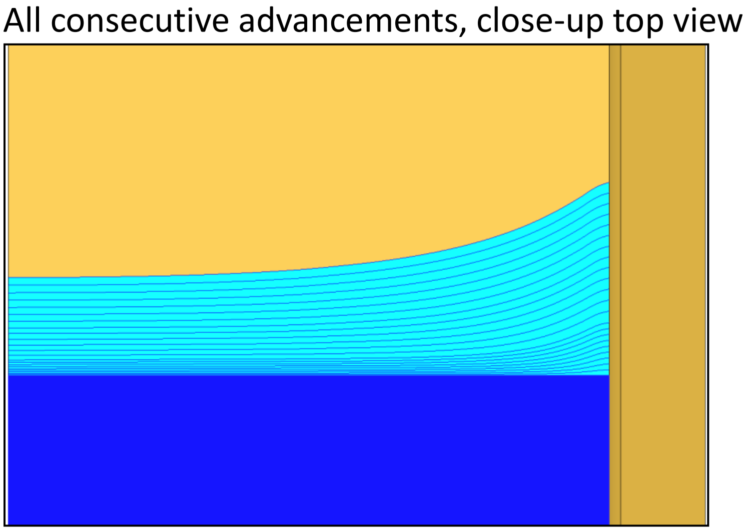

Figure 124: **Consecutive crack front advancements simulated in the study. Top view.**

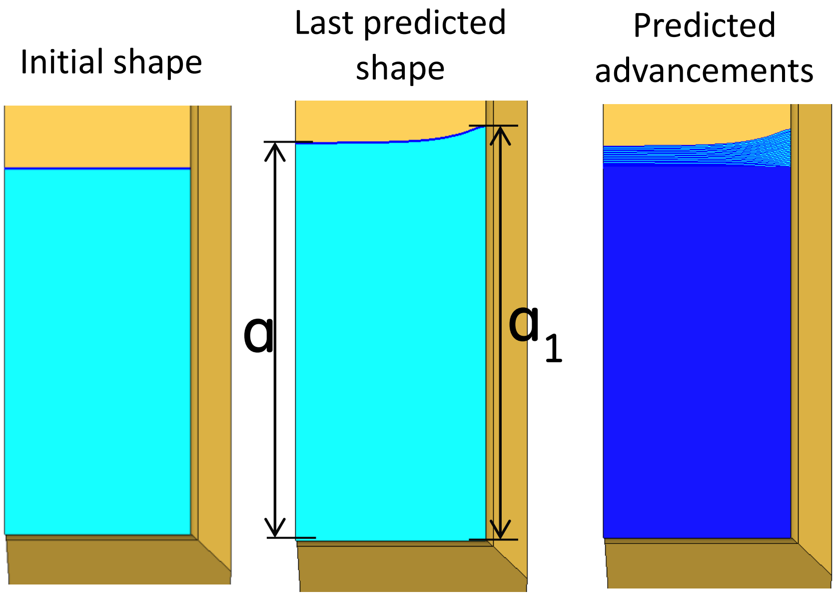

Figure 125: Crack front initial shape (straight), crack front advancements and two crack size measurements that are extracted from the simulation (a, a1).

Two stress ratios, R=0.05, 0.5, were considered. Simulations were limited to a max load of 0.5 kips (1kip=1000 pound-force) due to ANSYS convergence issues (large deformations at the crack front). The targeted max load was 1.9 kips, the load that was carried in the experiment. For this reason, in order to verify the solution (crack size vs. cycles), we generated a fatigue crack growth (da/dN vs. ΔK) from the CCTP model and use LEFM framework to simulate the same crack growth process. The Paris parameters that we used in the simulation were: C=2.49211E-9, n=2.927. A comparison between "classical" Paris crack growth model and the CCTP is given in Figure 126 and Figure 127.

Another verification of the 3D model was done against 2D FE solutions. Displacement (u_y, the loading direction displacement) along the centerline in the 3D model was compared against displacement prediction from the 2D FE model. The comparison is shown in Figure 128. Difference between crack tip plasticity between the 2D and 3D FE models is expected. The 3D model can capture crack tip plasticity size transition from free surface to the centerline while the 2D model cannot since the geometry is planar. The comparison between the two displacement fields confirms that the switch from 2D models to 3D was performed appropriately.

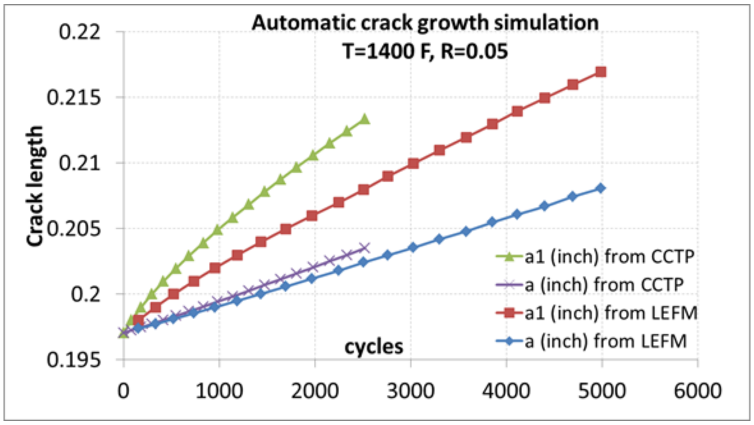

Figure 126: Crack size (a, a1) vs. cycles using LEFM framework and CCTP, R_σ=0.05. Simulations did not consider hold-time.

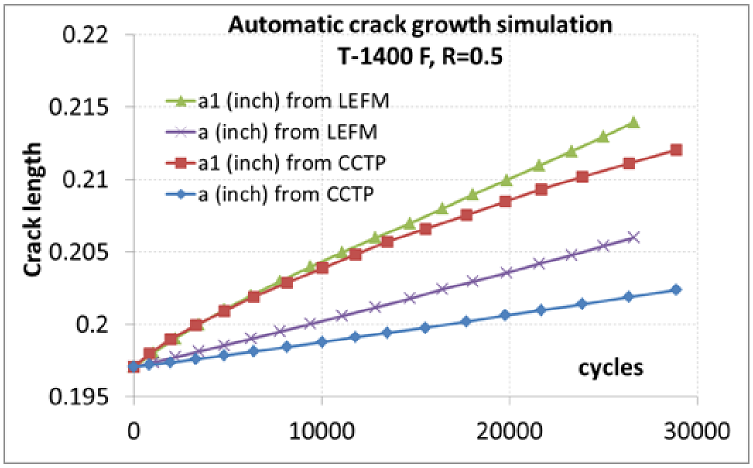

Figure 127: Crack size (a, a1) vs. cycles using LEFM framework and CCTP, R_σ=0.5. Simulations did not consider hold-time.

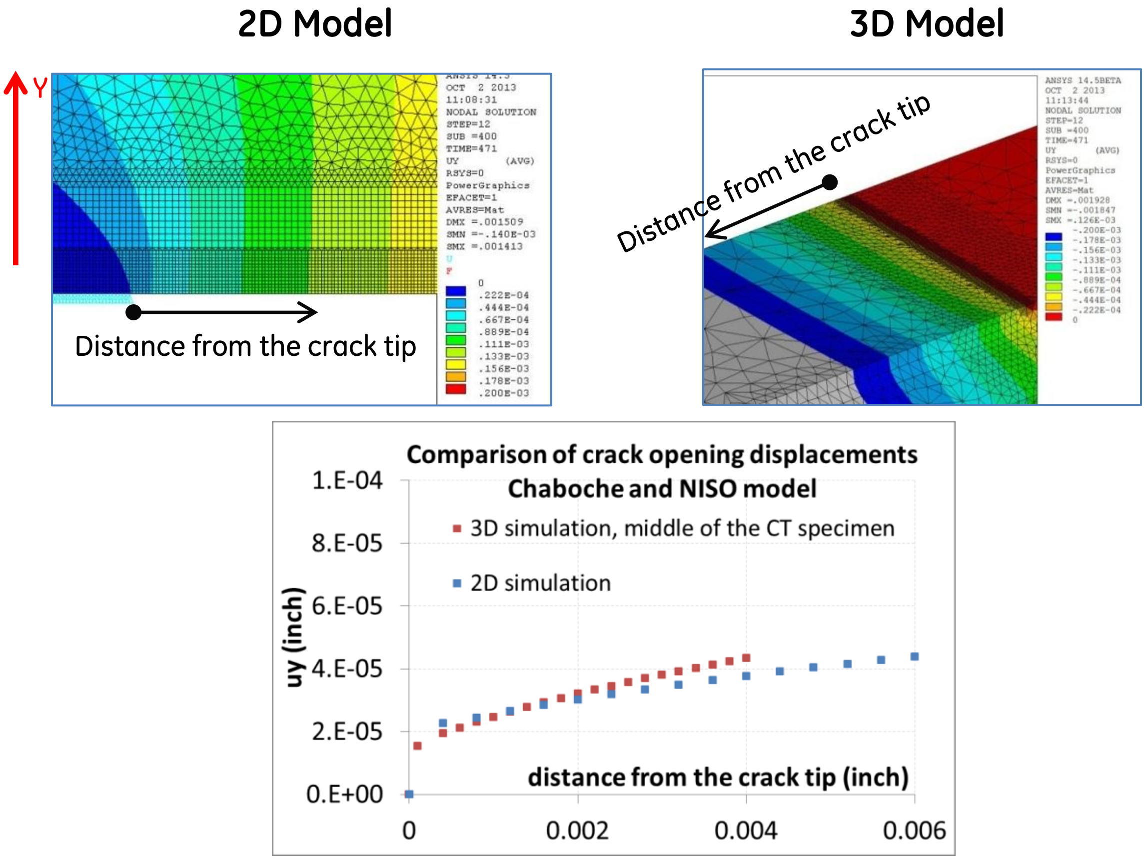

Figure 128: Displacement field (elastic plastic simulation) comparison between the 2D FE model and the 3D centerline path along the crack face.

6.6. Crack growth rate predictions using cyclic plasticity, creep and oxidation

Using the continuum-damage based creep model developed in Task 5 (see Section 5) in addition to the BKIN constitutive model developed in Task 6, a 2D compact tension FE model was used to capture evolution of crack tip plasticity for different loading missions. The analysis was performed in ANSYS. The FE model uses constitutive models calibrated at 1400˚F while the applied load was set to 0.5 kips. We made several attempts to use larger loads to predict fatigue crack growth rate for different ΔK values but, due to convergence issues in ANSYS, these solutions could not be obtained.

Three mission profiles were considered: [10, 1e3, 10], [10, 1e4, 10], [10, 1e5, 10] seconds for an R ratio of 0.05. A mission profile starts with a loading ramp (10 seconds) followed by a hold time (1e3, 1e4 or 1e5 seconds) and an unloading step of 10 seconds. For each mission profile a set of 25 loading steps were simulated to reach steady state conditions and capture dρ evolution for each step of the loading cycle. A typical dρ evolution is shown in Figure 129.

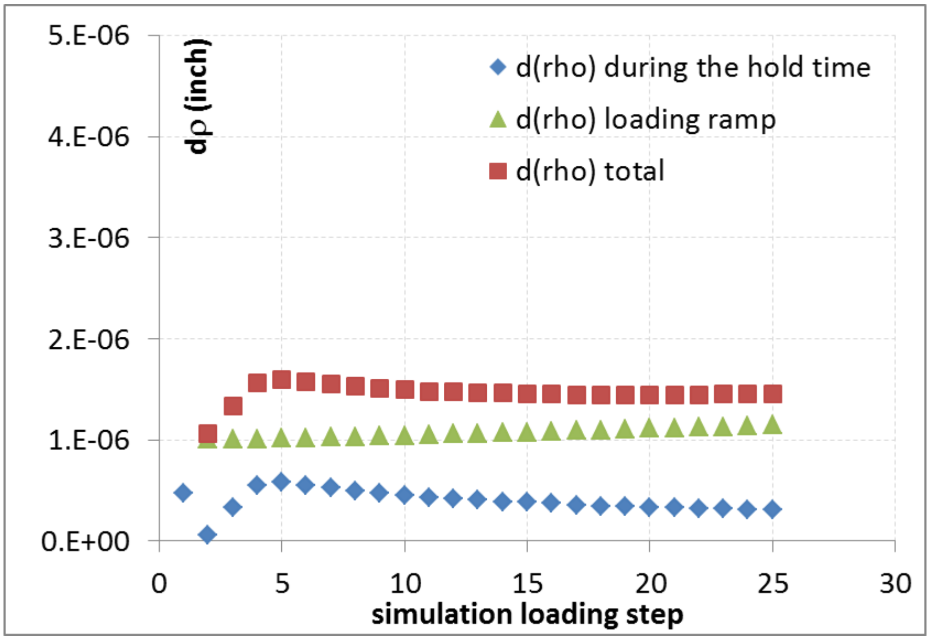

Figure 129: dρ evolution for 25 consecutive [10, 1e4, 10] sec cycles.

Crack growth rate was estimated using the process shown in Section 6.3 for dρ evolution during hold time as well as loading ramp and unloading step. The fatigue crack growth rate during the loading ramp was captured with Equation (6.3) while contribution due to creep was captured based on evolution of dρ during the hold time $\frac{\partial a}{\partial t}_{creep} = \left(\frac{d\rho}{dt}\right)_{hold\ time}$ in the last cycle of the simulation (25th).

The oxidation model described in Equation (6.10) was used to provide the additional term in the crack growth rate for a ΔK=10 ksi*in^0.5 as following:

For a HT=1,000 sec: da/dN = 9.295*10^-7
For a HT=10,000 sec: da/dN = 6.169*10^-6
For a HT=100,000 sec: da/dN = 9.513*10^-6

The three (3) fatigue crack growth rate predictions are shown in Figure 130. The ANSYS constitutive model input used for these 2D predictions is the following:

```
MPTEMP,,,,,,,,
MPTEMP,1,0
MPDATA,EX,1,,23.3e3
MPDATA,PRXY,1,,.3

TB,CREE,1,1,7,11
TBTEMP,1425
TBDATA,,5.4042E-075,24.948,4.2346,4.2075E-015,0,0
TBDATA,,0,,,,,
```

```
TB,BKIN,1,1,2,1
TBTEMP,1425
TBDATA,,90,50,,,,
```

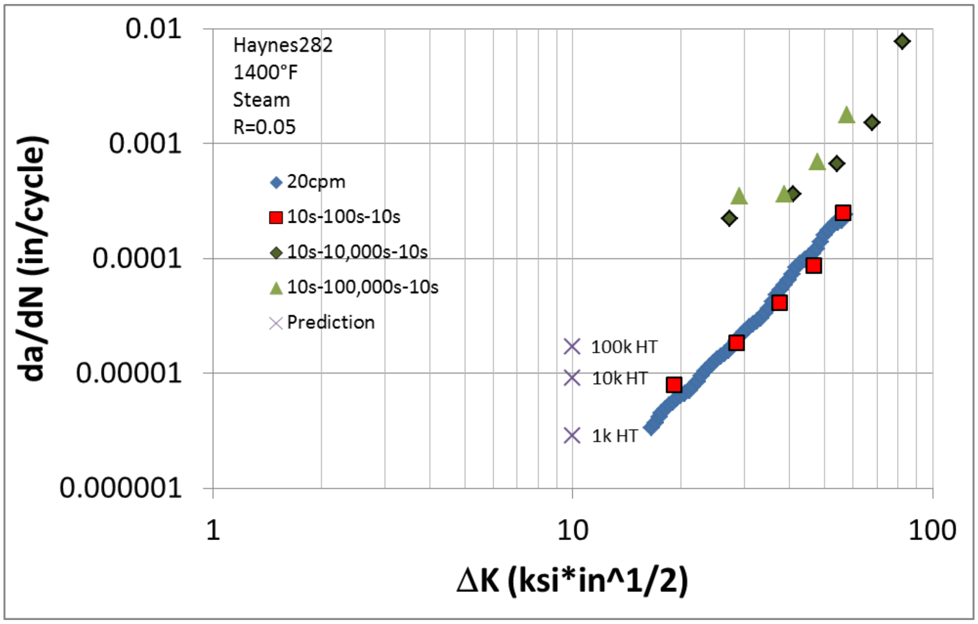

Figure 130: Model predictions for three different mission profiles: Hold time=1e3, 1e4, 1e5 seconds.

6.7. Summary

Task 6 focused on predicting crack growth rate at various testing conditions of Alloy 282. Under this task as well as Task 2, fatigue crack growth measurements were conducted using compact tension (CT) specimens at different load ratios R=0.05, 0.025, 0.5, fixed ΔK or ΔK sweep, and different environment (vacuum, air, steam). These data were used to calibrate the fatigue crack growth model at 1200˚F and 1400˚F, and to validate model predictions.

The fatigue crack growth model, proposed by Pommier et al, relates crack growth rate (da/dt) to crack tip blunting rate (dρ/dt). It was extended by Ruiz-Sabariego et al to include oxidation effects under hold time conditions. To capture crack tip plasticity in the FE models, round bar specimens were used to obtain stress strain bulk response, which was further used to calibrate different constitutive models (Chaboche, bilinear kinematic). Using 2D FEM, the constitutive fatigue crack growth model was calibrated at R=0.05. Fatigue crack growth rate predictions were then made for R=0.25 and 0.5. The predictions were found within 2X expected measurement scatter.

Since a 2D FEM fatigue crack growth framework has limitations in life assessment for engineering structures, a transition to 3D model representation was made using a GE proprietary tool that can simulate crack growth using ANSYS as solver, and the rest of the simulation (loading mission, constitutive models) was recycled. Two 3D automatic crack growth simulations at R=0.05 and 0.5 were performed using 3DFAS (GE proprietary tool) and the established crack growth model for each node along the crack front and each of the simulated crack advancement.

To further address the observed higher crack growth rate in loading cycles with hold times, creep model developed in Task 5 was added to the constitutive model in the 2D CT FE models and, an oxidation model was incorporated based on the available measurement data. Crack growth rate predictions were made for three loading profiles with 1e3, 1e4, 1e5 seconds hold time.

Acknowledgements

Timothy Hanlon, Kejie Zhao, Ju Li, Chen Shen, Ning Zhou, Monica Soare, Shakhrukh Ismonov, Adrian Loghin performed the technical tasks and prepared this report.

We wish to thank Vito Cedro, Samuel Thamboo, Liang Jiang, Robin Schwant, and Deepak Saha for technical discussions and program advisory;

Dustin Ellis, Ernie Hall, Ian Spinelli for microstructure characterization;

Michael Gilhooly for mechanical testing;

Ramkumar Oruganti, Mallikarjun Karadge for discussions on creep modeling;

Yongmei Jin and Yu Wang for discussions on phase field crack model;

Patrick Norais for contract administration;

REFERENCES

1 Bricknell, R. H. & Woodford, D. A. Grain-Boundary Embrittlement of the Iron-Base Superalloy-In903a. *Metallurgical Transactions a-Physical Metallurgy and Materials Science* **12**, 1673-1680, doi:10.1007/bf02643573 (1981).

2 Ma, L. Z. & Chang, K. M. Identification of SAGBO-induced damage zone ahead of crack tip to characterize sustained loading crack growth in alloy 783. *Scripta Materialia* **48**, 1271-1276, doi:10.1016/s1359-6462(03)00049-6 (2003).

3 McMahon, C. J. Comments on "Identification of SAGBO-induced damage zone ahead of crack tip to characterize sustained loading crack growth in alloy 783". *Scripta Materialia* **54**, 305-307, doi:10.1016/j.scriptamat.2005.09.030 (2006).

4 Bika, D. & McMahon, C. J. A Model for Dynamic Embrittlement. *Acta Metallurgica Et Materialia* **43**, 1909-1916, doi:10.1016/0956-7151(94)00387-w (1995).

5 https://materialsproject.org.

6 *Haynes 282 Brochure*, <http://www.haynesintl.com/pdf/h3173.pdf> (

7 *TTNI7*, <http://www.thermotech.co.uk/databases.html#Ni-DATA> (

8 Gabb, T. P. *et al.* in *Superalloys 2000.* (eds T M Pollock *et al.*) 405-414 (TMS).

9 Kampmann, R. & Wagner, R. in *Decomposition of alloys: the early stages* (eds Peter Haasen, V Gerold, Richard Wagner, & M F Ashby) 91-103 (Pergamon Press, 1984).

10 Langer, J. S. & Schwartz, A. J. Kinetics of nucleation in near-critical fluids. *Physical Review A* **21**, 948-958 (1980).

11 Wendt, h. & Haasen, P. Nucleation and growth of γ' -Precipitates in Ni-14 at.% Al. *Acta Metallurgica* **31**, 1649-1659, doi:10.1016/0001-6160(83)90163-3 (1983).

12 Simmons, J. P., Shen, C. & Wang, Y. Phase field modeling of simultaneous nucleation and growth by explicitly incorporating nucleation events. *Scripta Materialia* **43**, 935-942, doi:10.1016/s1359-6462(00)00517-0 (2000).

13 Kim, S. G., Kim, W. T. & Suzuki, T. Phase-field model for binary alloys. *Physical Review E* **60**, 7186-7197 (1999).

14 *MOBNI1*, <http://www.thermocalc.com/res/pdfDBD/DBD_MOBNi1-2.pdf> (

15 Brown, L. M. & Ham, R. K. *Strengthening methods in crystals*. 68 (Elsevier, 1971).

16 Dyson, B. F. Microstructure based creep constitutive model for precipitation strengthened alloys: theory and application. *Mat Sci. Tech* **25**, 213-220 (2009).

17 Delaunay, B. Sur la sphère vide. *Izvestia Akademii Nauk SSSR, Otdelenie Matematicheskikh i Estestvennykh Nauk* **7**, 793-800 (1934).

18 de Berg, M., Cheong, O., van Kreveld, M. & Overmars, M. *Computational Geometry: Algorithms and Applications*. (Springer-Verlag, 2008).

19 *ThermoCalc*, <http://www.thermocalc.com/products-services/software/thermo-calc> (

20 Wright, I. G. & Dooley, R. B. A review of the oxidation behaviour of structural alloys in steam. *International Materials Reviews* **55**, 129-167, doi:10.1179/095066010x12646898728165 (2010).

21 Jin, Y. M., Wang, Y. U. & Khachaturyan, A. G. Three-dimensional phase field microelasticity theory and modeling of multiple cracks and voids. *Applied Physics Letters* **79**, 3071-3073 (2001).

22 Wang, Y. U., Jin, Y. M. M. & Khachaturyan, A. G. Phase field microelasticity theory and simulation of multiple voids and cracks in single crystals and polycrystals under applied stress. *Journal of Applied Physics* **91**, 6435-6451 (2002).

23 Barenblatt, G. in *Advances in Applied Mechanics Volume 7* Vol. 7 Ch. Advances in Applied Mechanics, 55-129 (Elsevier, 1962).

24 Rice, J. R. A Path Independent Integral and the Approximate Analysis of Strain Concentration by Notches and Cracks. *Journal of Applied Mechanics* **35**, 379-386, doi:10.1115/1.3601206 (1968).

25 Bilby, B. A. & Eshelby, J. D. in *Advances in Applied Mechanics Volume 7* Vol. 7 Ch. Advances in Applied Mechanics, 99-182 (Elsevier, 1962).

26 Wang, Y. U. *Private communication* (2013).

27 Suresh, S. *Fatigue of Materials*. (Cambridge University Press, 1998).

28 Guo, X. H., Shi, S.-Q. & Ma, X. Q. Elastoplastic phase field model for microstructure evolution. *Applied Physics Letters* **87**, 221910 (2005).

29 Cahn, J. W. & Hilliard, J. E. Free Energy of a Nonuniform System. I. Interfacial Free Energy. *Journal of Chemical Physics* **28**, 258-267 (1958).

30 Dyson, B. F. Creep and Fracture of metals: mechanisms and mechanics. *Revue de Physique Appliquée* **23**, 605-613 (1988).

31 McLean, M. & Dyson, B. F. Modeling the Effects of Damage and Microstructural Evolution on the Creep Behavior of Engineering Alloys. *Journal of Engineering Materials and Technology* **122**, 273-278, doi:10.1115/1.482798 (2000).

32 Reed, R. C. *The Superalloys, Fundamentals and Applications*. (Cambridge University Press, 2006).

33 Needleman, A. & Rice, J. R. Plastic creep flow effects in the diffusive cavitation of grain boundaries. *Acta Metallurgica* **28**, 1315-1332, doi:http://dx.doi.org/10.1016/0001-6160(80)90001-2 (1980).

34 Kassner, M. E. & Pérez-Prado, M. T. *Fundamentals of Creep in Metals and Alloys*. (Elsevier Science Ltd, 2004).

35 Cocks, A. C. F. & Ashby, M. F. Intergranular fracture during power-law creep under multiaxial stresses. *Metal Science* **14**, 395-402, doi:10.1179/030634580790441187 (1980).

36 Cocks, A. C. F. & Ashby, M. F. On creep fracture by void growth. *Progress in Materials Science* **27**, 189-244, doi:http://dx.doi.org/10.1016/0079-6425(82)90001-9 (1982).

37 Divinski, S. V., Reglitz, G. & Wilde, G. Grain boundary self-diffusion in polycrystalline nickel of different purity levels. *Acta Materialia* **58**, 386-395, doi:http://dx.doi.org/10.1016/j.actamat.2009.09.015 (2010).

38 Hayhurst, D. R., Lin, J. & Hayhurst, R. J. Failure in notched tension bars due to high-temperature creep: Interaction between nucleation controlled cavity growth and continuum cavity growth. *International Journal of Solids and Structures* **45**, 2233-2250, doi:http://dx.doi.org/10.1016/j.ijsolstr.2007.11.026 (2008).

39 Perrin, I. J. & Hayhurst, D. R. A method for the transformation of creep constitutive equations. *International Journal of Pressure Vessels and Piping* **68**, 299-309, doi:http://dx.doi.org/10.1016/0308-0161(95)00069-0 (1996).
40 Holmström, S. & Auerkari, P. Robust prediction of full creep curves from minimal data and time to rupture mode. *Energy Materials, Materials Science & Engineering for Energy Systems* **1**, 249-255 (2006).
41 Holdsworth, S. R. *Recommendations And Guidance For The Assessment Of Creep Strain Data; Eccc Recommendations - Volume 5 Part Ib*, <http://www.ommi.co.uk/etd/eccc/advancedcreep/V5PIbi2x.pdf> (2003).
42 Santella, M., Shingledecker, J. & Swinderman, B. in *24th Annual Conference on Fossil Energy Materials* (Pittsburg, PA, 2010).
43 Hamam, R. *Simulation de la propagation des fissures par fatigue dans les toiles des roués de train sous chargement à amplitude variable* THÈSE DE DOCTORAT thesis, ENS Cachan, (2006).
44 Hamam, R., Pommier, S. & Bumbieler, F. Variable amplitude fatigue crack growth, experimental results and modeling. *International Journal of Fatigue* **29**, 1634-1646, doi:http://dx.doi.org/10.1016/j.ijfatigue.2007.02.005 (2007).
45 Pommier, S. & Hamam, R. Incremental model for fatigue crack growth based on a displacement partitioning hypothesis of mode I elastic–plastic displacement fields. *Fatigue & Fracture of Engineering Materials & Structures* **30**, 582-598, doi:10.1111/j.1460-2695.2007.01128.x (2007).
46 Ruiz-Sabariego, J. A. & Pommier, S. Oxidation assisted fatigue crack growth under complex non-isothermal loading conditions in a nickel base superalloy. *International Journal of Fatigue* **31**, 1724-1732, doi:10.1016/j.ijfatigue.2009.03.009 (2009).
47 *ANSYS Release 14.5 Documentation*. 4 (ANSYS Inc.).